

The Pennsylvania State University
The Graduate School
College of Engineering

**ATMOSPHERICALLY AWARE AIRCRAFT GUIDANCE USING *IN*
SITU OBSERVATIONS**

A Dissertation in
Aerospace Engineering
by
John Bird

© 2019 John Bird

Submitted in Partial Fulfillment
of the Requirements
for the Degree of

Doctor of Philosophy

August 2019

The dissertation of John Bird was reviewed and approved* by the following:

Jacob W. Langelaan
Associate Professor of Aerospace Engineering
Dissertation Advisor, Chair of Committee

Sean Brennan
Professor of Mechanical Engineering

Mark Maughmer
Professor of Aerospace Engineering

George Young
Professor of Meteorology

Amy Pritchett
Professor of Aerospace Engineering
Head of Department of Aerospace Engineering

*Signatures are on file in the Graduate School.

Abstract

A major challenge to widespread use of small electric UAS is their limited energy budgets and sensitivity to environmental conditions. Differences between forecast and realized weather conditions are often large enough that the energy required to complete a mission can differ significantly from that expected by *a priori* flight plans. This makes autonomous awareness of and response to the environmental state necessary in order to enable small UAS to conduct long-range missions. To develop this capability, the uncertain atmospheric state is decomposed into stochastic and systematic uncertainty which can be managed separately by the aircraft using speed and power output commands respectively.

Speed variations enable an aircraft to preferentially spend longer in favorable areas, making the atmosphere appear more conducive to UAS flight. A speed command is developed which responds optimally to stochastic conditions while meeting a specified arrival time at a destination.

A modeling system is developed which allows the aircraft to build a model of the vertical structure of the atmosphere using *in situ* observations and to transform the atmospheric state into a mission performance cost. This model is then employed in a multi-armed bandit inspired trajectory planner which balances reducing the aircraft's mission performance cost with maintaining a model of the environment. The planner solves the exploration-exploitation problem without employing heuristics to value information and demonstrates good performance and robustness when compared to a collocation-based optimal planner.

Together these techniques compose a system which allows small UAS to reduce their energy expenditure and the effect of the uncertain atmospheric state on their performance. Components of this system are tested in simulation and flight experiments and demonstrate an improvement in the ability of small UAS to operate in unknown and uncertain environments

Table of Contents

List of Figures	viii
List of Tables	xiv
Acknowledgments	xv
Chapter 1	
Introduction	1
1.1 Motivation	2
1.1.1 Solar Augmented Aircraft	3
1.1.2 Challenges to Small UAS Flight at Low Altitudes	4
1.1.3 Autonomy in Uncertain Environments	5
1.2 Design Goals	6
1.3 Primary Research Contributions and Reader’s Guide	9
Chapter 2	
Review of Relevant Literature	11
2.1 Trajectory Planning	11
2.1.1 Robotic Motion Planning	11
2.1.2 Long Range Aircraft Path Planning	12
2.1.3 Solar Aircraft Flight Planning	16
2.1.4 Soaring as a Stochastic Planning Problem	17
2.2 Environmental Modeling	19
2.3 Exploration vs Exploitation	21
2.3.1 Sensor Placement	21
2.3.2 Multi-Armed Bandits	22
2.4 Summary	24
Chapter 3	
Environment, Models, and Platforms	26
3.1 Relevant Characteristics of the Lower Atmosphere	26

3.1.1	Clouds	27
3.1.2	Winds	29
3.1.3	Vertical Motion	30
3.1.4	Weather Hazards	31
3.2	Aircraft Motion and Energetic Models	32
3.2.1	Aircraft Energetics	32
3.2.2	Kinematic Models	34
3.2.3	Solar Power System	35
3.2.4	Stored Energy	37
3.3	Environmental Models	37
3.3.1	Clouds	37
3.3.2	Wind	39
3.3.3	Updrafts	39
3.3.4	Numerical Weather Prediction	40
3.4	Aircraft	40
3.4.1	SB-XC	40
3.4.2	Vulture	41

Chapter 4

	Hybrid Solar Aircraft	43
4.1	Solar Aircraft Performance	44
4.1.1	Maximum Speed in Pure Solar Flight	44
4.1.2	Maximum Wing Loading in Pure Solar Flight	45
4.2	Solar Augmented Performance	46
4.2.1	Performance Sensitivity to Atmospheric Conditions	48
4.3	Summary	50

Chapter 5

	Speed to Fly	51
5.1	Speed to Fly with Stochastic Energy Input	51
5.1.1	Pure Solar Flight with Interruptions	52
5.1.2	Joint Optimization of Solar and Updraft Energy	55
5.1.3	Speed to Fly for Schedule Keeping	59
5.1.3.1	Energy Optimization With Speed Constraint	60
5.1.3.2	Speed to Fly Inversion	61
5.1.3.3	Convergence Analysis	62
5.2	Simulations	66
5.2.1	Approximating the MacCready Number	66
5.2.2	Monte Carlo Simulations	67
5.3	Flight Tests	70

5.3.1	Mission Description	71
5.3.2	Results	72
5.4	Summary	75

Chapter 6

	Modeling the Environment	77
6.1	Modeling with Basis Splines	79
6.1.1	Time Update	81
6.1.2	Process Noise	82
6.1.3	Observation Models	84
6.1.4	Measurement Noise	85
6.1.5	Sample Noise	87
6.1.5.1	Wind Sampling Error	87
6.1.5.2	Solar Sampling Error	88
6.1.5.3	Updraft Sampling Error	89
6.2	Computing Travel Cost	89
6.3	Flight Test	92
6.3.1	Test Description	92
6.3.2	Process and Measurement Noise	94
6.3.3	Results	95
6.3.3.1	Comparison with Radiosonde Observations	96
6.3.3.2	Comparison with Numerical Weather Model	99
6.3.4	Travel Cost	102
6.4	Summary	103

Chapter 7

	Altitude Optimization	106
7.1	Travel Cost	108
7.2	Mission Constraints	111
7.3	Selecting an Altitude to Explore	112
7.3.1	Expected Cost of Exploration	112
7.3.2	Finding the Lowest Cost Altitude	115
7.4	Monte Carlo Simulations	117
7.4.1	Simulation Tests	117
7.4.2	Mean Performance	120
7.4.3	Energy Budget for Likely Mission Completion	122
7.4.4	Comparison of Trajectories	123
7.4.5	Effect of Information Age	125
7.4.6	Robustness to Local Minima	128
7.4.7	Value of <i>a priori</i> Information	128

7.5	Summary	131
Chapter 8		
	Conclusion	134
8.1	Summary of Contributions	135
8.1.1	Separation of Scales of Response to Atmospheric Uncertainty	135
8.1.2	Speed Control to Manage Stochasticity	135
8.1.3	Environmental and Travel Cost Modeling	135
8.1.4	<i>in situ</i> Flight Planning	136
8.2	Recommendations for Future Research	137
8.2.1	Managing Stochasticity in Other Domains	137
8.2.2	Identification of and Response to Weather Hazards	137
8.2.3	Multi-Armed Bandit Planning	137
8.2.4	Exploration Cost	138
8.2.5	Forward Looking Sensors	138
	Works Cited	139

List of Figures

1.1	Odysseus high altitude pseudosatellite aircraft.	2
1.2	Mid-air disintegration of Helios.	3
1.3	Wind and cloud fields in the lower troposphere are much more complicated and difficult to predict than the atmospheric state at higher altitudes.	5
1.4	Definition of the <i>in situ</i> planning problem.	7
2.1	Approaches to robotic path planning.	12
2.2	Long-range trajectory planned for AtlantikSolar.	13
2.3	Stochastic collocation can quantify trajectory perturbations introduced by environmental uncertainty.	15
2.4	Evolution of the optimal station keeping flight path for a solar aircraft.	17
2.5	Speed to fly computed for a known spatially varying wind field.	18
2.6	Systematic errors in a wind forecast observed by a small UAS.	20
3.1	UAS operating altitudes.	27
3.2	Cloud types and distribution.	28
3.3	The nocturnal low-level jet.	30

3.4	An environment where a small forecast error can cause a significant planning error.	31
3.5	Aircraft kinematics used in simulations.	35
3.6	Exponential decay model for solar intensity within clouds.	38
3.7	The SB-XC, a small UAS commonly used for soaring research. . . .	41
	a RnR products SB-XC sailplane modified with an electric motor. .	
	b Speed polar for the SB-XC.	
3.8	The Vulture UAS.	42
4.1	Silent Falcon, a solar augmented small UAS.	43
4.2	Battery energy required for a 12 hour mission on the equinox. . . .	47
4.3	Payload capacity and battery mass required for SB-XC to fly a 12 hour mission.	48
	a Payload capacity and battery mass required to fly at best cruise speed, 14.5 m s^{-1}	
	b Payload capacity and battery mass required to fly 17 m s^{-1}	
4.4	Effect of solar augmentation on the speed polar.	49
5.1	Illustration of the speed to fly problem.	52
5.2	Solar powered cross-country performance for a small UAS.	54
	a Speed schedules for several values of net energy.	
	b Best average speed achieved.	

5.3	Average speed as a function of cloud factor for several solar insolation values with not net energy.	55
5.4	Problem definition for simultaneous optimization of updraft and solar energy.	56
5.5	Performance of the approximate unified speed to fly computation with arrival time constraint.	67
	a Optimal speed as a function of harvested energy.	
	b Residual error in the speed command.	
5.6	Ensemble mean energy savings achieved using speed to fly.	69
	a Energy savings for flying the speed to fly schedule.	
	b Energy savings expressed as a fraction of the energy required for constant speed flight.	
5.7	Trajectory of relative total energy in one simulated flight.	70
5.8	Distribution of error in the mean speed.	71
5.9	Desired flight path for the speed to fly test.	72
5.10	Actual flight path during one speed to fly test.	73
5.11	Command and state histories during the speed to fly test.	74
6.1	Definition of the environmental modeling problem.	77
6.2	Spline bases and an approximate function.	80
6.3	Computation of forecast error using a later model analysis.	83
6.4	Mean absolute error profiles for the HRRR wind forecast at a point in central Pennsylvania.	83

a	East wind error (positive is air parcels moving east)	
b	North wind error (positive is air parcels moving north)	
6.5	Mesoscale environment for the atmospheric modeling test.	93
6.6	Aerial view of the test area showing the balloon trajectories and aircraft orbit location.	93
6.7	Time history of aircraft and balloon altitude.	94
6.8	Time-altitude depiction of the profile of aircraft estimated horizontal wind depicting its evolution throughout the day.	95
6.9	Aircraft and radiosonde profiles from 08:00 local time.	97
6.10	Aircraft and radiosonde profiles from 09:00 local time.	98
6.11	Aircraft and radiosonde profiles from 13:00 local time.	98
6.12	Aircraft and radiosonde profiles from 16:00 local time.	99
6.13	Aircraft measured and HRRR predicted wind profiles at 08:00 local time.	100
6.14	Aircraft measured and HRRR predicted wind profiles at 09:00 local time.	101
6.15	Aircraft measured and HRRR predicted wind profiles at 13:00 local time.	102
6.16	Aircraft measured and HRRR predicted wind profiles at 16:00 local time.	103
6.17	Travel cost - flight direction polar plot for a groundspeed of 15 m s ⁻¹	104
a	Cost for the vulture to travel at an altitude of 500 meters above sea level.	

b	Cost for the vulture to travel at an altitude of 650 meters above sea level.	
7.1	The altitude optimization problem in an uncertain environment. . .	107
7.2	Spectrum of atmospheric energy.	110
7.3	Limitations on the maximum travel cost skew the exploration cost distribution.	114
7.4	The exploration cost profile can be non-convex even if the underlying travel cost profile is.	115
7.5	Simulation epochs	118
7.6	Simulated flight path	118
7.7	Mean regret averaged over 652 simulation runs.	121
7.8	Empirical cumulative distribution of the energy required to complete the mission.	122
a	Energy required to complete the mission if the environmental state is known perfectly.	
b	Energy required to complete the mission when the planners are provided with a four hour forecast.	
7.9	Altitude and expended stored energy for perfectly informed planners.	124
a	Aircraft flight paths.	
b	Expended stored energy trajectory.	
7.10	State trajectories in a quiescent atmosphere.	126
a	Aircraft flight paths.	
b	Expended stored energy trajectory.	

7.11	State trajectories in a changing atmosphere.	127
	a Aircraft flight paths.	
	b Expended stored energy trajectories.	
7.12	Robustness of the <i>in situ</i> planner to local minima.	129
	a Aircraft flight paths.	
	b Expended stored energy trajectories.	
7.13	Empirical cumulative distribution of final energy state for the <i>in situ</i> and <i>a priori</i> planners with a four hour forecast and for the <i>in situ</i> planner with no prior information.	130

List of Tables

3.1	Solar power system and powertrain efficiencies.	36
3.2	Basic parameters of the SB-XC aircraft.	41
3.3	Basic parameters of the Vulture aircraft	41
5.1	Parameters of the thermal model used in the simulations.	68
5.2	Parameters of the cloud model used in the simulations.	68
5.3	Time of arrival performance for the flight test.	73
7.1	Mean final regret averaged over 652 simulations.	121

Acknowledgments

Portions of this research were funded by the Naval Research Laboratory under grant number N00173-17-1-G004.

I have consistently found the most valuable resource in my graduate studies to be the people around me. Without friends, family, colleagues, and mentors this journey would have been much harder and much less personally and intellectually fulfilling.

I have my advisor to thank for the opportunity to pursue a program of study inspired by and centered on soaring techniques. Jack's support, advice, and leadership has enabled me to grow from a new master's student into an independent scholar. He has consistently encouraged my intellectual curiosity and interests even outside of my primary research area. This has enriched my studies and given me a broad perspective on aerospace and robotics.

To my committee I am grateful for the instruction and advice throughout this process. The diversity and depth of expertise they have shared has enabled me to work at the intersection of disciplines while keeping my work grounded in history and practicality.

My collaborators within the university and at the Naval Research Lab have helped frame problems, conduct experiments, and been a great team to work with.

I am very grateful to the other members of the AVIA lab, who have been wonderful colleagues and great friends. They have challenged my assumptions, checked my math, and clarified my ideas. I am proud to have had the opportunity to work with such a capable group of people and look forward to seeing the future they help build.

My work in the lab would not be possible without the people outside of it. The instruction and encouragement my parents have provided from an early age gave me the foundation for this work. Their example gave me the courage to take risks in pursuit of a goal and the perseverance to achieve it. My friends in State College have made this my home, they are outstanding people and I am fortunate to know them. I am especially grateful to Becky who has been a companion in adventure, partner in mischief, and source of constant love and support.

Dedication

for all of the birds who have taught me to fly

Chapter 1 |

Introduction

The objective of this thesis is to describe the development of a system that enables an autonomous aircraft to understand and respond to variations in the environment which influence the aircraft's energy state. The work described here is especially concerned with developing a system that can travel long distances and mixes the use of energy stored onboard the aircraft with energy gathered from the environment. Many of the developments are, however, equally applicable to aircraft which only employ stored energy. This research was inspired by the needs of small fixed-wing uninhabited aerial systems (UAS) equipped with solar panels and operating over long ranges at relatively low altitude in remote environments.

This guiding problem highlights several interesting general problems in autonomy, robotics, and UAS guidance. The aircraft operates in an environment characterized by both stochasticity and uncertainty. That is, the environment has features whose locations and characteristics cannot be predicted and in addition the mean environmental state is not exactly known *a priori*. Since the aircraft energy state is influenced by the environment, this uncertainty poses a challenge in choosing control policies that efficiently use energy, especially since a significant fraction of the energy budget is harvested from the environment through solar panels or flight in updrafts.

This thesis examines the design and operating space for small UAS equipped with solar panels but which do not rely only on solar power. It defines how to separate response to the mean state and stochastic elements of the environment and develops a method to manage stochasticity while navigating to a point. A framework for modeling the mean state of the environment, updating it with *in situ* observations, and fusing it with *a priori* predictions is then developed. Finally, a means is developed to manage uncertainty in the environmental model while trying



Figure 1.1: Large UAS such as the Aurora Flight Sciences Odyssey can offer very long range and endurance, but require large crews and significant infrastructure to maintain and operate. Photo reproduced from Aurora Flight Sciences (2019) “Odysseus – High Altitude, Ultra-long Endurance, Pseudo-Satellite – HAPS – Aurora Flight Sciences” [1].

to minimize energy consumption.

1.1 Motivation

Small electric UAS have many compelling features – they have few moving parts, simple logistics, and can be operated with little infrastructure. Unfortunately their capability is constrained by battery technology; missions longer than a few hours or about 100 kilometers are not yet practical to perform with electric aircraft. This is not a particularly severe restriction in the current regulatory environment which requires the aircraft be in sight of a human operator at all times. As regulations evolve and permit UAS flight beyond line of sight and without human operators, new applications will be available which would benefit from greater range and endurance.

Large fixed-wing and rotorcraft UAS can offer hours of endurance and hundreds of kilometers of range but bring the same logistics, maintenance, and capital costs as existing piloted aircraft. In some applications, such as cargo and passenger transport, a large aircraft is required regardless of whether the aircraft is piloted or autonomous. Other missions such as mapping and air sampling can in principle be performed with much smaller, less expensive platforms, but small UAS with adequate performance and reliability do not yet exist. Increasing the range, endurance, and autonomy of small electric UAS will help make aerial systems more accessible and enable their use in more applications.



Figure 1.2: Mid-air disintegration of the Helios solar aircraft. The need for atmospheric pseudosatellite aircraft to be extremely lightweight makes them very fragile and susceptible to damage from turbulence at low altitudes. Reproduced from Noll et al. (2004) “Investigation of the Helios Prototype Aircraft Mishap; Volume I: Mishap Report” [4].

1.1.1 Solar Augmented Aircraft

Advances in solar panels, electric motors, and power electronics have made it possible to build fixed-wing UAS powered by solar energy, dramatically increasing range and endurance. Even with these improvements, solar cells have low power density so aircraft powered purely by solar energy must be very lightweight. Typically solar aircraft are envisioned as “atmospheric pseudosatellites” which offer extremely long endurance at high altitude, making them attractive as communications relays and surveillance aircraft [2]. The low power density of solar cells and the thin air at high altitudes requires very large, very lightweight airframes that are fragile and expensive. Pseudosatellites must remain aloft for weeks to justify the risk they face in takeoff, landing, and flight through the lower atmosphere. Several of these aircraft have been damaged or destroyed while flying at low altitudes during launch or recovery [3–6], including the spectacular mid-air disintegration of Helios (Figure 1.2).

The unique capabilities of pseudosatellites are compelling, but these aircraft are too expensive and too specialized for widespread use. If the requirement for persistent solar flight is relaxed, the battery mass required to sustain the aircraft overnight can be devoted to structure or payload. This opens the design space to smaller, more conventional aircraft that cannot fly indefinitely on solar power

alone, but can still achieve hours of endurance and hundreds of kilometers of range. Several of these “solar augmented” aircraft have been constructed such as the Solar Puma [7] and SoLong [8]. Even nominally persistent solar aircraft such as AtlantikSolar [9] may operate as “solar augmented” aircraft when carrying a large payload or in suboptimal solar conditions.

“Solar augmented” aircraft offer more range and endurance than previous small UAS in a simpler, more robust platform than pseudosatellites. These aircraft are capable of accomplishing many missions such as aerial mapping, air sampling, news reporting, and tactical surveillance that require significant, but not indefinite range and endurance.

1.1.2 Challenges to Small UAS Flight at Low Altitudes

To achieve smaller, simpler, more robust airframes, small solar augmented aircraft must give up the very high altitude capability of pseudosatellites. This can compromise some of the surveillance and communications relay missions that pseudosatellites perform, but solar augmented aircraft can accomplish other tasks that are impractical to perform from high altitude. For example, air quality monitoring or other missions requiring *in situ* observations at low altitude clearly cannot be performed from the stratosphere. Flying at low altitude can be beneficial even in sensing applications as the same imaging resolution can be achieved with less sophisticated sensors.

Flying at low altitudes does make flight planning and management considerably more complicated however. The lower troposphere is a complex environment and a challenging place to operate aircraft, especially solar powered ones. There are many phenomena which can affect the energy budget of a small UAS. Horizontal winds and vertical air motion can both be of similar magnitude to the aircraft’s maximum performance, and clouds can interrupt solar energy [10]. Existing UAS are generally operated close to a ground station so that the pilot can monitor conditions and direct the aircraft’s response, but future UAS will need greater awareness of their environment to fly reliably in this complex environment.

Numerical weather prediction systems are constantly improving and will help to enable autonomous flight, but UAS cannot rely solely on forecasts. Clouds and vertical motion in the lower atmosphere form stochastically and can have a

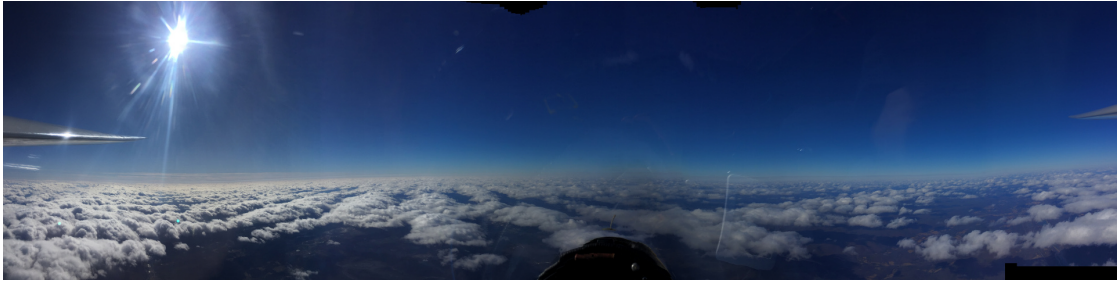


Figure 1.3: Wind and cloud fields in the lower troposphere are much more complicated and difficult to predict than the atmospheric state at higher altitudes. Photo taken by the author from a sailplane at 13,500 feet over central Pennsylvania. The complex cloud field at low altitude is formed by the interaction of orographic wave and wind-aligned convection.

significant impact on an aircraft’s energy budget [10]. Further, interaction between the stochastic features and mean atmospheric state combined with uncertainty in boundary conditions limits the possible skill of weather prediction systems [11].

A robust autonomous aerial system needs to be able to deal with this uncertainty and stochasticity in the environment. This is especially true for small, electric and solar powered aircraft; the energy available and required for these aircraft to complete a mission is more closely coupled to the environment. The capability of small UAS can be enhanced by responding to the environment in a way that reduces the mean energy consumption and makes the energy consumption more certain.

1.1.3 Autonomy in Uncertain Environments

While the tight coupling between small UAS and the environment makes this a particularly interesting application, the problem of navigating uncertain and random environments is common to many autonomous systems. Representing a complex environment without using an overly-specific model and building this model with *in situ* observations is a common need for autonomous systems.

Unless the objective is to map an environment, a model alone is not enough. A detailed map of the atmospheric state is not by itself enough to evaluate the cost of reaching a point or the certainty in that cost. It is important that the model employed by an autonomous aircraft can be easily transformed to compute the impact the environment has on the aircraft, and that the confidence in this effect

can also be determined.

When a vehicle must build a map from *in situ* observations it faces a choice between gathering information to identify favorable regions and flying in known areas of low travel cost. This problem is commonly known as the exploration-exploitation dilemma [12]. It has been explored in a number of applications, but the environmental structure and needs of solar aircraft poses an explore-exploit problem with some novel features. The nonstationarity of the environment, continuous exploration space, and high degree of coupling between the vehicle and environment make this a particularly challenging problem.

1.2 Design Goals

The big picture problem this thesis seeks to solve is illustrated in Figure 1.4. A solar augmented aircraft travels a long distance (such that its environment cannot be assumed to be stationary). Some imperfect *a priori* information about the state and evolution of the environment may be available at the beginning of the mission and the aircraft can observe the wind vector and solar insolation at its location. The aircraft's objective is to reach a desired point while minimizing energy consumption by intelligently controlling its speed and use of stored energy. To simplify the planning problem, this thesis restricts environmental modeling and flight planning to the vertical plane. This restriction is consistent with the limitations of *in situ* observations – the atmosphere generally forms in strata so a series of observations reveals more information about the best altitude to fly at than the best lateral flight path.

Because information about the environment is uncertain, strict adherence to a preplanned flight path is not likely to be optimal. A path planned *a priori* may direct the aircraft to fly through a cloud or headwind layer that is either not anticipated or forms at an altitude or time other than expected. Further, there may be random variations in the environment which cannot be predicted. The aircraft should build a map of its environment and decide how to respond to the mean environmental state and to random fluctuations in a way that minimizes expenditure of stored energy.

The autonomy guiding a low altitude solar augmented aircraft should meet several criteria:

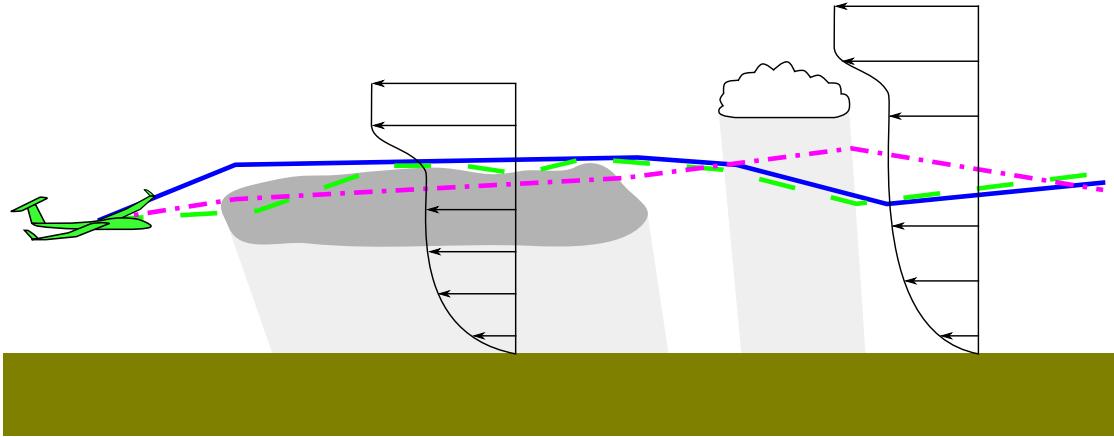


Figure 1.4: An aircraft flying in a random and uncertain environment must decide how to schedule its speed and power output to minimize energy expended in flight. The solid line represents a notional optimal path that cannot be determined without perfect knowledge. The dash-dot line represents a path planned using *a priori* information which includes suboptimal portions due to forecast error and stochastic phenomena. Finally, the dashed line indicates the objective – a (possibly suboptimal) path which balances mapping the environment with saving energy. The act of maintaining an environmental model requires expending energy but the knowledge gained can allow the aircraft to avoid costly errors.

- Minimize expenditure of stored energy and reduce uncertainty in energy used.
- Be capable of operating with little to no communication with outside systems.
- Determine a course of action from information available *in situ*.
- Improve in performance if exogenous information is available.
- Respect constraints imposed by an operator and provide feedback on the cost of constraints.

The first goal is relatively straightforward. The utility of an aircraft is often restricted by the amount of energy it can carry. Whether a mission objective requires the aircraft to carry a payload, reach a location, or orbit a point, its ability to accomplish this mission is constrained by its energy budget. Solar-electric aircraft have limited energy budgets with significant uncertainty. This has the double impact of limiting utility and making the capability uncertain, requiring larger reserves to ensure that enough energy is available to complete a mission.

Reducing energy consumption and increasing confidence in the expected energy required to complete a mission both have the effect of increasing an aircraft's usable energy budget and improving its utility.

The second goal is motivated by several needs. First, the aircraft should be capable of safe and intelligent flight even if communication is lost. This also allows the aircraft to operate in remote areas where communication is limited or unavailable. The ability to operate independently also improves the scalability of a system – if every aircraft requires a very high bandwidth data link then not many can be operated simultaneously. This goal requires that the aircraft be capable of making decisions using processing resources available on the aircraft and with information either uploaded preflight or obtained by the aircraft in flight.

The third goal is motivated partly by communications independence, but also by the nature of the environment at low altitudes. The scale of phenomena resolved by numerical weather models and the skill of weather forecasts leaves significant uncertainty in the optimal flight path and energy required to complete a mission. Regardless of the link budget for providing flight plans or weather data, using *in situ* observations has the potential to improve aircraft guidance by observing stochastic features of the environment and error in a forecast.

Observations from onboard a single aircraft are necessarily limited in their spatial scope and prognostic value. Observations from other aircraft or sensors can reduce the need for exploration. Updated forecast information can also reduce error in the aircraft's *a priori* knowledge of its environment and energy budget. Improvements in environmental knowledge and reduced need for exploration can enable more intelligent and energy-efficient decisions to be made. The decision and control system should be designed in a way that permits incorporating additional information available from offboard sources if it is available.

Finally, the aircraft should be capable of respecting mission constraints. Even small electric UAS are fairly complicated and expensive pieces of equipment. They will be used by operators whose figures of merit are related to mission objectives, not to aircraft operational details. An aircraft system which can fly indefinitely but requires an indefinite time to reach a goal point has limited utility, the ability to reposition to a region of interest without requiring ground infrastructure is a major advantage that UAS offer over balloons, kites, and towers. This makes it important to minimize energy while satisfying a schedule. The operator may also desire the

aircraft to be at a given altitude to satisfy a sensing objective or to deconflict with other aircraft. Some constraints may not be hard thresholds, if utility degrades smoothly as a constraint is violated then it is desirable that the autonomy system provide feedback on the operational cost of compliance with a proposed mission constraint.

As long range flight by small UAS (and especially small solar UAS) is a relatively new endeavor, there does not currently exist practical or theoretical tools solving this suite of problems. Section 2 discusses the current state of the art in solar aircraft planning and relevant work in other fields. This prior work does not provide a comprehensive solution to these autonomy design goals, motivating the need this thesis.

1.3 Primary Research Contributions and Reader's Guide

The contributions of this research are in several areas:

- Identifying the design space and operating environment for solar augmented aircraft.
- Demonstrating that optimal control of the speed and motor power output can be decoupled.
- Developing a control policy to schedule speed that minimizes power consumption while meeting mission constraints.
- Modeling the environment from information available *in situ* in order to enable autonomous decision making.
- Determining the optimal altitude and power output, taking into consideration the value of exploring altitudes where the environmental conditions are uncertain.

This thesis begins in Section 2 by reviewing literature relevant to small UAS, solar aircraft, and energy exploitation from the atmosphere. Previous work relevant to trajectory planning, environmental representation, and sampling strategy are

also examined. The shortcomings of existing methods with respect to the autonomy design goals are highlighted.

Section 3 reviews the operating environment for small UAS at low altitudes with special regard for solar aircraft. Relevant aircraft motion and energetic equations are reviewed, and several aircraft models are described which will be used throughout this work.

As most of the literature on solar aircraft focuses on high altitude pseudosatellites, it is important to carefully define what a solar augmented aircraft is, its design and operating space, and the characteristics shared with and distinct from other UAS. Section 4 explores the impact of relaxing the requirement of pure and persistent solar flight, as well as the impact environmental variations have on small UAS and especially solar powered UAS.

Section 5 demonstrates that speed and utilization of stored energy can be optimized separately. A speed scheduling policy is developed that determines the optimal response to stochastic energy input from multiple sources while meeting mission constraints. The control policy is demonstrated in both simulation and flight experiments.

Section 6 builds on the author's Master's work in developing a general representation of the vertical structure of the atmosphere, building the model from *in situ* observations. A method for relating the atmospheric model to the aircraft's travel cost is developed. The modeling system is demonstrated in flight test and validated against weather balloon observations and numerical weather predictions.

In Section 7, a method for optimizing altitude is developed. This method balances exploring the atmospheric profile with energy reduction by flying at the minimum energy altitude. The problem of altitude optimization from *in situ* observed conditions has novel features compared to previous explore-exploit problems. The utility of the proposed solution is compared in simulation to optimal paths computed with perfect knowledge, defining the cost of maintaining a model of the environment and benefits of using the model to make decisions *in situ*.

Chapter 2 | Review of Relevant Literature

The preceding chapter described a need faced by an emerging class of small UAS, this chapter reviews relevant work from aircraft flight planning, environment modeling, and allocation theory.

2.1 Trajectory Planning

Trajectory planning is a topic of considerable interest to a wide variety of vehicles. The field covers everything from coverage patterns for vacuum cleaners [13] to intercontinental navigation for commercial aircraft [14]. The proliferation of small autonomous systems has only further increased interest in planning methods that can be used in complex environments and run on low performance computers.

2.1.1 Robotic Motion Planning

Enabled in large part by sensing and computing technology developed for smartphones, mobile autonomous robots have proliferated in the past decade. The push for more capable and autonomous systems has driven considerable research in robotic motion planning [15]. Interest in small UAS has also brought attention to the specialized needs of robotic aircraft [16].

Robotic motion planning is typically concerned with finding trajectories through obstacle cluttered environments. This imposes constraints on the problem distinct from those under consideration here. Finding feasible trajectories (which do not intersect obstacles) for the aircraft considered here is almost trivial as the density of obstacles higher than one hundred meters tall is very low. Uncertainty exists not in the location of obstacles in the environment, but in the cost to traverse the environment. Common robotics planning algorithms such as A*, tree-based

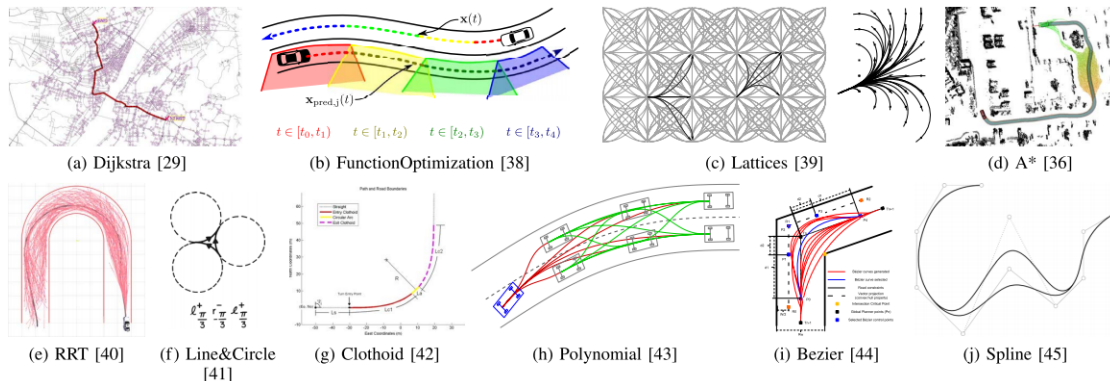


Figure 2.1: Environment representation and motion primitives for a number of robotic planning techniques. Reproduced from González et al. (2016) “A Review of Motion Planning Techniques for Automated Vehicles” [15].

algorithms, roadmaps, and Dubin’s car planners are capable of finding optimal routes under these conditions. However, these approaches are not well suited to planning routes robust to uncertainty in the travel cost. Many of these planners also rely on encountering impassable regions to prune the search space, making them slow to plan optimal routes in the absence of obstacles.

2.1.2 Long Range Aircraft Path Planning

Planning long-range flight in varying weather conditions is not a problem unique to small UAS or to solar aircraft, although their tight coupling to the environment, slow speed, and limited power budget makes it more important. The problem of optimal navigation in a wind field has a history dating to the Zermelo problem from the 1930s which examined optimal travel for a boat navigating a current [17].

More recently, a number of authors have investigated planning methods in complex time and spatially varying fields. Jardin and Bryson develop a technique using neighboring optimal control to plan paths through known spatially varying wind fields and derive feedback gains that can be used to compensate for small perturbations in the field as the aircraft flies [18]. Otte, et al. developed an anytime method to plan through a known field, permitting successive refinement of an initial path as time allows [19].

Several authors have directly addressed planning for aircraft which harvest energy from the environment. Chakrabarty and Langelaan developed a kinematic

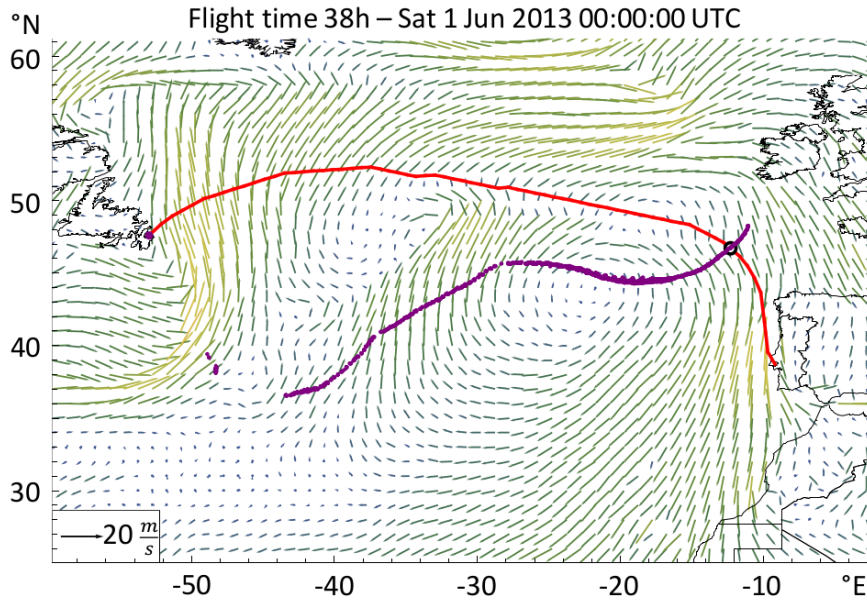


Figure 2.2: Optimized flight path for a solar UAS mission from Newfoundland to Portugal. The purple contour joins locations with equal cost to reach. Reproduced from Wirth et al. (2015) “Meteorological Path Planning Using Dynamic Programming for a Solar-Powered UAV” [22].

tree technique to plan an optimal path through a time and space varying wind field, gathering energy from updrafts along the way [20]. Dai applies the Bellman-Ford algorithm to maps of solar irradiance to maximize the solar energy gathered by an aircraft [21]. Wirth et al. use a decision tree approach to plan transatlantic paths for a solar powered UAS, minimizing a total cost which includes both battery energy and safety of flight parameters [22].

These techniques provide a means to plan energy optimal paths, but do so assuming that there is no uncertainty in the planning field. Other authors have examined energy optimal planning in uncertain fields. Al-Sabban et al. use a Markov decision process to plan through an environment where the wind at each cell is represented by a Gaussian distribution [23]. Cheung et al. use an ensemble of weather predictions to approximate the distribution of energy required to complete a long-range flight but do not address planning to manage this uncertainty [14]. Steiner et al. use a weather forecasting ensemble to forecast air transport delays by computing the distribution of weather-induced reduction in air route capacity [24]. They note that the approach could be used to define a map of regions where hazards

(or beneficial conditions) exist with high confidence and a conventional planner applied – similar to thresholding obstacle belief maps.

Stochastic collocation has emerged as a powerful approach to plan trajectories that are robust to random perturbations [25]. This involves writing the stochastic components of the system as inputs then decomposing these random inputs into a set of deterministically chosen vectors that describe the input distribution. A deterministic solution to the system equation can be computed for each of these input vectors, and the distribution of the state and output vector recovered. This approach is analogous to the Unscented Transform approach to computing the covariance of the output of a nonlinear system subject to Gaussian inputs by propagating “sigma points.” In stochastic collocation, the state distribution can be penalized by an optimal control planner as part of the cost function to produce trajectories that are both low-cost and likely.

Several authors have employed stochastic collocation in flight planning. González-Arribas et al. directly plan flight paths to manage uncertainty in a combination of arrival time and fuel required [26]. They draw the atmospheric state distribution from an ensemble of weather forecasts and employ optimal control to find trajectories which confidently achieve desired arrival times and minimum fuel burn. Flanzer et al. use stochastic collocation to develop dynamic soaring orbits which are robust to aircraft model and initial condition errors [27]. The approach can quantify the likely flight path perturbations (Figure 2.3) and which are penalized in the cost function to produce trajectories which are much more likely to sustain flight than a deterministic optimal control planner.

Decomposing the random input vector has a cost however – the system dynamics must be computed for each input vector. The number of points in the decomposition grows rapidly with the number of random inputs [28]. While sparse point selection can reduce this cost somewhat, the number of trajectories which must be solved is still several times more than a deterministic planner. This can make stochastic collocation challenging to employ using the computational resources available onboard an aircraft.

Stochastic collocation has another weakness shared with any *a priori* planning approach – it produces trajectories robust to random disturbances but it cannot respond to observed realizations of these disturbances. Using a receding horizon controller offers one approach to incorporate the observed environment, but requires

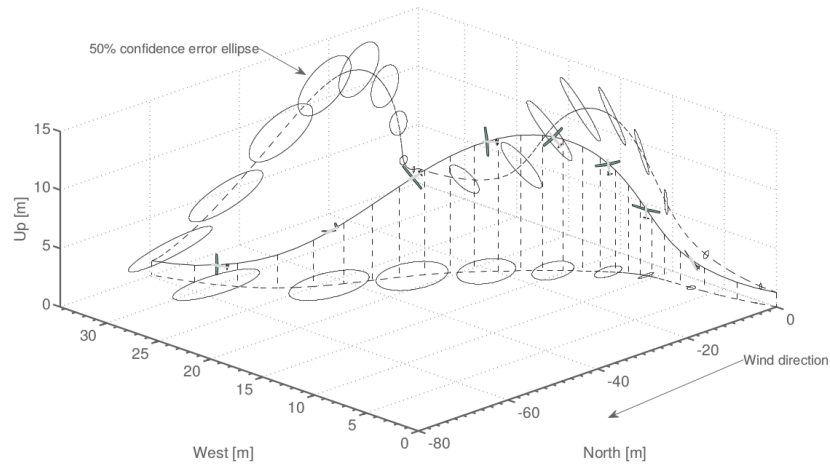


Figure 2.3: Stochastic collocation can be used to quantify trajectory perturbations introduced by environmental uncertainty. This uncertainty can be penalized in the cost function of an optimal control formulation to produce robust trajectories. Reproduced from Flanzer et al. (2012) “Robust Trajectory Optimization for Dynamic Soaring” [27].

a fast optimal control formulation to run continuously.

Computational challenges aside, any planner needs a realistic representation of the environment. To employ a planner robust to uncertainty, this representation must describe not only the mean state but its distribution. Existing approaches require that the entire field and its uncertainty is known *a priori*. An aircraft with no prior information or information old enough to have degraded significantly cannot make intelligent decisions using existing approaches.

There are also stochastic variations in the atmospheric environment that are not resolved by weather forecasts at all. Clouds and wind field perturbations introduced by convection and terrain can have a significant impact on the energy budget of small UAS but will not be addressed by even robust *a priori* planners as these features are often below the resolved scale of weather models. Increasing grid resolution of weather forecasts does not offer an immediate solution. Higher resolution does make the features produced by numerical weather prediction systems more realistic, but position and timing errors in the features resolved make planning for these features challenging [11].

In the long-term UAS may help solve these problems by gathering the high resolution observations needed to correctly place features in weather models. This

is only a viable approach in areas densely traveled by UAS, requires a constant high bandwidth data link, and faces a “bootstrapping” problem of getting UAS reliably and ubiquitously into the air in the first place.

2.1.3 Solar Aircraft Flight Planning

Optimal control approaches used for flight planning can be applied specifically to solar aircraft. A number of authors have examined maneuvering solar aircraft to maximize the illumination of solar arrays. Klesh and Kabamba used an optimal control approach to determine a bank angle and velocity schedule which reaches a desired point while maximizing energy by orienting the solar arrays favorably to the sun [29]. Dai et al. construct the aircraft kinematics using quaternions and employ quadratic programming to maximize array illumination when maneuvering [30]. Hosseini and Mesbahi examine trajectory generation with the addition of a surveillance cost, to maximize both energy gathered and coverage of a surveillance area [31]. They use the results from solving a nonlinear programming problem to develop a state machine for energy management and introduce a technique to learn the optimal open-loop climb rate command to use in the state machine. Edwards et al. develop a method to compute the optimal turn radius when exploiting a mix of both vertical air motion and solar energy [32]. Finally, Martin et al. use a collocation based optimal planner to determine optimal solar gathering trajectories subject to a station keeping constraint [33].

This previous work provides a number of approaches that can generally be classed as planning to maximize solar array illumination. While some of the papers address optimal trajectories over the course of a day, the constraints imposed typically require the aircraft to perform some type of station keeping, so that these solutions are often repeated applications of short range planners. With the exception of Hosseini and Mesbahi, the environment is assumed to be known perfectly *a priori*. Even in their paper, stochastic solar input is only considered when selecting an open-loop climb rate when simplifying their nonlinear programming solution to a state machine.

The primary weakness with the planning methods described here is that they do not address the uncertain and stochastic nature of solar energy availability in the troposphere. This could be ameliorated to some degree by the application of

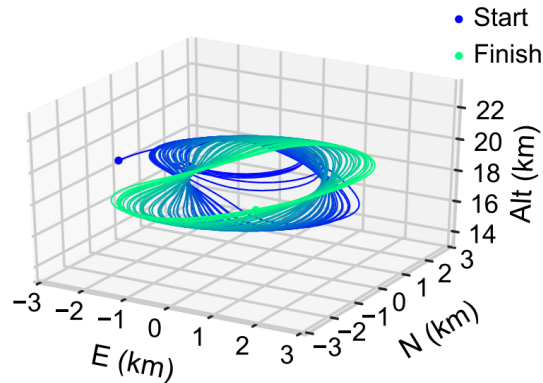


Figure 2.4: Evolution of the optimal flight path for a solar aircraft keeping station near a point. The long axis of the flight path tracks the vector to the sun projected on the ground plane. Reproduced from Martin et al. “Dynamic Optimization of High-Altitude Solar Aircraft Trajectories Under Station-Keeping Constraints” (2018) [33]

stochastic collocation or if the planners are rapid enough to be run onboard using *in situ* observation of the solar energy available. Stochastic collocation cannot address unresolved atmospheric properties however, and while it can provide a path robust to uncertainty in the *a priori* belief of the environmental state, it cannot seek out information in the realized state of the environment and respond to this information. Even a planner rapid enough to run on board using *in situ* observations requires heuristic choices be made about how to weight the value of seeking information and still cannot respond to short-period stochastic perturbations in the environment.

2.1.4 Soaring as a Stochastic Planning Problem

The weaknesses in existing planning techniques for small UAS and solar aircraft can largely be classified into two categories. First, forecast error in the mean state and structure of the atmosphere can lead to suboptimal routes or altitude guidance. Second, there will be stochastic variations in the energy available to a small UAS which can not be forecast *a priori* either because they are on a scale which is not resolved by weather forecast models, or because it is not possible to forecast the exact time and location at which the variations will occur. This is particularly true of intermittent solar input caused by scattered clouds in the lower troposphere and of disturbances caused by vertical air motion in a convective boundary layer.

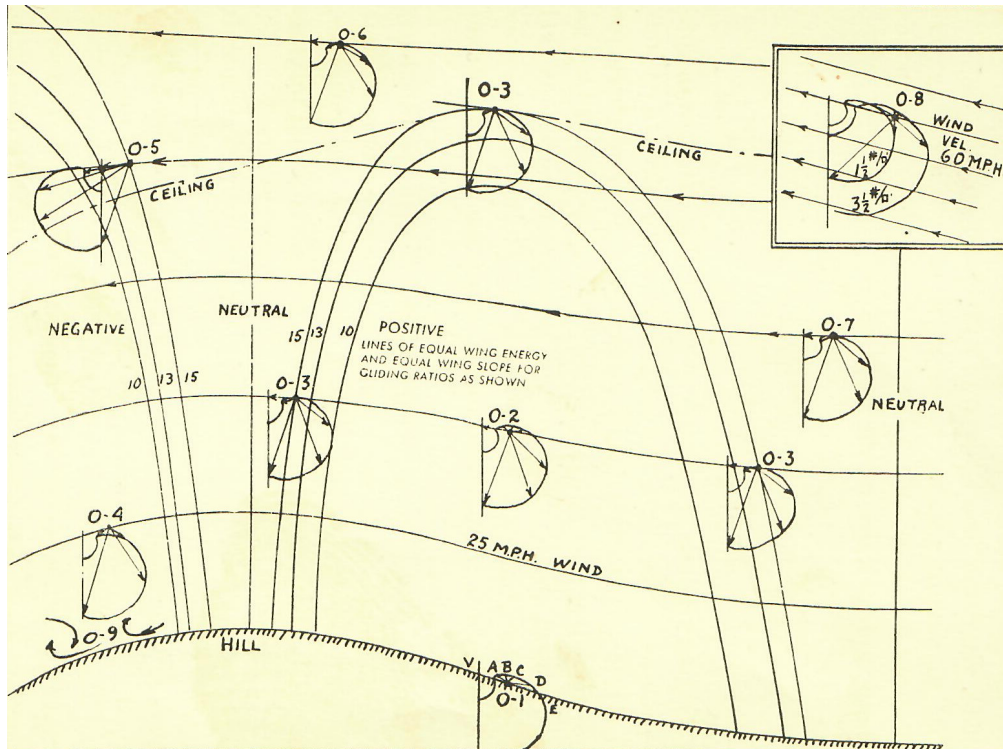


Figure 2.5: Speed to fly computed for a spatially varying wind field near a hill. Reproduced from Barnaby (1930) “Gliders and Gliding” [36].

Since the 1920s sailplane pilots have been concerned with selecting the speed that maximizes the range of unpowered aircraft in stochastic fields of up- and downdrafts [34–36]. The classic solution to speed to fly theory is developed for an aircraft which occasionally “stops” and circles in regions where it can gain energy before continuing its mission. Several extensions have been developed which enable speed to fly to be applied to a continuous flight. Arho [37] examined optimal soaring as a sequence of responses to environmental inputs and de Jong [38] generalized the aircraft performance model in a way that permits climbing and cruising flight to be treated identically.

It is not clear how to apply soaring speed to fly theory to solar flight however. Speed to fly solutions are parameterized by the “MacCready number,” which represents the power available during brief and isolated energy harvesting periods. For solar aircraft which continuously harvest energy, it is not clear how to define the MacCready number – there is no isolated energy harvesting period. Further, it would be desirable to satisfy the objectives of an outer loop planner or a mission

operator who specifies a time enroute to a destination, this is not possible with conventional speed to fly theory. Finally, as the magnitude of vertical air motion and solar energy input are of similar order, it would be desirable to have a means to combine exploitation of the two.

2.2 Environmental Modeling

In order to respond intelligently to the environment, the aircraft needs a representation of the environment that can be carried with it and maintained onboard. Because planning is restricted to the vertical plane in this work, this means a profile of the atmospheric conditions which are relevant to aircraft performance. The method employed to represent the environment should permit fusing observations taken on the aircraft with those taken by other aircraft, ground based sensors, or satellites. It should also permit information from numerical weather models to be incorporated.

A number of authors have examined building maps of the environment around an aircraft. Lawrance and Sukkarieh used Gaussian process regression to model the winds around a small aircraft and plan optimal flight paths [39]. Depenbusch et al. used a grid of one state Kalman Filters to estimate a 2-d map of updrafts [40]. This permitted a small UAS to find thermals and climb without running its motor. Bird used basis splines to model the vertical wind structure for dynamic soaring [41].

Glasheen et al. evaluated high resolution weather forecasts as a way to provide the aircraft with an environmental model [42]. Recognizing issues with boundary conditions, position, and timing of forecast phenomena they compare the distributions of relevant atmospheric properties observed by the aircraft to those forecast by a large eddy simulation. The results show systematic differences between forecast and observed conditions, identifying a need for using *in situ* observations to provide calibration to forecasts.

Several authors have sought to bridge this gap by assimilating observations from small UAS into a weather model [43] [44]. This is a promising approach, current efforts have reduced wind forecast error by approximately 10%. There are some operational disadvantages to the approach however; it requires constant communication between the aircraft and ground, and the aircraft cannot make use of its observations until a subsequent model analysis or forecast is complete

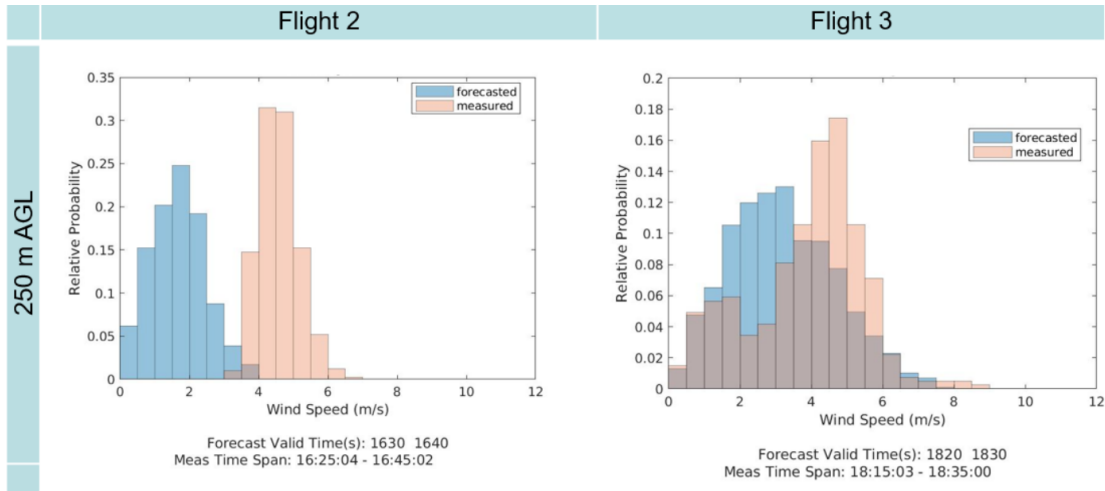


Figure 2.6: Systematic errors in the wind forecast observed in flight tests. Reproduced from Glasheen et al. (2019) “Experimental Assessment of Local Weather Forecasts for Small Unmanned Aircraft Flight” [42].

and transmitted back to the aircraft. This approach also does not address how to include and respond to subgrid-scale perturbations

On a more fundamental level, there may be limits to the error which can be eliminated using data assimilation. A small number of observations may not be sufficient to correct the state of a numerical weather model, especially if an error is caused by unmodeled dynamics or large-scale error in the boundary conditions. The dimension of the atmospheric state tracked by a numerical weather model is very large (order 10^7), so it is not feasible to fully describe the covariance between states or between an observation and all states. While a few observations may provide meaningful information about the entire atmosphere, if the correlation between that observation and distant states is not known, then the model cannot fully reflect the impact of the observation. For instance the forecast position of a cold front has significant implications for the entire atmospheric state on a large scale, but a few UAS observations that the front is moving faster (or slower) than expected may not be enough to force adjustment in the entire field of a weather model.

Oetersshagen et al. employ a diagnostic flow solver onboard an aircraft to solve potential flow equations over complex terrain [45]. This produces high resolution and rapidly updated predictions of horizontal and vertical air motion without coupling observations back into the dynamics of the atmosphere on a large scale.

This approach is promising for identifying and exploiting orographically induced winds at high resolution, but does not address responding to perturbations from other atmospheric processes or variations in solar energy.

Frew et al. describe a system for combining *a priori* forecasts with aircraft observations and remote sensing to enable intelligent response to complex atmospheric environments [46]. The approach divides the computational load between the aircraft and a ground station: the aircraft builds a Gaussian Process model of its immediate environment and employs receding horizon control; the ground station fuses multiple data sources and provides long-range guidance. In concept, the division made between local planning on the aircraft and global planning performed offboard is similar to the objective of independent planning in support of a human operator or autonomous tasking system identified in Section 1.2. Frew et al. model only the very-near environment on the aircraft however, limiting the vehicle’s independence and ability to operate in remote areas. Use of Gaussian Processes to model the local environment in 3-D permits accurate description of the environment and allows the aircraft to make detailed flight plans, but variations in the wind field are not correlated at scales longer than one-half of the boundary layer depth (order one kilometer) [47], limiting the range over which this planner can operate.

2.3 Exploration vs Exploitation

Even in an environment with no stochasticity the decision-making system needs a way to address error in its knowledge of the mean atmospheric state. This error could be introduced by large-scale unmodeled dynamics, by subgrid-scale phenomena, or by the interaction of unresolved and resolved scale processes. If the aircraft is permitted to change altitudes to maintain its environmental knowledge or to reach a more favorable environment, then planning can be viewed as an exploration vs exploitation problem.

2.3.1 Sensor Placement

One approach to solving this problem is to minimize energy consumption while maximizing knowledge about the environment. This is a sensor placement problem

where the goal is to maximize information while minimizing the sensor purchase and placement budget. Krause et al. developed a sensor placement algorithm which maximizes mutual information between the observed and underlying distributions. The algorithm can rapidly achieve results close to the optimal solution [48]. DeVries et al. use empirical observability to locate sensors in highly informative regions so that a fixed number of observations maximized knowledge of the environment [49].

There is one significant difference between the aircraft navigation and sensor placement problem however – there is no explicit need to maximize environmental knowledge in the aircraft navigation problem. A high quality map of the environment is only valuable in so far as it permits selecting the best route of flight. This necessitates selection of some heuristic in order to balance the trade of energy for information. Selection of this heuristic becomes a very important design choice, one which is difficult to accomplish in a principled way and which makes communicating the value of exploration and rationale for selecting a flight path to an operator or autonomous monitoring system difficult.

2.3.2 Multi-Armed Bandits

The problem of choosing an action that balances information and reward gain when information is only valuable as a means to select high-reward actions is generally referred to as a “multi-armed bandit” [50, 51]. The canonical form of this problem proceeds in rounds. In each round an action is chosen from a set of possible actions $x_i \in X = \{x_1, x_2, \dots, x_n\}$ known as “arms.” Each action (“pulling” an arm) confers an reward which is unknown *a priori* and may be drawn from a random distribution. The objective is to maximize the total reward by choosing the arm which confers the greatest reward $x_\star = \arg \max_x J(x)$. At each round there is a tradeoff between the cost of exploring (requiring the play of arms which have uncertain reward) and the best known arm.

There are a number of solutions to the classical multi-armed bandit problem. An algorithm is said to “solve” the bandit problem if its regret (cost relative to an “oracle” planner with perfect knowledge) grows with $\mathcal{O}(\log T)$ where T is the number of rounds [50]. Lai and Robbins devised the first general solution, assuming that the space of arms X is finite and that the reward distribution does not change [52]. A particularly interesting solution is the POKER algorithm which affixes a price to

the information which can be gained by playing an arm and includes that price in the expected reward [51].

Many other versions of the bandit problem have been formulated. Of particular interest here is the continuum bandit (where X is not finite but a continuous function) [53,54] and the nonstationary bandit (where the reward distribution $J(x_i)$ changes in time) [55–58]

In the continuum bandit problem actions are drawn from a continuous space $x_i \in [x_{min}, x_{max}]$. This introduces the complication that the action space can never be completely explored, equivalent to having a discrete action space with an infinite number of arms. If the reward is a continuous function of the actions then the problem becomes tractable. The typical way to solve the continuum bandit problem is to discretize the environment into regions and apply a conventional bandit approach over the discretized action-reward space [54]. This approach introduces another source of regret from the error in approximating the environment, so its regret scales with $\mathcal{O}(\sqrt{T})$ [53].

In the nonstationary bandit problem the reward distribution $J(x_i)$ changes in time. This is a particularly challenging problem as information about previous “pulls” of a particular arm become less and less relevant. Continuous exploration is required and explore-then-exploit approaches are not appropriate. Adaptations to a number of algorithms have been proposed to force continued exploration, but these generally require some exploration heuristic [55]. Slivkins and Upfal show that the regret for a finite-armed case where the reward of each arm follows a Brownian motion is lower bounded by $k\sigma^2$ where k is the number of arms and σ^2 is the process noise.

The configuration of the problem – information degrading and the background environment changing suggests that a Bayesian approach to monitoring and selecting actions might be appropriate. Granmo and Berg took this approach, tracking the value of a each arm of a finite-armed bandit with a Kalman Filter and selecting arm with the greatest expected value [57]. This approach demonstrated good performance, but is developed only for discrete domains and for problems where the number of rounds is very large.

2.4 Summary

Robotic motion planning under uncertainty is a well-studied field but the constraints and objectives of aircraft in cruising flight are distinct from those faced by many other robots. A cruising aircraft has a relatively unrestricted search space but the cost to traverse points in the domain can vary significantly with space and time. Optimal control planners perform well in these situations, though their typical formulation cannot address uncertainty in the environment. Stochastic collocation offers an optimal control approach which can manage uncertainty in the system but requires significantly more function evaluations. Regardless of the approach taken, planners which operate *a priori* are not able to incorporate knowledge gained about the realized state of the environment as the aircraft carries out a mission.

Flight planning for solar powered aircraft has also been the subject of several investigations, but the focus has been almost exclusively on maximizing illumination of the solar array. This is a reasonable approach for high altitude aircraft, when the energy variation is dominated by array pointing. At low altitudes clouds can reduce energy production more than suboptimal array orientation so investigation into approaches for dealing with interruptions in energy is required.

Regardless of whether a deterministic or probabilistic planner is used, an accurate representation of the environment is required. Especially for UAS operating at low altitudes, determining the environmental state to high accuracy before flight is not possible.

This makes *in situ* environmental modeling an appealing technique. Several authors have explored building maps onboard the aircraft. Most of these maps were only suitable for operations in small areas either because of limited domains or because the cost of building the model was impractical for long flights. Assimilating aircraft observations into numerical weather prediction models offers one way to provide longer-range awareness but requires constant high-bandwidth links to offboard computational resources. To operate reliably in challenging conditions and remote areas an aircraft will need to be able to make atmospherically aware decisions using only resources available before flight and onboard the aircraft.

Finally, making tradeoffs between gaining information and optimally accomplishing a mission is a challenging problem. Sensor placement approaches put demands on the system designer to choose heuristics that balance mission performance and

information. The multi-armed bandit framework better describes the needs of an independently operating aircraft, but existing formulations of the approach do not work for continuous, time-varying reward domains.

Chapter 3 | Environment, Models, and Platforms

To help frame the developments detailed in this thesis, this chapter describes the operational environment the autonomous system is designed to operate in. The aircraft dynamics and aircraft models used in simulation are described as well as the aircraft platforms used in simulation and flight tests.

3.1 Relevant Characteristics of the Lower Atmosphere

For the purposes of this work the aircraft is confined to relatively low altitudes. It is important to clarify what “low altitude” means in order to understand the implications of this choice. The motivation for flying at low altitude is driven by vehicle design and operational constraints, so this region will not correspond exactly to a unique dynamical region of the atmosphere.

- The aircraft must be permitted to fly below the lowest layer of clouds if required for imaging. In cases of fog this may not be achievable, so the lower limit should be motivated by terrain and obstacle clearance, to roughly 100 meters above ground level (AGL).
- The aircraft should be permitted to fly within the planetary boundary layer to sample weather conditions or trace chemicals in the atmosphere. This means the aircraft should be permitted to fly below 1-3 kilometers AGL.
- When imaging or sampling constraints are not in place the aircraft should be permitted to climb as high as practicable in search of favorable regions for cruise or loiter.

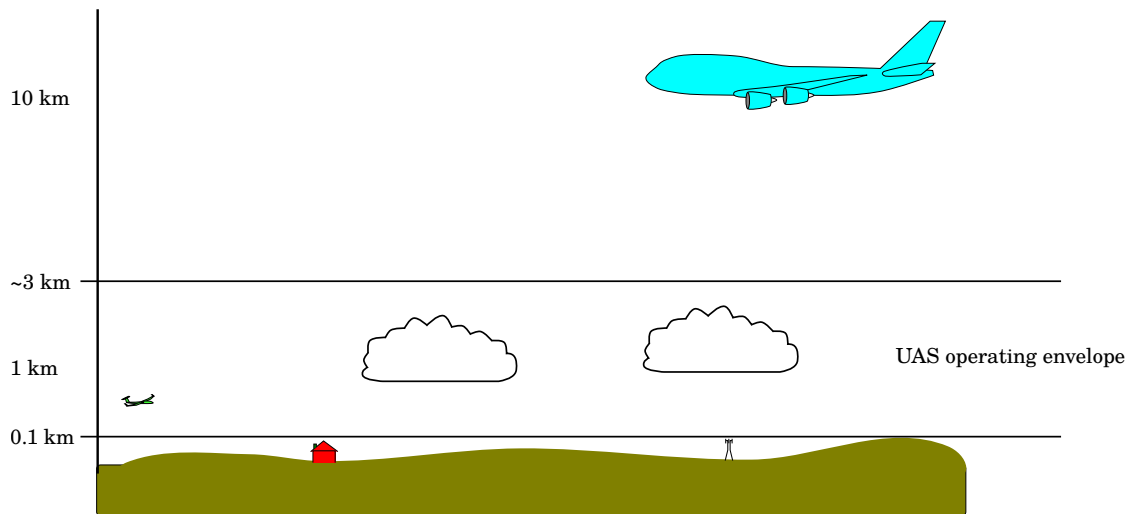


Figure 3.1: Most small aircraft operations take place between 100 m above ground and 3 kilometers above sea level. This provides separation from most transport aircraft, permits high resolution imaging, and avoids many obstacles.

- Large, fast commercial and tactical aircraft typically fly at above 3 km. While air traffic control systems exist to provide separation, it becomes more challenging as the relative speed increases. Given the slow speeds of small UAS it is desirable to keep them clear of larger and faster aircraft.

These considerations motivate a permitted altitude band ranging from approximately 100 meters above the surface up to 3 kilometers above sea level. While this definition breaks down in mountainous regions or over high altitude plateaus, for most of the world this provides a band which is responsive to the criteria listed. From a meteorological perspective this means that the aircraft could fly within the atmospheric boundary layer and the overlying free troposphere, but not up to the tropopause. To help frame the research problem, a brief overview of this environment and its influence on the aircraft's energy budget is provided

3.1.1 Clouds

Several cloud formation mechanisms and structures occur in this operating environment (Figure 3.2). The majority of clouds below 3 km are formed either by convective lifting induced by surface heating, by lifting associated with frontal systems, or by advection of moist air [59].

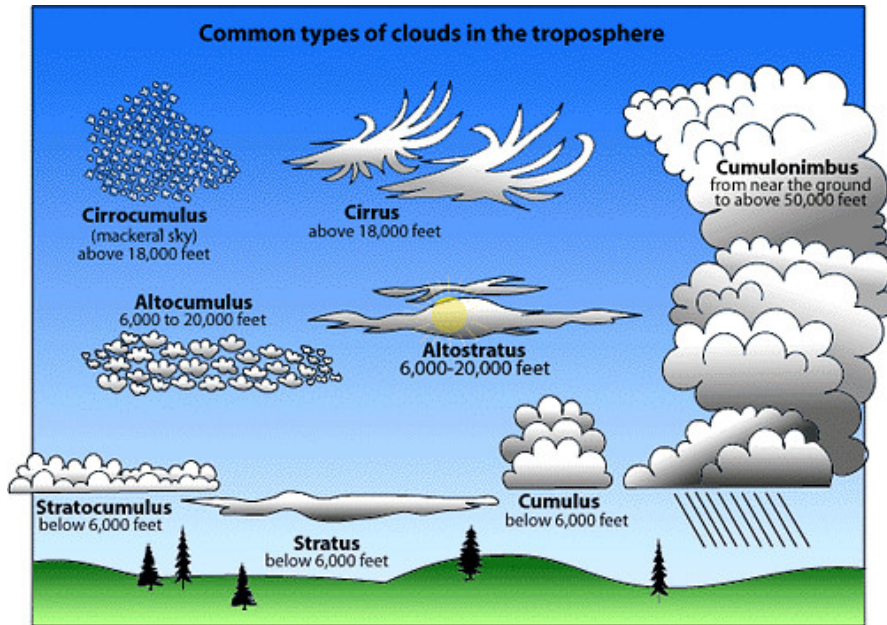


Figure 3.2: Several cloud types occur in the the operating envelope of small UAS. Reproduced from University Center for Atmospheric Research (2012) “Cloud Types | UCAR Center for Science Education” [60].

Cumuliform, or convectively driven clouds typically form at the top of a convective boundary layer. These clouds can form in single formations (cumulus humilis), sky covering layers (stratocumulus), or large formations associated with storms (cumulus congestus and cumulonimbus). They will typically have spatial and temporal scale smaller than the resolution of weather models. The average impact they have on the surface radiation and heat budget is forecast, but their individual location, lifespan, and influence cannot be predicted. Any response to these clouds will have to be based on *in situ* observations.

Stratiform clouds are formed by broad uplifting of air until it condenses, often associated with either warm fronts or with advection of moist air up a slope [59]. Because stratiform clouds are associated with large meso- to synoptic-scale weather features, their presence and extent can be forecast more precisely. Uncertainty in the moisture field at low altitude or with the position and timing of the warm front or advecting winds can introduce error in their precise location and altitude. This again makes an aircraft response based on *in situ* observation desirable as a means to respond to stratiform clouds.

In addition to clouds at the aircraft altitude, altocumulus and cirrus clouds

can form above the altitude band examined in this work. These clouds will have the effect of modulating the overall solar energy available to the aircraft without changing the level at which the aircraft harvests the most solar energy.

3.1.2 Winds

Winds have a significant and ubiquitous impact on the performance of all aircraft. The slowest aircraft, such as small UAS are especially affected. Even in the lower atmosphere, winds exceeding 15 m s^{-1} regularly occur – the same magnitude as the cruise speed of many small UAS. Understanding and responding appropriately to the wind environment is important to intelligent flight of all aircraft.

Wind patterns in the atmosphere are generally driven by synoptic-scale pressure gradients. The pressure gradients and Coriolis force interact to create the geostrophic wind that circulates around centers of high and low pressure. At the surface, the wind loses momentum to surface friction, reducing its velocity and changing its direction as the pressure gradient and Coriolis force balance is altered [59]. These interactions give rise to several patterns of vertical structure in the wind which can occur in the low altitude environment.

Within a convective boundary layer eddies can efficiently transfer momentum throughout the boundary layer. Friction at the surface reduces the wind speed, but momentum is constantly mixed down from higher in the boundary layer. This friction causes the entire convective boundary layer to be subgeostrophic – the wind is less than the pressure gradients would indicate. Above the boundary layer there is almost no friction so wind in the mid troposphere is almost geostrophic [59]. Shear between the boundary layer top and the free troposphere mixes momentum down into the boundary layer, though stability in the free troposphere suppresses eddies and slows this mixing. The greatest shear in a convective boundary layer is thus very near the surface (generally where aircraft aren't flying) and at the boundary layer top (where an aircraft trying to stay above the clouds will fly).

Stable boundary layers inhibit momentum transferring eddies associated with convective boundary layers. This makes stable boundary layers much thinner and increases shear near the surface. Stable boundary layers are generally no more than a few hundred meters thick [10] so they are of themselves not particularly consequential for aircraft.

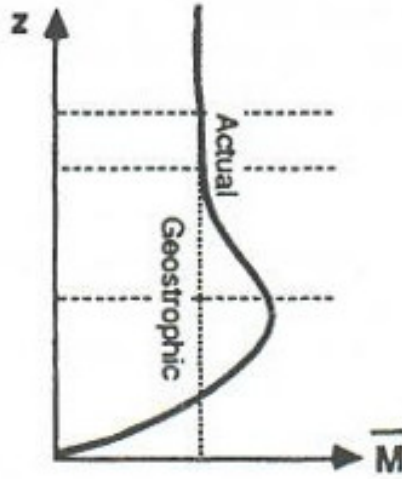


Figure 3.3: Decoupling of the surface and convective boundary layer can create a layer of high speed wind at low altitudes at night. From Stull (1988) “An Introduction to Boundary Layer Meteorology” [10].

One exception to this is the nocturnal low level jet. It forms when a nocturnal temperature inversion decouples the residual daytime convective boundary from the surface [10]. The momentum sink at the surface disappears and the pressure gradient accelerates the overlying air, overshooting geostrophic balance and forming a jet of high speed wind above the nocturnal boundary layer as shown in Figure 3.3

While in general wind varies smoothly, transitions between wind regimes are typically aligned with dynamical regimes in the atmosphere. This means that an error in, for example, the boundary layer depth will create an error in the forecast wind field. Since clouds can also occur at the boundary between dynamical regimes this error can be significant, Figure 3.4 illustrates how an error in the forecast boundary layer depth can significantly affect an aircraft trying to fly above a stratocumulus layer and below a strong headwind. This makes planners which rely solely on *a priori* information brittle as they can give a false indication of the cost to complete a mission.

3.1.3 Vertical Motion

The mean vertical motion in the atmosphere is very small, rarely exceeding 10 cm s^{-1} [61]. Significantly greater vertical motion occurs in small pockets however, often reaching several m s^{-1} – approximately the vertical rate of a small UAS.

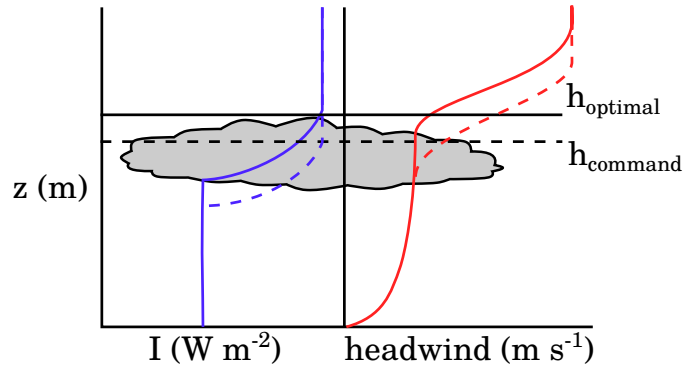


Figure 3.4: A small error in the forecast for the boundary layer depth can impact both the cloud and wind field leading an *a priori* planner to choose a suboptimal altitude. Dashed lines represent the forecast conditions and solid the observed conditions.

This makes exploitation of pockets of significant vertical motion attractive, in fact a number of researchers have demonstrated flights of several hours powered by vertical air motion [62–67].

The most ubiquitous vertical motion is caused by thermals, convective eddies in the boundary layer which transfer heat from the surface and mix it throughout the boundary layer. While thermals can be used by themselves to sustain flight, doing so requires the aircraft to stop and circle to climb. This significantly reduces the speed at which the aircraft progresses toward a goal since roughly 30% of its time is spent circling to gain energy. Because it significantly impacts the aircraft’s mission speed, and thus operational utility, this thesis does not focus on sustaining flight using updrafts alone. The magnitude of these updrafts is comparable to the solar energy which can be gathered on an aircraft and to the aircraft’s sink rate, so it is desirable to be able to exploit this energy as much as possible without having to stop to circle.

3.1.4 Weather Hazards

The modern air transport system is incredibly effective at permitting safe operation in almost any weather condition. The capabilities of transport aircraft de-icing systems, approach guidance, and navigation systems makes it easy to overlook the hazard that weather can pose to aircraft. Small UAS weather capabilities are more comparable to small general aviation aircraft than to transport aircraft, requiring

care to be taken in order to operate safely.

The most significant hazards to small aircraft are icing and thunderstorms. Ice accretion on the aircraft can impact the aircraft weight, center of gravity, and adversely alter the aerodynamic shape. Thunderstorms present heavy precipitation, strong up- and downdrafts, lightning, hail, and often heavy icing. Identifying and avoiding these hazards is an important capability for autonomous aircraft, but it is beyond the scope of this thesis.

3.2 Aircraft Motion and Energetic Models

The primary problems of concern in this work are of guidance rather than control. That is, rather than being concerned with generating actuator commands to achieve a desired aircraft state, the objective is to select the optimal states. From this perspective, the precise dynamics of the vehicle are less important than its gross motion and energetics. This section describes several kinematic and energetic models used throughout this work as well as several exemplar aircraft used in simulation and flight testing.

3.2.1 Aircraft Energetics

For the purposes of this development, it is assumed that most altitude targets are “soft” so that the aircraft can seek favorable conditions and use altitude as its primary energy storage medium [68]. This avoids round-trip charging losses in the battery and ensures that the results are applicable to aircraft equipped with non-renewable energy stores (e.g. primary batteries or a fuel cell). The results are equally applicable when excess solar energy is stored in a rechargeable battery onboard the aircraft provided a round-trip efficiency $\eta_{round-trip}$ is used to account for inefficiencies in charging and discharging. In this case the stored energy can be related to the altitude storage as:

$$e_{altitude} = h = \frac{E_{battery}\eta_{round-trip}}{mg} \quad (3.1)$$

The focus of this work is on straight-line flight segments where the aircraft is traveling to a destination. For efficient aircraft, the aircraft pitch attitude changes relatively little as a function of airspeed, so the effect of aircraft maneuvering on

solar incidence angle is neglected. The details of the solar panels, power electronics, motor, and propeller are simplified by working with the aerodynamic power output due to the solar power harvested (i.e. electrical power produced by the solar array adjusted for the efficiency of the drivetrain and propeller). Since the primary focus is the effect of solar energy on flight path, power harvested by the solar array is written as specific solar power:

$$p_{pv,aero} = \frac{P_{pv}\eta_{propeller}}{mg} = \frac{I\alpha S_{pv}}{mg} \cos(i)\eta_{pv}\eta_{propeller} \quad (3.2)$$

where P_{pv} is the electrical power output from the solar power system, I is the clear sky solar insolation, α is the fraction of incident solar radiation blocked by clouds, i is the solar incidence angle, η_{pv} the solar array efficiency in converting solar radiation into electricity, and $\eta_{propeller}$ the efficiency in converting electrical power into aerodynamic power.

When energy is drawn from onboard storage (such as a battery) to power the aircraft, it supplements the power output from the solar panels. Power output from storage will also be expressed as specific power, and have the appropriate efficiencies applied:

$$p_{output,aero} = \frac{P_{output}\eta_{propeller}}{mg} \quad (3.3)$$

The total specific power available is

$$p_{available} = p_{pv} + p_{output} \quad (3.4)$$

Clearly, if no power is drawn from storage, $p_{output} = 0$.

The aircraft's rate of change of altitude (climb rate) at constant speed is dependent on excess specific power and the vertical component of wind speed [69]:

$$\dot{h} = p_{available} - \frac{Dv}{mg} + w_{wind} = p_{pv} + p_{output} + w_{wind} - \frac{Dv}{mg} \quad (3.5)$$

Where $P_{required} = Dv$ is the aerodynamic power required for steady, constant altitude flight [69]. This explicitly shows the equivalence of vertical air motion, solar power, and stored energy. The drag will be modeled using the *speed polar*, a performance model commonly used in the sailplane community to describe performance [35, 38, 70, 71]. The speed polar relates airspeed to the vertical rate

in a steady-state glide at constant airspeed. It thus represents the relationship between speed and the rate of specific work done on the aircraft by drag:

$$w_s(v) = p_{drag} = \frac{P_{drag}}{mg} = -\frac{Dv}{mg} \quad (3.6)$$

where v is airspeed, D is drag, and w_s is the sink rate, the aircraft's vertical rate with respect to the local air mass in an unpowered glide. Note that the sink rate is always negative but is often referred to colloquially without a sign. In sailplane performance analysis it is common to represent the sink rate with a best-fit second order polynomial [35]:

$$w_s(v) = av^2 + bv + c \quad (3.7)$$

Provided that the polar can be adequately represented by Equation 3.7, this form offers a number of advantages, among them that it can easily be corrected for changes in the mass of an aircraft (provided that Reynolds number effects are neglected) [35]:

$$w'_s(v) = a'v^2 + b'v + c' = a\sqrt{\frac{m_0}{m}}v^2 + bv + c\sqrt{\frac{m}{m_0}} \quad (3.8)$$

where m_0 is the reference mass for the speed polar from Equation 3.7 and m is the actual mass of the vehicle.

3.2.2 Kinematic Models

The focus of this thesis is guidance, developing the desired vehicle states, rather than controlling the vehicle to those states. In general the slowest longitudinal mode of motion for an aircraft is the phugoid. The phugoid natural frequency can be approximated $\omega = \sqrt{2\frac{g}{V}}$ [72], for a small UAS this implies a period of 6-10 seconds. This gives a characteristic length scale for the aircraft motion of 100-200 meters. The next fastest longitudinal mode is the short period which is approximately a factor of 10 faster. Characteristic scales in the lower atmosphere range from 100-1000 meters, so the airspeed dynamics might be relevant, but faster motions of the aircraft should be decoupled from its response to the environment.

Reflecting this, simulations in this thesis use a kinematic aircraft model, depicted in Figure 3.5. To represent the airspeed change dynamics, airspeed commands are

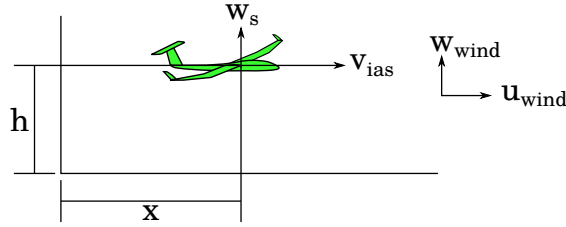


Figure 3.5: Aircraft kinematics used in simulations.

run through a first-order filter with a time constant of 5.0 seconds. The aircraft is restricted to maneuvering in the longitudinal plane, and the world is simplified to a flat earth. The states of interest are then: position, altitude, indicated airspeed, and stored specific energy. Inputs are speed command, power output from the onboard storage, horizontal and vertical winds, and solar power input. The state equations are given:

$$\frac{\partial}{\partial t} \begin{bmatrix} x \\ h \\ v_{ias} \\ e \end{bmatrix} = \begin{bmatrix} \frac{v_{ias}}{\sqrt{\sigma}} \\ \frac{w_s(v_{ias})}{\sqrt{\sigma}} \\ 0 \\ 0 \end{bmatrix} + \begin{bmatrix} 0 \\ \frac{\tilde{P}\eta_{propeller}}{mg} \\ \frac{v_{ias_command} - v_{ias}}{\tau} \\ \frac{-\tilde{P}}{mg} \end{bmatrix} + \begin{bmatrix} u_{wind} \\ w_{wind} + \frac{P_{pv}\eta_{propeller}}{mg} \\ 0 \\ 0 \end{bmatrix} \quad (3.9)$$

The first term represents the system dynamics where σ is the ratio of air density at the aircraft's location to sea level air density, and w_s is the sink rate. The second term is the aircraft response to control inputs, \tilde{P} is the power output from the onboard storage system, $\eta_{propeller}$ is the propeller efficiency, and τ is the airspeed control time constant. The final term is the response to environmental inputs, P_{pv} is the electrical power output from the solar array, u_{wind} the horizontal wind component, and w_{wind} the vertical wind component. The stored energy, e is defined such that its rate is negative when energy is drawn from storage. Rather than assuming an energy storage capacity, it is initialized to zero and its negative represents the amount of stored energy required to complete a flight.

3.2.3 Solar Power System

Since an aircraft equipped with solar cells was not available for flight tests, response to solar power is evaluated through simulation or in some cases using vertical air

velocity as a surrogate. In simulation a simplified solar power system model is used, the solar cell and power electronics are modeled with static power conversion efficiencies. The solar array efficiency used is 26%, the best reported installed efficiency [73]. Component and powertrain efficiencies are modeled after the work done by Edwards et al. [32]. The convention used here is that any solar-specific component efficiency is combined into an effective solar efficiency, η_{pv} , while efficiencies that occur regardless of the source of electrical power (e.g. motor and propeller) are included in the propeller efficiency. The component efficiencies are detailed in Table 3.1. The solar array is assumed to be integral with the wing upper surface, the fraction of the wing covered by the solar array is varied depending on the simulation.

Table 3.1: Solar power system and powertrain efficiencies.

component	efficiency	source
solar array	0.26	[73]
maximum power-point tracker	0.97	[32]
DC-DC converter	0.97	[32]
η_{pv}	0.24	
motor controller	0.95	[32]
motor	0.85	[32]
gearbox	0.97	[32]
propeller	0.85	[32]
$\eta_{propeller}$	0.67	

The nominal solar insolation is either specified as a static value or generated using the Python pvlib library [74]. When the exact geographic location of the aircraft is not important, the insolation is kept constant, at other times it is generated using pvlib. In all cases, the effect of aircraft maneuvering on the solar array incidence angle is neglected. Because the aircraft is in constant heading cruise flight the bank angle is approximately zero. In constant speed cruise flight pitch angles are small, typically less than $\pm 5^\circ$, so a small angle approximation is made and the solar array can be approximated as a plane parallel to the earth’s surface.

3.2.4 Stored Energy

There are a number of ways that an aircraft can store energy onboard. Batteries, engine-driven generators, and fuel cells can all provide supplemental power. A general purpose energy-saving autonomy algorithm should be agnostic to the method of storing energy on the aircraft. For this reason, the details of the energy storage are neglected in this thesis. Because energy storage density varies widely between the storage medium and because energy storage technology is constantly advancing the amount of energy available is not specified in this work. Instead, the aircraft is permitted to use whatever energy is required, and the amount of energy expended (and thus the amount which must be available) is examined. The only constraint placed on the energy storage mechanism is that it is not recharged, the aircraft stores excess energy in altitude, though this constraint can be relaxed by introducing appropriate efficiencies for storing and later using energy.

3.3 Environmental Models

Since the atmospheric environment is of primary concern in this research, models of some atmospheric phenomena are required. Clouds, horizontal winds, and updrafts all can have an effect on the aircraft's energy budget so all are implemented in the simulations used in this research. Depending on the simulation and its purpose the parameters for the models of these phenomena may be drawn from numerical weather prediction models or specified manually for illustrative purposes.

3.3.1 Clouds

When a discrete cloud is required, its shadow is modeled as a sharp-edged reduction in the solar input. Cloud shadows are assumed to lie directly underneath a cloud. Shadows can obviously be offset depending on the sun angle, but since the exact location of a shadow is not important, the simple direct projection is used. The effect of a cloud is defined by a "cloud factor," α , the fraction of incident solar energy which is transmitted through a cloud and is thus available beneath:

$$I_{cloud} = \alpha I_{clearsky} \quad (3.10)$$

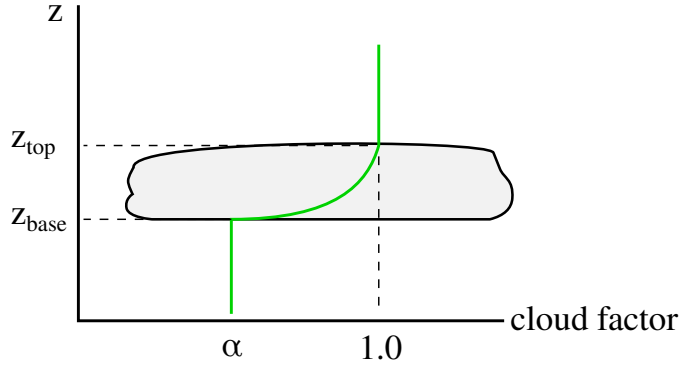


Figure 3.6: The effect of clouds is captured by the “cloud factor,” the fraction of light transmitted through a cloud. Every level within the cloud blocks the same fraction of light so the cloud factor decreases exponentially within the cloud.

The cloud is assumed to be homogeneous internally, so each unit depth of the cloud blocks the same fraction of light. This means that the cloud factor decreases exponentially within a cloud, depicted in Figure 3.6.

Generating cloud effects from a numerical weather model is slightly more complicated because weather model output files generally do not include incident solar radiation at every level. The surface solar insolation is available and a total cloud factor can be determined based on the nominal clear-sky solar insolation obtained from pvlib. The fraction of sky that is covered by cloud is generally available, assuming that the cloud fraction at each model level is statistically independent then the cumulative fraction of sky covered above a given altitude can be computed:

$$f_{tot}(z) = 1 - \prod_{i \text{ s.t. } z_i > z}^K (1 - f(z_i)) \quad (3.11)$$

Where $f(z)$ is the cloud coverage fraction. Since the actual locations of the clouds are not determined, and the optical thickness of clouds at different altitudes likely varies considerably, the logarithmic transmittance model is not used here. Instead, the cloud factor is a linear function of the cumulative solar fraction:

$$\alpha(z) = 1 - (1 - \alpha(z_{surface})) \frac{f_{tot}(z)}{f_{tot}(z_{surface})} \quad (3.12)$$

This model has some clear shortcomings, for instance once an overcast layer is encountered the cloud factor is the same at all lower levels regardless of whether

subsequent cloud layers exist (because the cloud fraction is saturated at 1.0), it also allows solar power to vary smoothly rather than jumping up and down as cloud shadows are encountered. It does however create a model where the amount of solar energy available is dependent on the vertical structure of the atmosphere and decreases in the presence of clouds.

3.3.2 Wind

In comparison to the solar model, the wind profile is relatively simple. Since the aircraft is restricted to the longitudinal plane of motion, the only wind component considered is the wind aligned along the direction of travel. A tailwind is defined as positive. Note that the assumption that the wind acts along the aircraft flight path is slightly different than the assumption that the aircraft flies in a single plane – flying in a crosswind requires a crab angle to correct a drift component which reduces the aircraft groundspeed. This effect is neglected here to simplify simulations.

When the weather model is not driven by numerical weather predictions, a constant wind is specified at all altitudes. When driven by a numerical weather model, the wind vector is retrieved from the model fields and projected onto the aircraft travel direction.

3.3.3 Updrafts

Thermals are the only type of updraft considered in this work, the distribution of vertical velocity within a thermal is modeled with the exponential function.

$$w_{wind} = \exp\left(-\frac{r}{r_{scale}}\right)w_{scale} \quad (3.13)$$

Where the r represents the distance between the aircraft and the thermal core, r_{scale} determines the thermal size, and w_{scale} the maximum strength. Rather than incorporating downdrafts surrounding the thermal core [75], the thermal strength is permitted to be negative, introducing areas of sinking air into the environment. This is simpler than the updraft distribution used by a number of other researchers [40, 75, 76]. Since the aircraft is not attempting to loiter within the thermals, the exact details of the thermal profile is less important. Using

exponential functions is simple and permitting “negative thermals” introduces areas of strong sink that are absent in past simulations of soaring flight.

3.3.4 Numerical Weather Prediction

For some simulations a dynamically consistent and time-evolving environment was desired. In these cases, output from the High Resolution Rapid Refresh HRRR model is used. This is a numerical weather prediction model with 3 kilometer resolution over the contiguous United States, it is run hourly with hourly output intervals over an 18 hour forecast [77]. The HRRR model provides surface solar insolation, turbulent kinetic energy, 3-D cloud fraction, and the 3-D wind vector.

3.4 Aircraft

Two small unmanned aircraft models are used in this work. The SB-XC is a large Group 1 to small Group 2 UAS, depending on its payload. The Vulture is a Group 1 UAS. While the two aircraft vary in size they have similar aerodynamic performance and a similar flight envelope, the inclusion of both in this work represents a transition in equipment available rather than an illustrative choice.

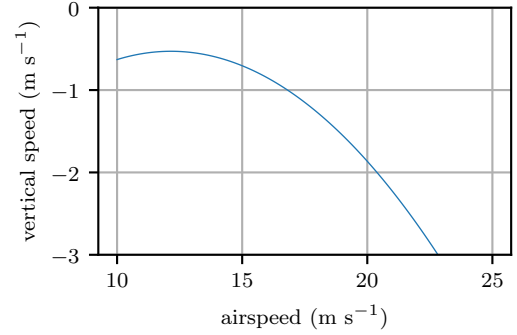
3.4.1 SB-XC

The SB-XC is a 4.2 m span aircraft used by a number of authors for autonomous soaring investigations [62–64,66]. It is generally flown at a mass of approximately 6.5 kg. The SB-XC aircraft is depicted in Figure 3.7a. While the aircraft is nominally a pure glider it can be modified with an electric motor offering an endurance of roughly one hour. The SB-XC has very good aerodynamic performance for an aircraft of its size, offering a best lift-to-drag ratio exceeding 20 [66]. The speed polar relating descent speed in a glider and airspeed is depicted in Figure 3.7b while its basic characteristics are given in Table 3.2.

As the SB-XC is a well characterized aircraft used by a number of authors and is a large enough aircraft to carry a mission payload it will be used for most of the simulations in this work.



(a) RnR products SB-XC sailplane modified with an electric motor.



(b) Speed polar for the SB-XC.

Figure 3.7: The SB-XC, a small UAS commonly used for soaring research.

Table 3.2: Basic parameters of the SB-XC aircraft.

mass	6.5 kg
S_{ref}	0.97 m ²
wingspan	4.2 m

3.4.2 Vulture

The Vulture (Figure 3.8) is a small UAS based on the G2 aviation Vera2V model sailplane. It is used in flight test experiments in this work as it is easier to transport, launch, and recover than the SB-XC. Basic parameters of the Vulture are given in Table 3.3. Since a speed polar based on flight data was not available for the Vulture, its performance was assumed to be similar to the SB-XC as they are of similar configuration.

Table 3.3: Basic parameters of the Vulture aircraft

mass	2.2 kg
S_{ref}	0.46 m ²
wingspan	2.5 m

Low-level control of the vehicle is provided by a pixhawk autopilot running a customized version of the PX4 flight stack [78]. The autopilot was modified to add a



Figure 3.8: The Vulture UAS.

flight mode permitting bank angle and airspeed to be commanded by a companion computer rather than the default attitude command mode. An onboard Odroid C1+ computer running Linux and the Robot Operating System generates bank angle and airspeed commands [79]. In addition to the sensors integral to the pixhawk a GPS, pitot-static probe with absolute and differential pressure sensors, and an outside air temperature probe are fitted. This permits the aircraft to determine its inertial and air-relative velocities, including the air density for computing true airspeed.

The wings each carry one 10 Ah single cell lithium ion battery. These batteries are connected in series are capable of powering the flight computer, autopilot, and servos for approximately 10 hours. A serial radio modem in the tailboom provides a datalink to provide information about the aircraft state, but all control and decision takes place on the vehicle.

Chapter 4 | Hybrid Solar Aircraft

Before developing guidance algorithms for solar augmented aircraft, it is worth exploring the design and operating space that these aircraft occupy and understanding how their capabilities compare to small UAS in general. “Solar aircraft” that cannot fly on solar power alone are hardly new: early piloted solar aircraft could not fly on solar energy alone [3]. These aircraft would soar in updrafts charging a battery using solar power, allowing periodic motor runs.

As technology improved the focus on solar aircraft shifted to high altitude pseudosatellites. Only recently has attention returned to solar augmentation, but now as a way to significantly improve the capability of small electric UAS [70, 73, 80, 81]. In principle, relaxing the requirement for pure and sustained solar flight could permit small UAS to achieve greater endurance, payload, and speed. This chapter will examine the impact that solar augmentation can have on the capability of small fixed-wing UAS.



Figure 4.1: The Silent Falcon is one of an emerging class of small solar augmented UAS. Reproduced from Silent Falcon (2019) “Silent Falcon” [81]

4.1 Solar Aircraft Performance

To understand the rationale for employing solar augmented rather than pure solar aircraft it is worth examining the performance and limitations of pure solar aircraft.

4.1.1 Maximum Speed in Pure Solar Flight

For many missions high cruise speed is desirable to increase flexibility or improve utilization of an air vehicle. Aircraft speed is relevant even for loitering missions – in high winds it may be necessary to fly relatively fast in order to remain in the desired area. The maximum speed a solar aircraft can sustain can be defined by equating the energy gained from the solar cells to that lost to aerodynamic drag. Recalling the solar power available from Equation 3.2 and equating this to specific power due to drag:

$$p_{pv,aero} = \frac{Dv}{mg} \quad (4.1)$$

Expanding both sides of Equation 4.1:

$$\frac{I \cos(i) S_{panel} \eta_{pv} \eta_{propeller}}{mg} = \frac{1}{2} \frac{\rho v^2 S_{ref} C_{Dv}}{mg} \quad (4.2)$$

Dividing by S_{ref} :

$$I \cos(i) \eta_{pv} \eta_{propeller} \frac{S_{pv}}{S_{ref}} = \frac{1}{2} \rho v^2 C_{Dv} \quad (4.3)$$

This can be thought of as balancing the power produced to that consumed per unit wing area. The fraction $\frac{S_{pv}}{S_{ref}}$ can be thought of the fraction of the wing covered in solar panels, though it is not strictly limited to the range $[0, 1]$. For instance if the horizontal tail were covered in panels it is possible that $S_{pv} > S_{ref}$. At first glance this makes the wing coverage fraction seem a little nonsensical, but in many ways it parallels the usage of the wing reference area, S_{ref} . Aircraft lift and drag coefficients nondimensionalized by S_{ref} include the contributions of components other than the wing's aerodynamic forces, but as the wing is the largest component of the aircraft these forces scale well with wing area. Similarly, the wing provides the greatest area for mounting solar panels so the available solar energy will scale with wing area.

If the fractional coverage is written $\beta_{pv} = \frac{S_{pv}}{S_{ref}}$ and equation 4.3 is rearranged, the maximum speed attainable by a solar aircraft in level flight can be determined.

$$v_{max} = \sqrt[3]{\frac{2I \cos(i) \beta_{pv} \eta_{pv} \eta_{propeller}}{\rho C_{D,min}}} \quad (4.4)$$

Equation 4.4 shows that achieving high speed on solar power requires very low drag and low air density (high altitude). This is a familiar approach to achieving high cruise speed, but the constraint of flying on solar power alone severely limits speed outside of this regime. For instance under ideal conditions with panels reaching the 86% efficiency limit derived by Araújo and Martí [82] covering the entire wing surface, a fully illuminated sky with normal solar incidence, a perfectly efficient propeller, and a minimum drag coefficient of 0.005 (approximately the best achieved by modern sailplane *airfoils* [83]) the maximum achievable speed at sea level is 66 m s⁻¹. This is quite fast for a small UAS but is slower than many light aircraft. Reducing the solar cell efficiency to 26% [73] and using typical powertrain efficiencies [32] limits the maximum speed at sea level to 37 m s⁻¹.

An operational aircraft would have higher drag as it also has induced and trim drag as well as drag caused by sensors, communication antennas, and mission equipment. For small UAS operating at low altitude a drag coefficient of 0.02 (roughly the minimum drag coefficient of the SB-XC) is probably a realistic minimum. Assuming a propeller efficiency of 85% [32] then the maximum achievable speed is 24 m s⁻¹. This is above the nominal cruise speed of the SB-XC, so under ideal conditions solar flight is within the operating envelope of an efficient small UAS.

4.1.2 Maximum Wing Loading in Pure Solar Flight

Another way to consider the performance limitations of solar aircraft in cruise is to consider how heavy a solar aircraft can be and sustain flight. This is obviously relevant from the perspective of maximizing the amount of payload that can be carried. Xiong et al. derive a limit on the maximum wing loading that can be sustained by a solar aircraft [84]:

$$\frac{W}{S} = (P_{pv} \eta_{pv} \eta_{propeller})^{\frac{2}{3}} \left(\frac{\rho}{2}\right)^{\frac{1}{3}} \left(\frac{C_L^{1.5}}{CD}\right)^{\frac{2}{3}} \quad (4.5)$$

By writing $\left(\frac{C_L^{1.5}}{C_D}\right)^{\frac{2}{3}}$ as $\left(\frac{C_L}{C_D}\right)^{\frac{2}{3}} C_L^{\frac{1}{3}}$ and then expanding the lift coefficient normally and P_{pv} according to Equation 3.2 then Equation 4.5 can be written in a form more compatible with the analysis in Section 3.2.1:

$$\frac{m}{S_{ref}} = \frac{1}{g} S_{pv} \alpha I \cos i \eta_{pv} \eta_{propeller} \frac{L}{D} \frac{1}{v} = \frac{1}{g} S_{pv} \alpha I \cos i \eta_{pv} \eta_{propeller} \frac{-1}{w_s(v)} \quad (4.6)$$

Since sink rate is itself a function of wing loading, Equation 4.6 is an implicit equation for the maximum wing loading at which level flight can be achieved on solar power alone. Assuming that the solar and propeller efficiencies are independent of speed, then the greatest wing loading occurs when sink rate is least (the minimum power flight condition), so when iterating to solve this equation only the minimum sink rate condition need be checked.

For the SB-XC with wings fully covered in solar panels, perfect solar conditions, and the theoretical maximum solar efficiency of 86%, this yields a wing loading of 42.2 kg m⁻², lower than the wing loading at *empty weight* for the Cessna 172 or General Atomics MQ-1. With the current state of the art installed solar cell efficiency of 26% [73], and typical power train efficiencies [32], this wing loading drops to 19.0 kg m⁻², well below light general aviation and mid-size tactical UAS wing loadings. At a latitude of 40.8° (central Pennsylvania) the solar insolation, I , is about 80% of its value at the equator and the permissible wing loading drops even further to 15.8 kg m⁻².

A wing loading below 15 kg m⁻² is not unreasonable for small UAS – the nominal wing loading of the SB-XC is below 7 kg m⁻². This shows that aerodynamically efficient small UAS can be made capable of sustained solar flight, a fact that is also reflected in the number of authors that have explored designs for this class of aircraft [80, 85, 86].

4.2 Solar Augmented Performance

Section 4.1 showed that many small fixed-wing UAS are capable of flying purely under solar power in ideal solar conditions and at slow speeds. If enough additional energy can be carried to power the aircraft in off-nominal solar times (such as morning, evening, or when traversing a cloudy region) or when making a high speed

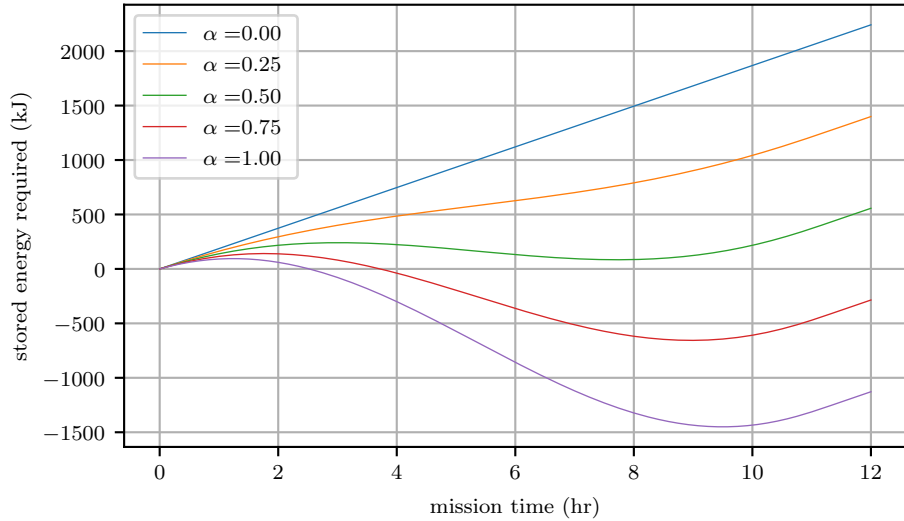


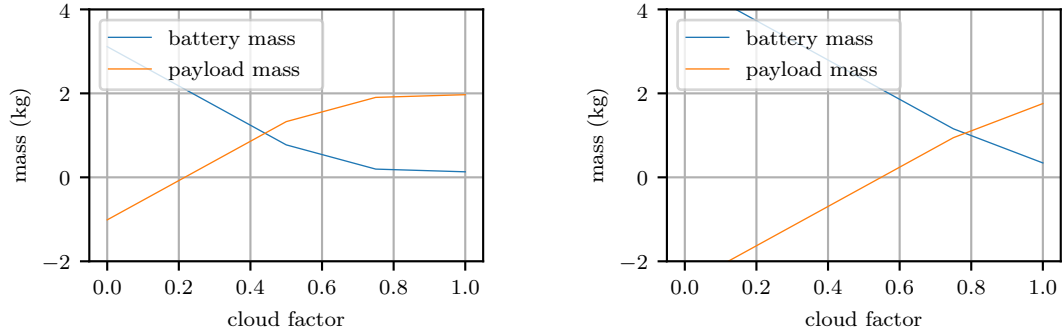
Figure 4.2: Battery energy required for a 12 hour mission on the equinox for an SB-XC cruising at its speed for best range.

dash, then it should be possible to achieve all-day endurance for small UAS using current solar technology, motivating the concept of a solar augmented aircraft.

The capabilities of solar augmentation can be demonstrated by considering a notional solar augmented UAS with aerodynamic and mass properties similar to the SB-XC. Based on a rough survey of the mass of hand- and bungee-launched UAS, the maximum practical weight of a small UAS which does not require sophisticated launch and recovery infrastructure is about 8 kg. The basic airframe weight of the SB-XC is 5.5 kg without batteries, assuming that 80% of the wings can be covered in solar cells and that solar cells have an areal density of 0.59 kg m^{-2} [9] the aircraft’s useful load is 2.1 kg.

Assuming the payload and aircraft systems require 10 W of power each (the avionics power reflects that reported by Depenbusch et al. [66]), the energy budget can be evaluated for a candidate mission by integrating the excess power and computing the mass of batteries required. For a baseline mission, consider a 12 hour (sunrise to sunset) mission in Centre County, Pennsylvania on 20 March 2019 (the vernal equinox) with the aircraft flying its best range speed at all times. Figure 4.2 illustrates the state of a rechargeable battery throughout this mission for several different “cloud factors.”

When the cloud factor is greater than 0.5 (more than half of the incident sunlight



(a) Payload capacity and battery mass required to fly at best cruise speed, 14.5 m s^{-1} .

(b) Payload capacity and battery mass required to fly 17 m s^{-1} .

Figure 4.3: Battery mass required and capacity for solar augmented SB-XC flying a 12 hour mission on the equinox.

reaches the aircraft), then a 12 hour flight can be accomplished with only a nominal battery capacity required.

4.2.1 Performance Sensitivity to Atmospheric Conditions

Assuming a pack-level battery energy density of 200 W hr kg^{-1} , the mass of the battery required and the payload which can be accommodated by the SB-XC as a function of the cloud factor is shown in Figure 4.3a. Note that when no solar power is available ($\alpha = 0$) that the payload mass is negative, indicating that the aircraft cannot reach 12 hours of endurance even if all of the useful load is dedicated to batteries. In general however, the payload capacity is relatively resilient to reductions in solar power and as long as some solar energy is available it is possible to achieve very long endurance when flying the best cruise speed.

Figure 4.3b shows the payload capacity for the 12 hour mission when it is flown at an airspeed of 17 m s^{-1} . The payload capacity is significantly reduced for all solar conditions, and the mission cannot even be completed with no payload unless more than half of the clear sky solar insolation is available. Comparing Figures 4.3a and 4.3b shows that a small increase in speed has a greater impact on the aircraft payload carrying capacity than reducing the solar insolation by half.

The reason for this sensitivity is shown in Figure 4.4 which compares speed polars for the basic and solar augmented SB-XC. Solar augmentation shifts the

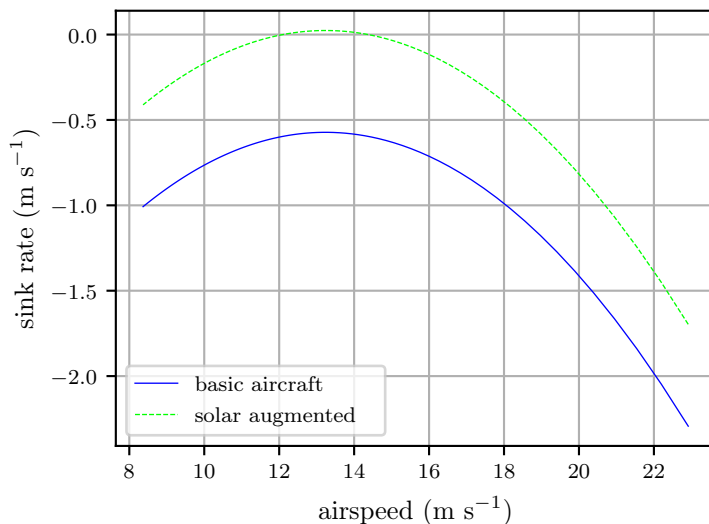


Figure 4.4: Basic and solar augmented polars for the SB-XC at a mass of 8 kg flying at noon in Pennsylvania with a cloud factor of 0.75. Solar augmentation moves the polar up, reducing energy input but does not affect the shape of the polar so high speed is still quite costly.

polar up, reducing the cost of flight at all conditions. It does not change the shape of the polar however, so flight at high speeds is still very costly. In this case the aircraft can maintain flight under pure solar power at up to 14 m s⁻¹ but by 19 m s⁻¹ the solar augmented aircraft requires more power than the minimum power without augmentation.

The speed difference between Figures 4.3a and 4.3b is approximately equal to the analysis skill (difference between the true atmospheric state and posterior state expected by a weather model after incorporating observations) for numerical weather prediction in the contiguous United States [87, 88], so a 2.5 m s⁻¹ speed perturbation would not be uncommon when the aircraft is tracking a flight planned *a priori* using a weather forecast if the time of arrival is specified.

Solar augmentation can significantly enhance the range and endurance of a small UAS, but it does not change the sensitivity of the aircraft to environmental conditions. In order to operate effectively over long ranges, both solar augmented and conventionally powered small UAS therefore need awareness of their environment.

4.3 Summary

The energy budget of small solar augmented UAS is sensitive to small changes in speed but fairly robust to variations in solar insolation. If operating under the guidance of an *a priori* plan then relatively small errors between the expected and true wind can significantly impact the payload and range capability of the aircraft, especially if an arrival time is specified. This sensitivity makes using small UAS for missions over long ranges difficult and is likely responsible for the fact that there are few small UAS – solar augmented or otherwise – employed in missions requiring more than a few kilometers of range or an hour of endurance.

To be robust to these sensitivities a small UAS that is useful for long-range missions should have significant endurance (to provide some “padding” in the energy budget). It should also have a system capable of identifying departures from the anticipated conditions and responding in a way which minimizes the impact of these perturbations on the aircraft’s energy budget. These objectives are familiar – extending endurance is the motivation for solar augmentation and the other objectives are the design goals for this work that were identified in Section 1.2

Chapter 5 | Speed to Fly

Many planners for solar aircraft assume that variations in energy input are driven entirely by celestial mechanics and the aircraft attitude [31,32,89]. For low altitude solar aircraft the situation is more complex. The exact location of clouds in the lower atmosphere cannot be perfectly forecast, so the shadows these clouds cast will cause stochastic variations in energy input. Vertical air motion in the convective boundary layer also cannot be forecast with enough precision to enable *a priori* planning, so it provides another (potentially negative) stochastic energy input.

Further complicating the problem, updrafts and clouds shadows might be correlated as clouds frequently form at the top of updrafts. Near solar noon when cloud shadows are located directly underneath the clouds, the aircraft may simultaneously experience a decrease in solar energy and an updraft. At other times, cloud shadows are offset so that the correlation could be absent or even reversed. To minimize energy expended from onboard storage, a method is needed that can simultaneously manage the interruptions in solar power and variations in updraft intensity.

For guidance in the vertical plane, the aircraft's control action is limited to speed and power output. Any solar power available should be used to its full extent, so "power output" as a control means non-renewed output from an onboard store of energy such as a battery.

5.1 Speed to Fly with Stochastic Energy Input

We will begin by deriving a speed control which minimizes energy consumption. A speed control is particularly useful as it is equally applicable to solar augmented aircraft and pure solar aircraft which cannot use "power output" as they must

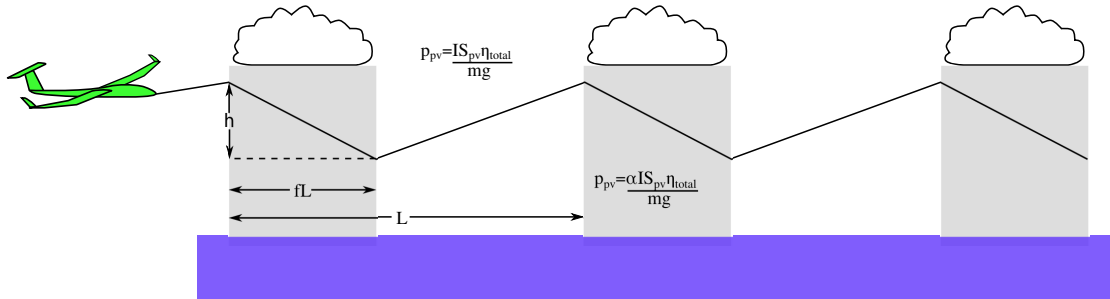


Figure 5.1: Definition of the solar speed to fly problem, the aircraft traverses cloud shadows over a fraction, f , of its flight path.

satisfy their entire energy budget with solar power.

5.1.1 Pure Solar Flight with Interruptions

Sailplanes must collect energy in concentrated areas of upward moving air, then traverse regions of sinking air before reaching the next energy source. This is similar to the challenge faced by a solar aircraft flying at low altitude. The aircraft gains energy flying in sunny regions and then must traverse a shadowed area where there is less energy available. It is desirable to find the optimal strategy for a solar powered aircraft to adopt when traversing areas of varying solar energy. This strategy is known in the soaring literature as “speed to fly” [35].

Continuing the analogy with soaring flight, a development similar to classic soaring speed to fly theory is used here [35, 70]. A two-segment flight is considered: the aircraft flies underneath a cloud, losing altitude which must be regained during a subsequent climb in sun. This situation is depicted in Figure 5.1. It is analogous to a sailplane traversing an area of sinking air. In this situation, a soaring aircraft should speed up to minimize the time spent in the sinking air. It is expected then, that the optimal strategy here will be to speed up when traversing cloud shadows, then slow down to “recharge” by climbing in sun.

The cloud cover is assumed to be uniformly shaped and scattered and vertical air motion is neglected for the moment. Cloud cover is defined by the fraction spent in shadow while flying a leg of length L . The aircraft loses altitude h while traversing the shadowed region and regains that altitude in a cruise-climb while in a sunny segment so that there is no change in total energy over a cloud-sun cycle. Shadowed regions are assumed to be brief enough with sufficient length of sunny

regions in between to enable the altitude to be regained. The solar incidence angle is assumed to be constant. First, the time spent in each flight segment is computed:

$$t_{cloud} = f \frac{L}{v_{cloud}} \quad (5.1)$$

$$t_{sun} = (1 - f) \frac{L}{v_{sun}} \quad (5.2)$$

The mean cross-country speed is then:

$$\bar{v} = \frac{\Delta X}{\Delta t} = \frac{L}{t_{cloud} + t_{sun}} = \frac{L}{f \frac{L}{v_{cloud}} + (1 - f) \frac{L}{v_{sun}}} = \frac{v_{cloud} v_{sun}}{f v_{sun} + (1 - f) v_{cloud}} \quad (5.3)$$

The altitude gained and lost when traversing sunny and cloudy areas can be expressed as h_{sun} and h_{cloud} respectively:

$$h_{sun} = (w_s(v_{sun}) + p_{sun}) t_{sun} = (w_s(v_{sun}) + p_{sun}) (1 - f) \frac{L}{v_{sun}} \quad (5.4)$$

$$h_{cloud} = (w_s(v_{cloud}) + p_{cloud}) t_{cloud} = (w_s(v_{cloud}) + p_{cloud}) f \frac{L}{v_{cloud}} \quad (5.5)$$

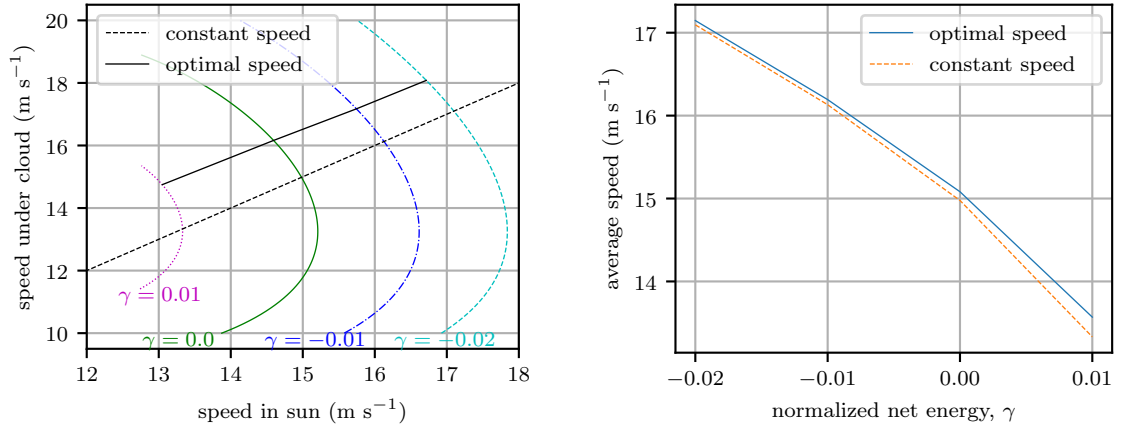
Where p_{cloud} and p_{sun} represent the specific solar power output in shadow and sun respectively. Since the altitude lost under clouds must be regained in the sunny segments, $h_{cloud} = -h_{sun}$. Substitution of the expressions from Equation 5.5 and Equation 5.4 yields:

$$(w_s(v_{cloud}) + p_{cloud}) f \frac{L}{v_{cloud}} = - (w_s(v_{sun}) + p_{sun}) (1 - f) \frac{L}{v_{sun}} \quad (5.6)$$

simplifying,

$$(w_s(v_{cloud}) + p_{cloud}) f \frac{v_{sun}}{v_{cloud}} + (w_s(v_{sun}) + p_{sun}) (1 - f) = 0 \quad (5.7)$$

gives an implicit equation for the relationship between the speed under cloud and the speed in sun. The method of Lagrange multipliers could be used to maximize Equation 5.3 subject to Equation 5.7, but the analytic form is complex. Thus, to explore this relation, Equation 5.7 is solved for a range of speeds when traversing



(a) Contours depict speed schedules which will achieved a desired net energy. The optimal and constant speed schedules are shown connecting contours.

(b) Best average speed achieved as a function of net energy after a sun / cloud cycle.

Figure 5.2: Solar powered cross-country performance for a small UAS.

clouded regions and the corresponding mean speed is then computed. Figure 5.2 details the relationship between cloud and sun speeds and the average cross-country speed. The solution is illustrated for the SB-XC aircraft described Section 3.4.1, assuming that 80% of its wing is covered in solar panels (so that it can sustain flight on solar power). Clouds are assumed to cover one third of the sky and fully block incident solar energy with a clear sky insolation of 750 W m^{-2} .

Figure 5.2a illustrates the relationship between speed under cloud and in sun required in order to meet a specified net energy after one cycle, with net specific energy expressed as a fraction of the cycle length. Figure 5.2b illustrates the average speed achieved as a function of the net energy. Expressed this way, the net energy is equivalent to the flight path angle, γ . The speed relationships are smooth throughout the flight envelope of the aircraft, suggesting that numerical solutions optimizing Equation 5.3 will be reliable and fast to compute.

The dashed black line in Figure 5.2a indicates the constant speed schedule to achieve a desired net energy. Figure 5.2b shows that constant speed flight is suboptimal. The optimal strategy is to speed up slightly under clouds to rapidly leave the shadow, then slow down in sunny regions to gain altitude. The

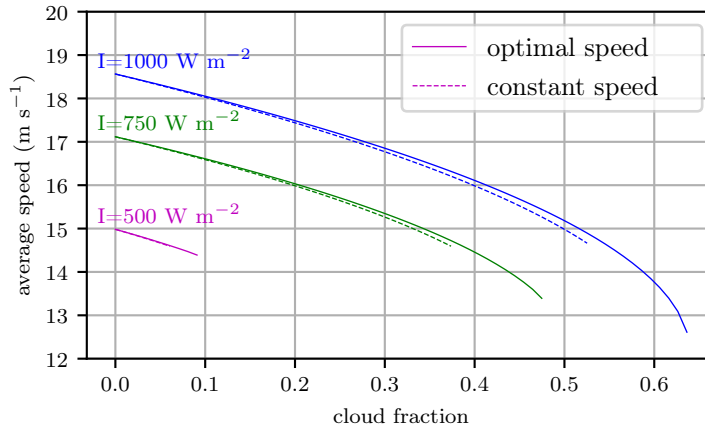


Figure 5.3: Average speed as a function of cloud factor for several solar insolation values with not net energy.

improvement in cross-country speed is small, about 1%.

Figure 5.3 shows the mean speed achieved using speed to fly and constant speed schedules as a function of solar insolation and cloud fraction for $\gamma = 0$. The speed curves end at a cloud fraction where sustained flight is not possible on solar power alone. As cloud fraction increases, the advantage of flying speed to fly increases although the speed gain is still quite small. The most significant impact of adopting speed to fly is that the aircraft is capable of sustaining flight with significantly larger cloud fractions.

While this development uses altitude lost and gained to express the aircraft total energy, the development holds for any storage medium. If excess solar power is stored in a battery instead of altitude, the same result holds, provided the aircraft achieves a “net energy” equal to the energy conversion loss in charging and discharging the battery.

5.1.2 Joint Optimization of Solar and Updraft Energy

The magnitude of specific solar power is approximately 1 m s^{-1} , similar to the magnitude of vertical air motion in a convective boundary layer [10]. Solar energy and vertical air motion may also be correlated depending on the atmospheric conditions and time of day, making it desirable to have a speed command which considers both sources of energy. This problem is illustrated in Figure 5.4: the

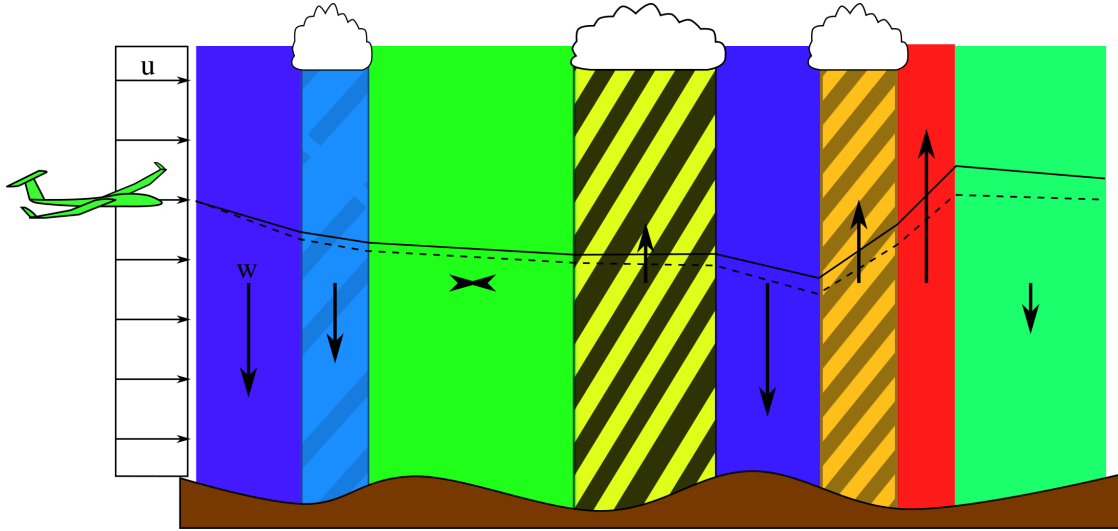


Figure 5.4: Problem definition for simultaneous optimization of updraft and solar energy. A series of segments are defined with stochastic input from solar energy and vertical air motion on each segment. A constant horizontal wind acts on the aircraft throughout the flight. Vertical air motion is indicated by color and arrows, cloud influence by shading. The aircraft is permitted to change airspeed when transitioning to a new segment.

aircraft transits regions with varying vertical air motion and solar input. The aircraft also experiences a constant horizontal wind.

Assuming that the aircraft is equipped with onboard energy storage, the requirement from Section 5.1.1 that all required energy is harvested from the environment can be relaxed. This allows the optimal speed to be determined even for cases where the aircraft cannot sustain flight on solar power alone in full sun, which causes nonsensical solutions to Equation 5.7 because the condition that the altitude lost in shadow be regained in sun cannot be satisfied.

The equivalence of specific solar power and vertical motion established in Section 3.2.1 permits the combining solar and updraft energy into a single value measuring the power being harvested from the environment.

$$p_h = p_{pv,aero} + w_{wind} \quad (5.8)$$

The distinction from Section 5.1.1 between energy gaining and energy losing segments is eliminated by allowing p_h to take on negative values. The control variables are speed and power output from storage, v and p_{out} respectively. The

flight is approximated as a series of segments of random length with constant energy harvest rate in each segment, similar to the approach adopted by Arho [37], but with generalized energy harvest rate. The aircraft is permitted to change the velocity and power output at the beginning of each segment. It is assumed that segments are long enough that the transient behavior when changing controls is negligible. Each variable can then be written:

$$p_h(x) = \sum_n \hat{p}_n \text{RECT}(x_n, \Delta x_n, x) \quad (5.9)$$

$$v(x) = \sum_n \tilde{v}_n \text{RECT}(x_n, \Delta x_n, x) \quad (5.10)$$

$$p_{output,aero}(x) = p_{output}(x) \eta_{propeller} = \sum_n \tilde{p}_n \text{RECT}(x_n, \Delta x_n, x) \quad (5.11)$$

Where \hat{p}_n represents the energy harvested, \tilde{v}_n the speed command, and \tilde{p}_n the aerodynamic power output from storage in segment n . Segments are defined by a start x_n , interval Δx_n , and the rectangular function $\text{RECT}(x_n, \Delta x_n, x)$:

$$\text{RECT}(x_n, \Delta x_n, x) = \begin{cases} 1, & x \in [x_n, x_n + \Delta x] \\ 0, & \text{otherwise} \end{cases} \quad (5.12)$$

Assuming that the propulsion efficiency is static, then the energy output from storage can be minimized by minimizing the integrated aerodynamic power output from storage, $e_{output,aero}$ which can be computed:

$$\begin{aligned} e_{output,aero} &= \int_T p_{output,aero}(t) dt \\ &= \int_X p_{output,aero}(x) \frac{dt}{dx} dx \\ &= \sum_n \int_{x_n}^{x_n + \Delta x_n} \frac{\tilde{p}_n}{\tilde{v}_n + u} \text{RECT}(x_n, \Delta x_n, x) dx \\ &= \sum_n \frac{\tilde{p}_n}{\tilde{v}_n + u} \Delta x_n \\ &= \sum_n \tilde{p}_n \frac{l_n}{\tilde{v}_n + u} \end{aligned} \quad (5.13)$$

Where l_n is the length of segment n and u is the constant horizontal wind,

positive for a tailwind. The aircraft energy state after crossing a sequence of N segments with known energy harvest rates and length is a function of $2N$ variables, $\{\tilde{p}_n, \tilde{v}_n\}$.

Achieving minimum expenditure of stored energy is thus an optimization problem to minimize Equation 5.13 while remaining above ground and starting and ending at the same altitude.

The constraint requiring that the initial and final altitudes be equal prevents the aircraft from minimizing energy expenditure by descending to arbitrarily low altitudes. It can be written:

$$\begin{aligned}
0 &= e(T) - e(0) \\
&= \int_T (p_h(t) + p_{out}(t) + w_s(v(t))) dt \\
&= \int_X (p_h(x) + p_{out}(x) + w_s(v(x))) \frac{dt}{dx} dx \\
&= \sum_n \int_{x_n}^{x_n + \Delta x_n} \frac{\hat{p}_n + \tilde{p}_n + w_s(\tilde{v}_n)}{\tilde{v}_n + u} \text{RECT}(x_n, \Delta x_n, x) dx \\
&= \sum_n (\hat{p}_n + \tilde{p}_n + w_s(\tilde{v}_n)) \frac{l_n}{\tilde{v}_n + u}
\end{aligned} \tag{5.14}$$

For the moment, the final condition that the aircraft remain above ground at all times is neglected. The rationale for this will later be evident.

Since the energy constraint can be expressed as an equality, this optimization problem can be solved through Lagrange multipliers. The Lagrangian can be written:

$$\mathcal{L} = \sum_n \tilde{p}_n \frac{l_n}{\tilde{v}_n + u} + \lambda_1 \left(\sum_n (\hat{p}_n + \tilde{p}_n + w_s(\tilde{v}_n)) \frac{l_n}{\tilde{v}_n + u} \right) \tag{5.15}$$

Computing partial derivatives:

$$\frac{\partial \mathcal{L}}{\partial \tilde{v}_i} = \frac{l_i}{(\tilde{v}_i + u)^2} \left(-\tilde{p}_i - \lambda_1 \left(\hat{p}_i + \tilde{p}_i + w_s(\tilde{v}_i) - \frac{\partial w_s(\tilde{v}_i)}{\partial \tilde{v}_i} (\tilde{v}_i + u) \right) \right) = 0 \tag{5.16}$$

$$\frac{\partial \mathcal{L}}{\partial \tilde{p}_i} = \frac{l_i}{\tilde{v}_i + u} (1 + \lambda_1) = 0 \tag{5.17}$$

$$\frac{\partial \mathcal{L}}{\partial \lambda_1} = \sum_n (\hat{p}_n + \tilde{p}_n + w_s(\tilde{v}_n)) \frac{l_n}{\tilde{v}_n + u} = 0 \quad (5.18)$$

From Equation 5.17 it is clear that $\lambda_1 = -1$. Substituted into Equation 5.16, this causes \tilde{p}_i to drop out of the equation entirely. Thus Equations 5.16 and 5.18 are decoupled. This simplifies the optimization to N equations for $\{\tilde{v}_i\}$ and a single equation constraining $\{\tilde{p}_i\}$. Any choice of $\{\tilde{p}_i\}$ in the null space of Equation 5.18 is valid. This justifies relaxing the criteria that the aircraft stays above ground, as the power output can be specified to do so without altering the optimal speed. The resulting equations for $\{\tilde{v}_i\}$ reduce to the requirement that each segment i satisfy:

$$\hat{p}_i + w_s(\tilde{v}_i) - \frac{\partial w_s(\tilde{v}_i)}{\partial \tilde{v}_i} (\tilde{v}_i + u) = 0 \quad (5.19)$$

This is the classic speed to fly equation [35] with the MacCready value, MC , set to zero. Equation Equation 5.19 can be further simplified if the speed polar is represented by a second-order polynomial:

$$\tilde{v}_i = \sqrt{\frac{au^2 - bu + \hat{p}_i + c}{a}} - u \quad (5.20)$$

Note that the optimal speed command is dependent only on the instantaneous value of \hat{p}_i so the unified power harvesting value is sufficient to determine the optimal speed, avoiding complications arising from correlation between solar power and updrafts.

5.1.3 Speed to Fly for Schedule Keeping

In many applications a waypoint may be specified by an operator or outer loop planner with a desired time of arrival. Even with schedule keeping requirements, it is desirable to minimize energy consumption. Section 5.1.2 shows that the speed and power schedule can be solved separately. It does not however, provide a means to control the average speed. The optimization framework presented in Section 5.1.2 can be extended to incorporate the arrival time constraint.

5.1.3.1 Energy Optimization With Speed Constraint

If the desired time of arrival after N segments is T , this can be expressed as an average speed requirement:

$$\begin{aligned}\bar{v} &= \frac{X}{T} \\ &= \frac{\sum_n l_n}{\sum_n \frac{l_n}{\tilde{v}_n + u}}\end{aligned}\tag{5.21}$$

The arrival time constraint can be incorporated into the optimization problem, Equation 5.15, by augmenting the Lagrangian with another term:

$$\mathcal{L} = \sum_n \tilde{p}_n \frac{l_n}{\tilde{v}_n + u} + \lambda_1 \left(\sum_n (\hat{p}_n + \tilde{p}_n + w_s(\tilde{v}_n)) \frac{l_n}{\tilde{v}_n + u} \right) + \lambda_2 \left(\frac{\sum_n l_n}{\sum_n \frac{l_n}{\tilde{v}_n + u}} - \bar{v} \right)\tag{5.22}$$

Which introduces one more term into the partial derivative with respect to \tilde{v}_i :

$$\begin{aligned}\frac{\partial \mathcal{L}}{\partial \tilde{v}_i} &= 0 \\ &= \frac{l_i}{(\tilde{v}_i + u)^2} \left(-\tilde{p}_i - \lambda_1 \left(\tilde{p}_i + \hat{p}_i + w_s(\tilde{v}_i) - \frac{\partial w_s(\tilde{v}_i)}{\partial \tilde{v}_i} (\tilde{v}_i + u) \right) - \lambda_2 \frac{\sum_k l_k}{\left(\sum_k \frac{l_k}{\tilde{v}_k + u} \right)^2} \right)\end{aligned}\tag{5.23}$$

and adds one more equation to solve after taking partial derivatives:

$$\frac{\partial \mathcal{L}}{\partial \lambda_2} = \frac{\sum_n l_n}{\sum_n \frac{l_n}{\tilde{v}_n + u}} - \bar{v} = 0\tag{5.24}$$

The partial with respect to λ_1 is unchanged so again, $\lambda_1 = -1$ and the speed and power optimizations are decoupled. Equation 5.23 simplifies to a form similar (but not identical) to the speed to fly equation:

$$0 = \hat{p}_i + w_s(\tilde{v}_i) - \frac{\partial w_s(\tilde{v}_i)}{\partial \tilde{v}_i} (\tilde{v}_i + u) - \lambda_2 \frac{\sum_k l_k}{\left(\sum_k \frac{l_k}{\tilde{v}_k + u} \right)^2}\tag{5.25}$$

Note that in Equation 5.25 the term involving λ_2 is not dependent on any

individual \tilde{v}_i . Hence that term can be written as $MC = \lambda'_2 = \lambda_2 \frac{\sum_k l_k}{\left(\sum_k \frac{l_k}{\tilde{v}_k + u}\right)^2}$, the MacCready value which will optimize energy consumption while respecting the speed constraint.

Equation 5.25 can also be simplified if the aircraft performance is assumed to follow a quadratic polar:

$$\tilde{v}_i = \sqrt{\frac{au^2 - bu + c + \hat{p}_i - MC}{a}} - u \quad (5.26)$$

5.1.3.2 Speed to Fly Inversion

Equation 5.25 specifies a family of speed schedules which minimize energy use, but it does not provide a means to compute $MC = \lambda'_2$, which identifies the schedule that satisfies the arrival time condition. If the input power distribution \hat{p}_n is known then MC can be computed directly. Since \hat{p} is a stochastic function, it will not be known *a priori* so another means to determine MC is required.

One approach is to invert the speed to fly problem. MC can be approximated by solving Equation 5.25 in the mean sense:

$$0 = \mathbb{E}(\hat{p}_i) + \mathbb{E}(w_s(\tilde{v}_i)) - \mathbb{E}\left(\frac{\partial w_s(\tilde{v}_i)}{\partial \tilde{v}_i}(\tilde{v}_i + u)\right) - MC \quad (5.27)$$

The arrival time constraint specifies the expected speed, \bar{v} . Over the operating envelope of the aircraft, the speed polar is approximately linear in a neighborhood of any speed so that:

$$\mathbb{E}(w_s(v)) \approx w_s(\bar{v}) \quad (5.28)$$

and

$$\mathbb{E}\left(\frac{\partial w_s(\tilde{v}_i)}{\partial \tilde{v}_i}(\tilde{v}_i + u)\right) \approx \frac{\partial w_s(\bar{v})}{\partial v}(\bar{v} + u) \quad (5.29)$$

Equation 5.27 can then be solved for an approximate MC value provided that $\mathbb{E}(\hat{p}_i)$ can be estimated:

$$MC \approx \mathbb{E}(\hat{p}_i) + w_s(\bar{v}) - \frac{\partial w_s(\bar{v})}{\partial v}(\bar{v} + u) \quad (5.30)$$

If the aircraft speed polar, $w_s(v)$ is assumed to be quadratic then the MacCready

value can be written:

$$MC \approx \mathbb{E}(\hat{p}_i) - a\bar{v}^2 + c - 2a\bar{v}u - bu \quad (5.31)$$

This is useful as it is reasonable to expect that $\mathbb{E}(\hat{p}_i)$ could be estimated (for instance by a weather forecast of cloud cover, or by a running average assuming that conditions change slowly). The error introduced by this approximation will be explored numerically in Section 5.2.1.

It is worth noting here that $\mathbb{E}(\hat{p}_i)$ is a weak function of \bar{v} . Speed to fly works on the principle that speed variations allow the aircraft to spend more time in favorable regions and less time in unfavorable regions, effectively modifying the environment experienced by the aircraft. When the average speed is low, the aircraft will slow more when harvesting energy and speed up more when losing energy than when it must achieve a higher speed so it will achieve a larger effective value for $\mathbb{E}(\hat{p}_i)$. This effect is relatively small and is only relevant when $\mathbb{E}(\hat{p}_i)$ is computed from a spatial average of \hat{p}_i , for example from a weather forecast. If $\mathbb{E}(\hat{p}_i)$ is estimated from a time average of \hat{p} measured on the aircraft then this variation vanishes provided the nominal speed remains the same.

5.1.3.3 Convergence Analysis

Consider a simplified form of the speed scheduling problem where there is no stochastic variation in the environment. At each timestep, the MC value is determined based on the mean speed required to satisfy the arrival time and a speed command generated. The vehicle is modeled as purely kinematic on the basis that the flight time is much larger than the aircraft longitudinal dynamics, $t_{final} \gg T_{longitudinal}$. This system can be written:

$$x_{k+1} = x_k + \Delta t v_{command} \quad (5.32)$$

The speed command, $v_{command}$ is generated so that the aircraft flies the distance remaining to the goal point in the allotted time remaining. For simplicity in analysis the final point will be assumed to be $x = 0$. The controller can then be written into the system dynamics as:

$$\begin{aligned}
x_{k+1} &= x_k + \Delta t \frac{-x_k}{t_{final} - k\Delta t} \\
&= x_k \left(1 - \frac{\Delta t}{t_{final} - k\Delta t} \right)
\end{aligned} \tag{5.33}$$

There is a clear concern that as the aircraft reaches the final time and $k\Delta t = t_{final}$ that there is a singularity in the solution. In UAS navigation it is common to have a threshold distance around a waypoint which satisfies reaching the point, so the singularity itself might not be critical, provided that the controller is bounded sufficiently close to the goal point.

Because this system is time varying, its convergence cannot be analyzed through the system equation. Instead convergence of this system can be established through the state transition matrix [90]:

$$x_{k+1} = \Phi(k+1, 0)x_0 \tag{5.34}$$

For notational brevity the state transition matrix that maps x_0 to x_{k+1} will be written as Φ_{k+1} , retaining the function notation when the initial state is not x_0 . By recursive application of the system matrix $x_{k+1} = A(k)x_k$ the general form for the state transition matrix can be determined.

$$\begin{aligned}
x_{k+1} &= A(k)x_k = A(k)A(k-1)x_{k-1} = A(k)\dots A(0)x_0 \\
&= \left(\prod_{i=0}^k A(i) \right) x_0 \\
&= \left(\prod_{i=0}^k \left(1 - \frac{\Delta t}{t_{final} - i\Delta t} \right) \right) x_0
\end{aligned} \tag{5.35}$$

So that the state transition matrix is:

$$\Phi_{k+1} = \prod_{i=0}^k A(i) = \prod_{i=0}^k \left(1 - \frac{\Delta t}{t_{final} - i\Delta t} \right) \tag{5.36}$$

At first glance this does not appear to be an improvement as there is still a singularity when $k = \frac{t_{final}}{\Delta t}$. However, at step $k = \frac{t_{final}}{\Delta t} - 1$ the system matrix goes to:

$$\begin{aligned}
A\left(\frac{t_{final}}{\Delta t} - 1\right) &= 1 - \frac{\Delta t}{t_{final} - k\Delta t} \\
&= 1 - \frac{\Delta t}{t_{final} - \left(\frac{t_{final}}{\Delta t} - 1\right)\Delta t} \\
&= 1 - \frac{\Delta t}{t_{final} - t_{final} + \Delta t} \\
&= 1 - 1 \\
&= 0
\end{aligned} \tag{5.37}$$

The state transition matrix $\Phi\left(\frac{t_{final}}{\Delta t}, 0\right)$ is thus zero, satisfying arrival at the goal point and avoiding the singularity. The physical interpretation of this is that the aircraft reaches the goal point at $\left(\frac{t_{final}}{\Delta t}\right)_-$, the beginning of the timestep where the singularity occurs. The goal point is thus controllable from any starting state and any choice of a threshold for “reaching” the waypoint will avoid the singularity. Note that while the goal point is controllable from any starting state, there is no restriction placed on the control effort required in order to do so. As with any control design problem, it is incumbent on the system designer and aircraft management system to operate the controller within a physically sensible operating space.

The previous analysis does not include the effect of varying speed in response to the stochastic energy input. As the speed variations are in response to stochastic atmospheric characteristics, the speed will be modeled as subject to a random disturbance: $v_k = v_{command} + \zeta_k$ so that the state transition can be written:

$$\begin{aligned}
x_{k+1} &= x_k + \Delta t (v_{command} + \zeta_k) \\
&= x_k + \Delta t \frac{-x_k}{t_{final} - k\Delta t} + \Delta t \zeta_k \\
&= x_k \left(1 - \frac{\Delta t}{t_{final} - k\Delta t}\right) + \Delta t \zeta_k
\end{aligned} \tag{5.38}$$

The input response must be included in the transition:

$$x_{k+1} = \Phi_{k+1}x_0 + \sum_{i=0}^k \Phi(k+1, i+1)\Delta t \zeta_i \tag{5.39}$$

Noting that $\Phi(j, j) \equiv 1$ and again recursively applying the dynamics, the state

transition can be determined:

$$\begin{aligned}
x_{k+1} &= x_0 \prod_{i=0}^k A(i) + \sum_{i=0}^{k-1} \left(\Delta t \zeta_i \prod_{j=i+1}^k A(j) \right) + \Delta t \zeta_k \\
&= x_0 \prod_{i=0}^k \left(1 - \frac{\Delta t}{t_{final} - k\Delta t} \right) + \sum_{i=0}^{k-1} \left(\Delta t \zeta_i \prod_{j=i+1}^k \left(1 - \frac{\Delta t}{t_{final} - j\Delta t} \right) \right) + \Delta t \zeta_k
\end{aligned} \tag{5.40}$$

As before, the zero input response goes to 0 when $k = \frac{t_{final}}{\Delta t} - 1$. The zero state response also goes to zero for every term in the summation in Equation 5.40 as the product always includes the system matrix $A\left(\frac{t_{final}}{\Delta t} - 1\right) = 0$. The only term remaining in the zero state response is $\Delta t \zeta_{\frac{t_{final}}{\Delta t} - 1}$, the disturbance at the final step. The desired final state is no longer completely controllable from any state, but can be achieved up to some final error $x_{error} = \Delta t \zeta_{\frac{t_{final}}{\Delta t} - 1}$. Assuming that the controller is shut off at t_{final} , the arrival time error can be approximated by the final error and the nominal speed:

$$t_{error} = \frac{x_{error}}{\bar{v}} = \frac{\Delta t \zeta_{\frac{t_{final}}{\Delta t} - 1}}{\bar{v}} \tag{5.41}$$

It is worth noting that throughout this development, the disturbance was not assumed to have any particular statistical structure (e.g. normally distributed). This means that the exact nature of the aircraft response to stochastic energy inputs is not critical to satisfying the arrival time condition (up to the error term). Further, the speed error is not restricted to speed commands for energy harvesting, the analysis applies to any source of error in the aircraft speed.

This result can also be used to determine a minimum arrival threshold to ensure that the controller is shut off before reaching the singularity. If the maximum speed error can be estimated, a lower bound for the threshold can be determined based on the maximum position error at the final time:

$$x_{threshold} < x_{error} \approx \max(\zeta)\Delta t \tag{5.42}$$

Assuming a quadratic polar and referencing Equation 5.26, the disturbance in the speed command can be estimated based on the largest expected disturbance in \hat{p}_i . Assuming that the nominal mean speed is equal to the speed for maximum

range and that there is no wind, then Equation 5.31 will yield $MC = \mathbb{E}(\hat{p})$. The velocity disturbance can be computed:

$$\begin{aligned} \max(\zeta) \approx |\max(v) - \bar{v}| &= \left| \sqrt{\frac{c - MC - \max(\hat{p})}{a}} - \sqrt{\frac{c - MC}{a}} \right| \\ &= \left| \sqrt{\frac{c - \mathbb{E}(\hat{p}) - \max(\hat{p})}{a}} - \sqrt{\frac{c - \mathbb{E}(\hat{p})}{a}} \right| \end{aligned} \quad (5.43)$$

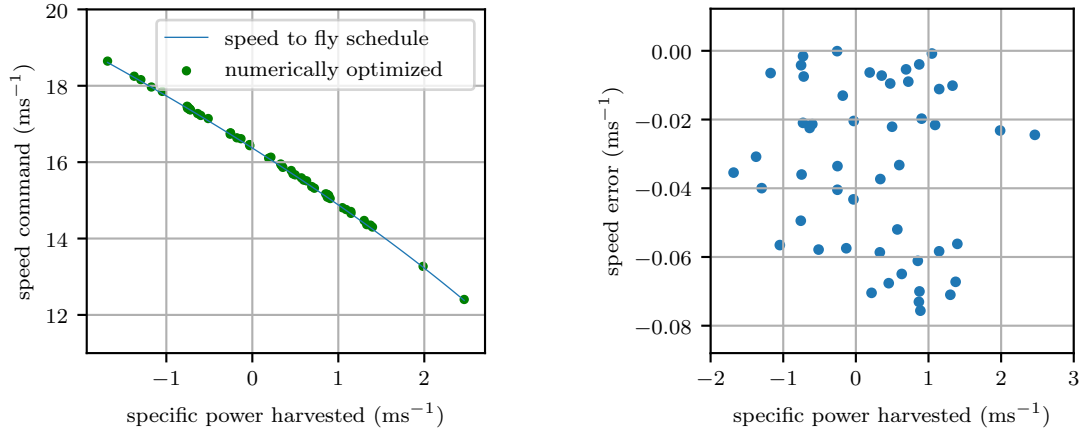
Using values of a and c from the SB-XC, $MC = 0$, and letting $\max(\hat{p}) \approx 2 \text{ m s}^{-1}$ (a fairly large vertical updraft), the maximum disturbance is approximately 4 m s^{-1} . If the controller time step is 1.0 s then this would indicate a threshold of about 4.0 m would be appropriate, larger than differential GPS accuracy, but smaller than is commonly used on fixed wing UAS for navigation thresholds. Equation 5.42 can alternatively be viewed as a means to select a required controller time step size given a navigation performance requirement.

5.2 Simulations

The speed to fly schedule from section Section 5 was studied using two numerical approaches. In both, the aircraft simulated is the SB-XC, described in Section 3.4.1. For these simulations, it is assumed that solar cells cover 30% of the SBXC's wings, this value is chosen so that it is not capable of sustained flight on solar power alone.

5.2.1 Approximating the MacCready Number

To validate the approximation to MC given by Equation 5.30, a numeric approach is adopted to finding the speed schedule which satisfies Equations 5.23 and 5.24. The SciPy `minimize` routine [91], is used to minimize Equation 5.13 subject to a mean speed constraint of 16 m s^{-1} over 50 segments. A candidate schedule was also computed using equation 5.30. Segment lengths were drawn from a uniform distribution with a maximum value of 1000.0 m. The energy harvest rate for each segment, \hat{p} , was drawn from a Gaussian random distribution with mean of 0.3 m s^{-1} (so that the mean energy harvesting rate is almost enough to remain aloft) and unit standard deviation (approximately the vertical velocity variance in a



(a) Optimal speed as a function of harvested energy. Also plotted is the speed to fly curve evaluated with MC computed as in equation 5.31.

(b) Error in the speed command from equation 5.26 versus the numerically optimized speed.

Figure 5.5: Performance of the approximate unified speed to fly computation with arrival time constraint. The MacCready value is 2.26 m s^{-1} , computed by solving Equation 5.31.

moderately convective boundary layer). The results are illustrated in Figure 5.5.

The MacCready value was determined by recursively applying Equation 5.30, computing $\mathbb{E}(\hat{p})$ for this schedule, then recomputing the MC value. This was repeated until the MC value converged. This approximates the value for $\mathbb{E}(\hat{p})$ which could be computed by a running average on the aircraft. Figure 5.5a shows that the speed to fly schedule lies nearly on top of the numerically optimized speed schedule, the speed command errors are shown in figure 5.5b and are below 1%, validating the approximation made in Equation 5.30. The average speed is slower than the desired speed by 0.056 m s^{-1} , or 0.35%.

5.2.2 Monte Carlo Simulations

The speed to fly algorithm is tested more extensively in a Monte Carlo simulation. The aircraft is represented as a point mass with states: east position, altitude, and stored specific energy. The simulation model and state dynamics are described in Section 3.2.2. Power commands, \tilde{p} are generated by a proportional-integral control

loop which seeks to keep the aircraft at an altitude of 500 m.

The environment is defined by randomly scattered clouds and thermals. Thermals are modeled as described in Section 3.3.3 Parameters for the thermals are shown in Table 5.1. The horizontal wind is set to zero.

Table 5.1: Parameters of the thermal model used in the simulations.

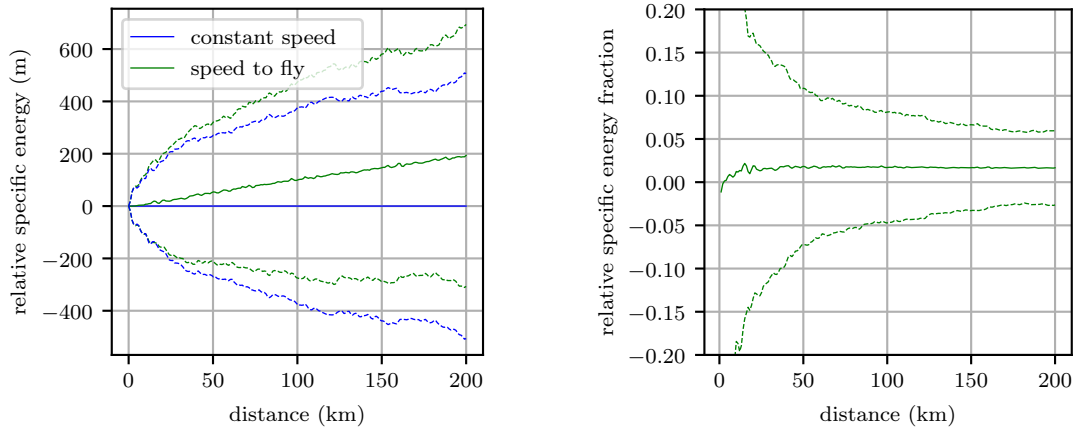
number of thermals	100
locations	$\mathcal{U}(0, 200 \text{ km})$
r_{scale}	$\mathcal{N}(200 \text{ m}, 10000 \text{ m}^2)$
w_{scale}	$\mathcal{N}(0, 1.0 \text{ m}^2\text{s}^{-2})$

Clouds are modeled as by sharp-edged reductions in the solar input. For a clouded segment, the global insolation is multiplied by the “cloud factor” which represents the fraction of total solar power available. The nominal global insolation is set to 750 W m^{-2} to represent the effect of a suboptimal solar angle because of latitude and time of day. Parameters for the solar model are depicted in Table 5.2.

Table 5.2: Parameters of the cloud model used in the simulations.

number of clouds	50
locations	$\mathcal{U}(0, 200 \text{ km})$
r_{scale}	$\mathcal{N}(1000 \text{ m}, 100 \text{ m})$
cloud factor	$\mathcal{N}(0.3, 0.04)$ (clipped to $[0, 1]$)
solar insolation	750 W m^{-2}

For each simulation iteration a random cloud and thermal environment is generated and then two aircraft are simulated through the same environment over a 200 km flight with a desired mean speed of 16 m s^{-1} for a nominal time of 12500 seconds (≈ 3.5 hours). The speed command is selected so that the aircraft must fly faster than the speed for best $\frac{L}{D}$, as is common in cruise for small aircraft at low altitude. One aircraft flies a constant speed while the other flies the speed schedule developed in section 5.1.3.1. The expected energy harvest rate is initialized by taking the average of 1000 random samples of the environment and thereafter determined using a first order lowpass filter with a time constant of 30 minutes.



(a) Energy savings for flying the speed to fly schedule.

(b) Energy savings expressed as a fraction of the energy required for constant speed flight.

Figure 5.6: Ensemble mean energy savings achieved using speed to fly over 100 Monte Carlo simulation iterations. Dotted lines indicated one standard deviation.

Figure 5.6 illustrates the mean savings that can be achieved by flying speed to fly, computed over 100 Monte Carlo simulation iterations. On average, the speed to fly schedule will reduce the energy required to fly a mission by about 2%, illustrated in figure 5.6b which is consistent with the gains seen in section 5.1.1 for optimal response to clouds for a pure solar aircraft, it is also consistent with the experience of soaring pilots [35]. Figure 5.6a shows the difference in energy between the speed to fly and constant speed approaches and the uncertainty in energy state for each aircraft plotted against travel distance. While it is difficult to read directly from the figure, flying the speed to fly results not only in energy savings but in a slight reduction in uncertainty of the final energy state (about 3% reduction in the standard deviation of the final energy state).

Figure 5.7 shows the difference in energy between an aircraft using speed to fly compared to one in constant speed flight for a randomly selected Monte Carlo iteration. The figure also illustrates the components of \hat{p} : clouded regions are shown shaded by $1 - \alpha$ (the fraction of light blocked by the cloud) and the relative energy line is colored by vertical air motion (red and blue for rising and sinking air respectively). The aircraft which uses speed to fly speed steadily gains energy over the constant speed aircraft though it is difficult to assign energy gains to specific

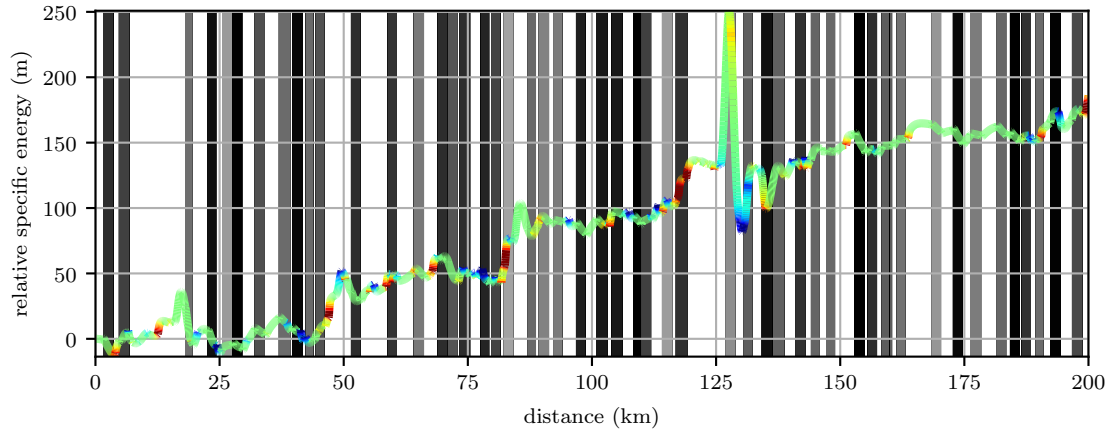


Figure 5.7: Difference in total energy (kinetic + potential - expended stored energy) between an aircraft employing the speed to fly schedule and an aircraft in constant speed flight for one run from the Monte Carlo set.

phenomena. When crossing a cloud shadow the speed to fly command increases, also increasing drag but it takes some time for the altitude controller integrators to unwind and increase power output so the cost to cross the shaded region won't be fully realized until later. This effect is especially evident at around 130 km. Both aircraft are descending as they fly through a clouded region. The speed to fly aircraft has a higher initial altitude so it turns on its motor after the constant speed aircraft, causing an apparent spike in the relative energy. The mean trend however shows that flying the speed to fly leads to consistent gains in energy relative to constant speed flight.

The distribution of error in mean speed over for the Monte Carlo set is depicted in Figure 5.8. The mean error is 0.05 m s^{-1} , less than 1% of the commanded speed. The slowest speed of all iterations was 15.90 m s^{-1} while the fastest was 15.97 m s^{-1} . This implies a maximum deviation from the desired arrival time of 78 seconds over a flight time of approximately 3.5 hours. The speed error is consistent with the error demonstrated in the first simulation experiment from section 5.2.1.

5.3 Flight Tests

To provide further validation of the speed control algorithm, it was implemented on the Vulture, a small powered sailplane described in Section 3.4.2. The aircraft

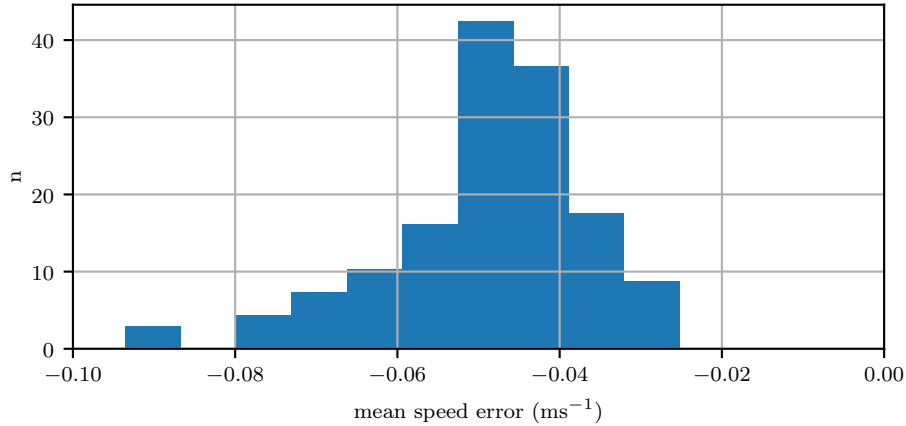


Figure 5.8: Distribution of error in the mean speed. In 100 iterations no aircraft finished with more than 0.1 m s^{-1} of error. The mean error is 0.05 m s^{-1} , less than 1% of the nominal speed, 16 m s^{-1} .

was commanded to fly several missions which were to arrive at a specified location at a specified time.

5.3.1 Mission Description

The aircraft is commanded to fly a flight path in the shape of a hypotrochoid (“spirograph” pattern) 10115 meters in length at an average speed of 14.0 m s^{-1} , for a nominal flight time of 722.55 seconds (≈ 12 minutes). There was concern that flying a circle would lead to the aircraft repeatedly re-encountering the same atmospheric conditions (the characteristic timescale for the lower troposphere is ≈ 600 seconds [10]). The hypotrochoid provides a long path with minimal curvature that revisits relatively few points and fits within a compact flight area. The test speed was chosen so that the aircraft must fly faster than its best L/D speed, and path length chosen so that the test duration left considerable reserve power in the battery for recovery.

During the test a new MC value is generated every 5.0 seconds. It is assumed that there is no net energy harvested on average, i.e. that $\mathbb{E}(\hat{p}) = 0$. At first glance, this assumption appears to be in conflict with our objective of using speed to fly to reduce the energy consumption. Given that the aircraft is not equipped with solar cells and that the large-scale average vertical air motion is zero, the energy

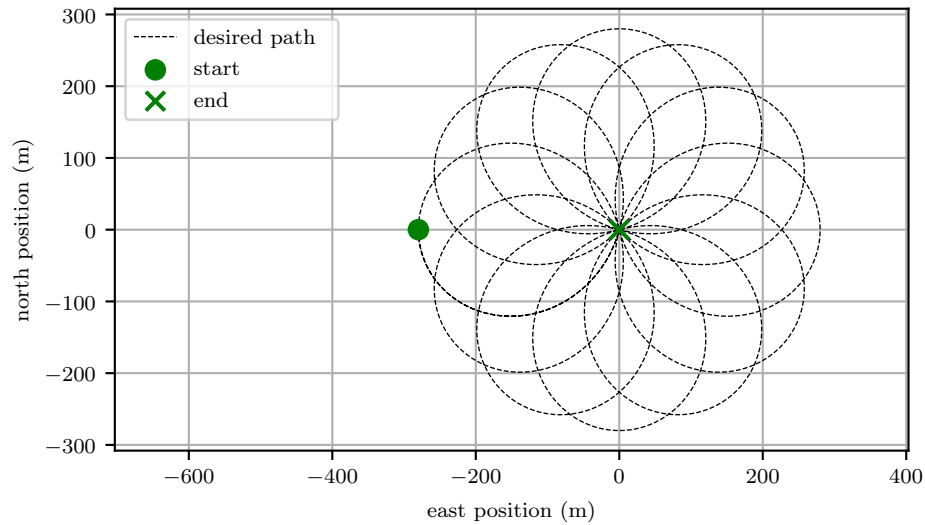


Figure 5.9: Desired flight path for the speed to fly test. The aircraft travels in an anti-clockwise path starting at the green circle with the “petals” precessing anti-clockwise as well. The aircraft completes the test at the center point.

harvested should be relatively small so the error introduced should be eliminated by subsequent computations of the required MC value. The nominal flight path is depicted in Figure 5.9. The flight path begins at $[-250 \text{ m}, 0 \text{ m}]$ and ends at $[0 \text{ m}, 0 \text{ m}]$. The aircraft proceeds anti-clockwise, the “petals” precess anti-clockwise as well.

5.3.2 Results

The flight path was flown 6 times. In each test the wind was assumed to be still when computing the required MacCready number, so the wind appears as an unmodeled disturbance. Table 5.3 illustrates the schedule keeping performance.

Given a mean wind speed of roughly 3.0 m s^{-1} and the amount of vertical motion experienced, errors of up to 1.3 seconds or 0.18% are anticipated by Equation 5.41. Table 5.3 indicates greater error for all flights, often exceeding the expected error by several times. The reason for the error can be explored by examining a particular flight in greater depth. Figure 5.10 shows the aircraft flight path during the third trial. The aircraft completed the path in 720.37 seconds, an error of -2.18 seconds or approximately 0.3%.

Table 5.3: Time of arrival performance for the flight test.

trial	nominal time	elapsed time	error (s)	error (%)
1	722.55	717.09	-5.46	-0.76
2	722.55	715.64	-6.91	-0.96
3	722.55	720.37	-2.18	-0.30
4	722.55	719.64	-2.93	-0.40
5	722.55	721.16	-1.39	-0.19
6	722.55	718.72	-3.83	-0.53

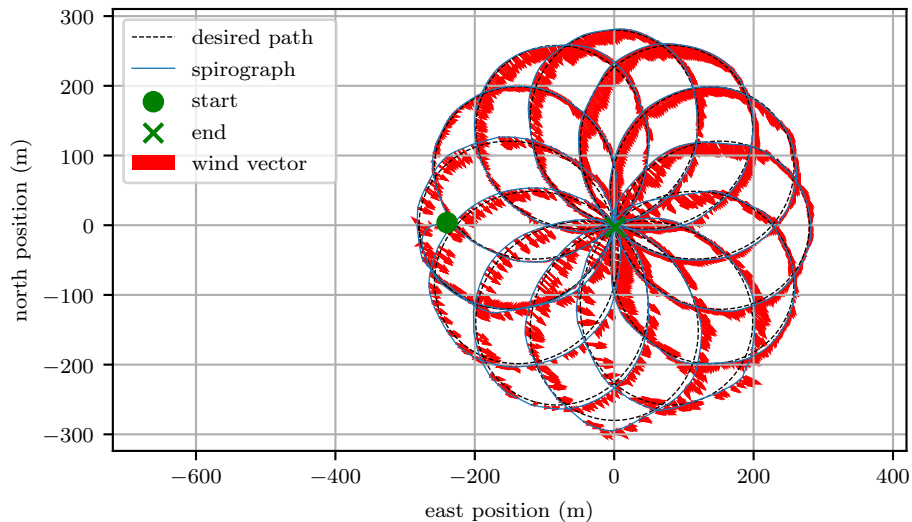


Figure 5.10: Actual flight path during one speed to fly test. The wind is depicted as vectors along the flight path and was left unmodeled as a disturbance the controller had to eliminate. The mean north wind component was -2.56 m s^{-1} and mean east component was 2.82 m s^{-1} .

Figure 5.11 depicts the time history of the airspeed, commanded airspeed, vertical air motion, and MacCready number for the third trial. The aircraft varies its speed substantially in response to vertical air motion, between approximately 10.0 and 20.0 m s^{-1} . The MacCready number is relatively constant for much of the flight. Late in the flight, the required speed becomes more sensitive to error as the time remaining decreases, causing more variation in the MacCready number. At $t \approx 550$ seconds and $t \approx 600$ seconds the MacCready number can be seen increasing

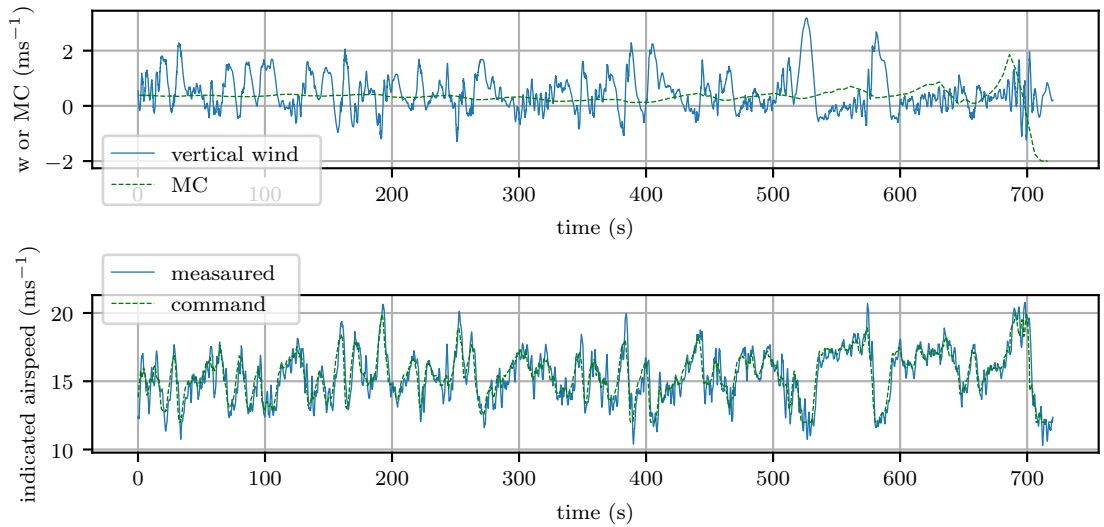


Figure 5.11: Command and state histories during the speed to fly test. Late in the test the MacCready setting begins to vary in response to vertical motion (the aircraft slows down when flying in rising air, requiring an increased MacCready number in order to satisfy the time of arrival).

after the aircraft slows as it traverses an area of updraft. At $t > 680$ seconds the MacCready number decreases rapidly and the aircraft slows to its minimum allowable speed.

The error in flight 2 was approximately 60% greater than Equation 5.41 would expect. The additional error is due to constraints placed on the MacCready value which are outside the scope of analysis of Section 5.1.3.3. The aircraft began the last half-petal by flying directly downwind, the strong wind (greater than 20% of the nominal mean speed) increased the aircraft's groundspeed by enough to generate a MC value below the lower saturation limit, set to ensure the aircraft remained above the stall speed. This accumulated enough error that even after turning crosswind, there was not enough time remaining in the trajectory to fully eliminate the error. This effect can be seen in Figure 5.11.

The flight test demonstrates that even in the presence of significant unmodeled dynamics the controller can achieve a desired time of arrival at a point of interest with an error of less than 1% of the flight time. Further, the controller shows stable performance even as the time remaining decreases and the command becomes more sensitive to error. Energy consumption is not examined in the flight test as

the performance improvement would be difficult to confidently measure without significant numbers of both experimental and control flights.

5.4 Summary

Soaring speed to fly theory is extended, permitting it to be used to determine optimal speed response to variations in solar energy. One extension of speed to fly theory enables determination of a speed command which permits a solar powered aircraft to minimize the impact of solar interruptions on average speed. A second extension of speed to fly theory generalizes the energy input to include both solar input and vertical motion. This approach demonstrates the power of analyzing the aircraft power budget, including solar energy, as specific aerodynamic power. Using specific power permits combining multiple sources of energy and gives kinematic meaning to the power budget.

By permitting the aircraft to expend energy stored onboard, an average speed constraint can be introduced to allow an arrival time to be satisfied. Computing this speed schedule requires knowledge of the atmospheric state, an approach to approximate the required atmospheric knowledge is suggested. The convergence of the proposed control method to the desired final state is analyzed and a means to select an appropriate arrival threshold is discussed.

Numerical experiments are used to validate the speed commands. A numerically optimized solution computed with full knowledge of the environment is used to validate the speed schedule. The speed command with arrival time condition is tested in a Monte Carlo simulation against an aircraft which flies at constant speed. Flying the speed to fly reduces the energy required to fly a given distance by approximately 2%, reduces the uncertainty in final energy state by approximately 3%, and satisfies the desired arrival time to within 1%.

Finally, the speed command for arrival time algorithm is implemented on a small UAS and tested in a series of flight experiments. Even in the presence of unmodeled disturbances the controller achieves an arrival time error of less than 1%. The theoretical development, numerical and simulation validation, and flight tests describe a control policy which can guide a solar augmented aircraft to arrive at a designated point at a desired time while saving energy. A modest reduction in energy is achieved along with improved certainty in the final energy state with no

design changes to the vehicle.

Chapter 6 | Modeling the Environment

Section 5.1.2 demonstrated that speed variations can be used to respond to the stochastic component of the environmental state. The aircraft should also respond to the mean atmospheric state in a way that minimizes its use of stored energy. In order to do so, a model of the atmosphere is required. Reviewing the design goals laid out in Section 1.2, the atmospheric modeling system should have a few characteristics:

- It should include environmental properties which influence the aircraft's energy budget.
- The model should be constructed from *in situ* observations.
- It should be possible to incorporate observations from other aircraft or sensors.

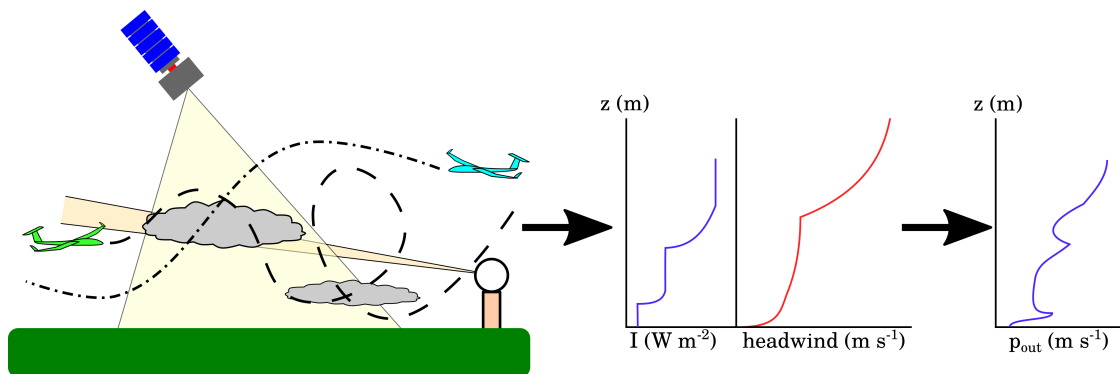


Figure 6.1: The aircraft environmental model should be able to be constructed onboard the aircraft from *in situ* observations but be able to incorporate observations from other platforms if available. It should model the atmospheric structure in a way that permits transformation into other quantities of interest.

Figure 6.1 illustrates this problem schematically. To simplify implementation and use of the atmospheric modeling system and to make it robust to a wide variety of conditions there are a few other desirable features:

- The model should have relatively few parameters to “tune.”
- The model structure should not expect a specific atmospheric structure.
- Updating and evaluating the model should scale efficiently to large numbers of observations.
- The model should provide information about the confidence in its representation of the environment.
- It should be possible to combine several model states into a model for some other parameter, e.g. the cost to loiter or achieve a desired inertial velocity.

Since the aircraft’s awareness of and response to the environment is restricted to the vertical plane, the model need only represent a single dimension. Wind, solar insolation, and mean vertical air motion have the largest effect on the aircraft’s energy budget, so these properties will be included in the model. To simplify handling celestial dynamics, the solar radiation will be represented by the “cloud factor” introduced in Section 3.3.1. This permits the expected solar insolation at any time to be retrieved by multiplying the clear sky insolation by the cloud factor.

A number of approaches are commonly used to represent arbitrary environments. Perhaps the most common and flexible is Gaussian Process regression [92]. Gaussian processes have been used in the past to model unknown wind fields for small UAS planning [93, 94]. However, Gaussian process regression scales poorly with large numbers of observations as it requires maintaining and inverting a matrix with dimension equal to the number of observations.

An approach which provides much of the flexibility of Gaussian Process regression but in a more computationally tractable form is to specify a fixed set of basis functions *a priori* and estimate model coefficients on this basis. A commonly used basis is spline functions.

6.1 Modeling with Basis Splines

Splines functions are commonly used to interpolation unstructured data. They can represent arbitrary functions and the degree of continuity in derivatives can be chosen by the order of the spline [95]. A spline is specified by a series of “knots,” or control point locations, and the order of derivative which is permitted to have discontinuities at the knots. For instance, a first-order spline is piecewise linear function between the knots. Cubic splines are most commonly used and offer C^2 continuity.

The exact mathematical representation of a spline can be expressed in several ways, including as piecewise continuous polynomial functions. For the purposes of recursively building an environmental model, basis splines are the most convenient. In basis spline, or B-spline form, a series of spline functions are defined covering the domain of the model. Each spline has limited support near a particular knot and the spline functions form a partition of unity at each point in the domain of the model, that is [95]:

$$\sum_{i=0}^{n+k-1} N_i(z) = 1 \quad \forall x \in [z_{knot,min}, z_{knot,max}] \quad (6.1)$$

Where $N_i(z)$ is the value of basis i at point z , n is the number of knots in the spline and k is the spline order. At a desired point z , the value of a function can be represented as a linear combination of the spline functions. Coefficients, c_i specify the influence of each spline basis:

$$f(z) = \sum_{i=0}^{n+k-1} N_i(z)c_i = \mathbf{N}(z)\mathbf{c} \quad (6.2)$$

Where $\mathbf{N}(z)$ is a row vector of spline basis functions evaluated at point z and \mathbf{c} is a column vector of spline coefficients. A spline can thus be thought of as a mapping from an $n + k - 1$ vector to a scalar value $f \in [z_{knot,min}, z_{knot,max}]$. Finding a model to fit a function requires finding the spline coordinate vector which minimizes the difference between the spline model and function values.

With four atmospheric parameters to model, four sets of spline coordinates will have to be estimated, representing the wind vector, cloud factor, and mean vertical air motion respectively. The four parameters will be modeled with separate

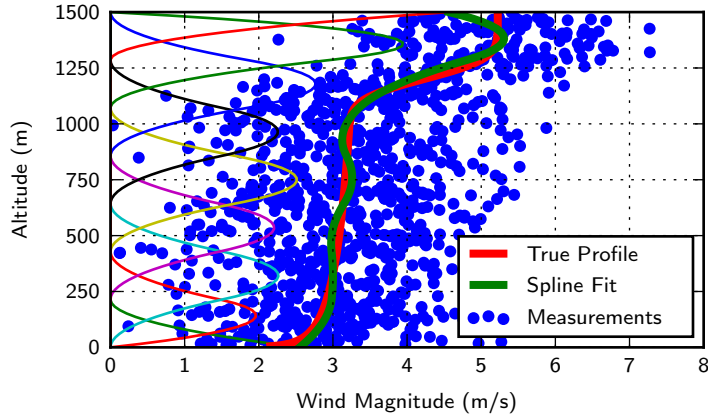


Figure 6.2: Basis splines can be used to approximate functions by a linear combination of the bases at each point. The coefficients for this model were determined by a least square fit of the noisy data. Spline bases are shown scaled by their respective coefficients.

Kalman filters, implicitly assuming that there is no correlation between the mean value of each parameter. To simplify calculations, each will use the same order and basis, although different bases could be used if required to provide additional model resolution for each parameter in different areas.

Equation 6.2 shows that the value of a spline model evaluated at a point is determined by a linear combination of the bases. If a process to be modeled is assumed to be represented by spline coefficients \mathbf{c} , then an approximate model can be constructed from noisy observations $y_j = \mathbf{N}(x_j)\mathbf{c} + v$ where v is noise in the observation [96]. This is a classic linear model fitting problem, it could be solved for a batch of observations using least-square estimation:

$$\hat{\mathbf{c}} = (\mathbf{N}^T(\mathbf{z})\mathbf{N}(\mathbf{x}))^{-1} \mathbf{N}^T(\mathbf{z})\mathbf{y} \approx \mathbf{c} \quad (6.3)$$

Figure 6.2 shows an example of spline bases and a function approximated by a linear combination of the bases with the coefficients determined by least square fit of noisy data.

Alternatively, the environment can be viewed as a dynamic system and the coefficients \mathbf{c} as its states. Since the basis spline is linear, the coefficient vector can be estimated recursively using a Kalman Filter as observations of the environment are received. The observation model is just the spline basis evaluated at the

observation location, Equation 6.2. A form of this model was used to determine the wind shear value for a dynamic soaring aircraft [97].

6.1.1 Time Update

Predictions of the evolution of the atmospheric state can be used to update the spline model. Since several splines influence the value of the model at each point, updating the spline coefficients is not as simple as applying the rate of change of the atmospheric state at a knot location to the appropriate coefficient. Writing the state of interest generically, the state derivative is related to the coefficient derivatives:

$$\frac{\partial f(z)}{\partial t} = \frac{\partial \mathbf{N}(z)\mathbf{c}}{\partial t} = \frac{\partial \mathbf{N}(z)}{\partial t}\mathbf{c} + \mathbf{N}(z)\frac{\partial \mathbf{c}}{\partial t} \quad (6.4)$$

If the spline knot locations are to remain constant, then $\frac{\partial \mathbf{N}(z)}{\partial t} = 0$. This may not be the case if the knot locations are permitted to change, which may be used to provide greater knot density (and thus resolution) at the boundary layer top or some other region of interest which is not fixed in space. For this work the knot locations are left constant.

Assuming that the atmospheric state derivatives are available at discrete points (e.g. at the grid location of a numerical weather prediction model) then the best fit derivative of the coefficient vector can be computed using the psuedoinverse:

$$\frac{\partial \mathbf{c}}{\partial t} = (\mathbf{N}^T(\mathbf{z})\mathbf{N}(\mathbf{z}))^{-1} \mathbf{N}^T(\mathbf{z})\frac{\partial f(\mathbf{z})}{\partial t} \quad (6.5)$$

Note that in order for the psuedoinverse to be nonsingular the derivative must be known at $n + k - 1$ points, and also there must be a sample point z_n in the support of every spline basis.

If time derivatives of the atmospheric state are not available, it can be modeled simply as a random walk. In this work, the High Resolution Rapid Refresh (HRRR) numerical weather prediction model is used to determine the time derivative of the expected environmental state [77]. Time derivatives are determined by a central finite difference of the HRRR state at the observation time with a step size equal to half the HRRR output time step.

6.1.2 Process Noise

Since both the mean and distribution of the environmental state is of interest, it is important to determine an appropriate value for the process noise. The model framework chosen and information available will influence the meaning and choice of process noise. If a prediction of the evolution of the atmospheric state is available (for example, from a numerical weather model), the Kalman Filter framework permits it to be incorporated and fused naturally with *in situ* observation. In this case the process noise represents the growth of error in the forecast with time. If a prediction of the state evolution is not available then the process noise should be chosen to represent the rate of change of the state in a random walk.

To determine an appropriate process noise, the HRRR analysis and forecast was obtained for 900 forecast periods. In engineering parlance the analysis step of a weather model is the “measurement update,” observations from weather sensors are used to update the model and provide a best estimate of the current state of the atmosphere before beginning a forecast. Figure 6.3 illustrates how the analysis step of subsequent forecasts is used as “truth” to compute forecast error. Forecast error is computed by finding the difference between the forecast and the model analysis at each hour. For instance, given an hourly forecast initialized at 12:00 UTC, the one-hour forecast error is the difference between the forecast for T_0+1 hour and the analysis from a run initialized at 13:00 UTC, the two-hour error is the difference between the forecast for T_0+2 hours and the analysis from the 14:00 UTC run, and so on.

The mean forecast error can then be computed by averaging the one-hour, two-hour, etc error over many forecast periods. Figure 6.4 illustrates the mean wind error versus forecast hour for several model levels at an example point in central Pennsylvania.

Figure 6.4 shows that the forecast error has some variation with height. While in principle the process noise could vary with height, the appropriate scaling parameter at low altitude is height above ground level so a map of terrain elevation would have to be carried and referenced when selecting the process noise. For the point examined in Figure 6.4, the variation in forecast error with height is greatest in the lowest 100 meters or so, especially for short forecast periods. Since most aircraft cruise at altitudes above 100 meters and to simplify construction of the filter,

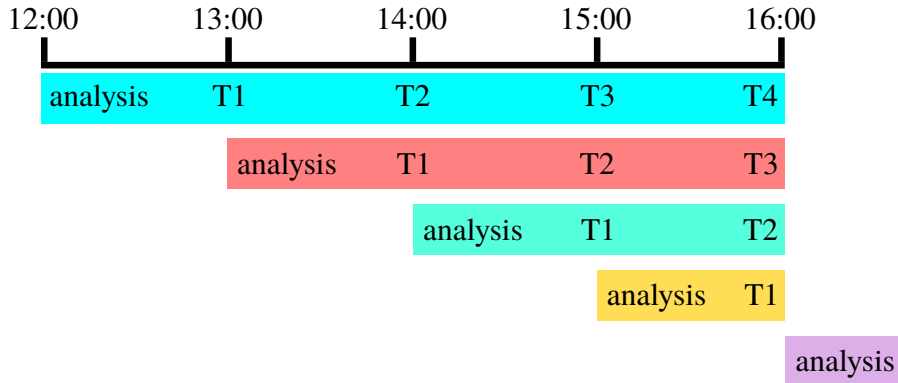
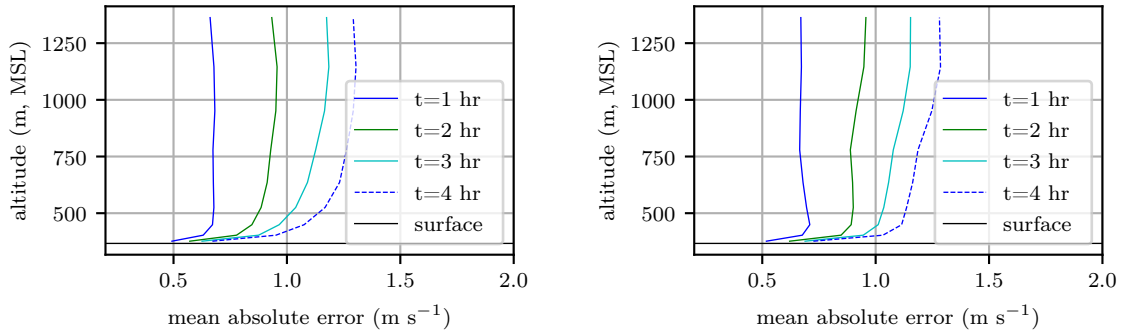


Figure 6.3: The forecast error at each hour is computed using a triangular scheme and the analysis from subsequent forecast times as “truth.” For instance the one-hour forecast error for the 12:00 UTC forecast is the value of the desired fields from the 12:00 UTC T1 step minus the analysis value from the 13:00 UTC forecast.



(a) East wind error (positive is air parcels moving east)

(b) North wind error (positive is air parcels moving north)

Figure 6.4: Mean absolute error profiles for the HRRR wind forecast at a point in central Pennsylvania.

this work uses a constant value of $0.9504 \text{ m}^2 \text{ s}^{-2} \text{ h}^{-1}$ for process noise, the wind magnitude variance computed from the mean 1 hour forecast error.

For very large flight areas that cross regions with significantly varying atmospheric dynamics, a process noise map could be constructed which allows the process noise to vary with position and perhaps with time of day and year. Again, to simplify the filter in this work, a single static value is used.

For constant values of environmental process noise it can easily be related to the spline coefficients. Since the spline functions sum to 1 at all points in the domain, a

uniform increase in uncertainty can be accomplished with a diagonal process noise matrix.

$$\mathbf{Q} = \mathbf{I}_{n+k-1}Q \quad (6.6)$$

If the process noise is permitted to vary with height then the forecast error growth must be transformed into error growth in the spline coefficients. Since the spline model is a linear transformation applied to the spline coefficient vector, if the covariance of this vector is known, then the variance of any point in the spline model can be computed:

$$P_f(z) = \mathbf{N}(z)\Sigma_{\mathbf{c}_f}\mathbf{N}^T(z) \quad (6.7)$$

If the growth rate of the variance in the modeled quantity, $\frac{\partial P_f(z)}{\partial t}$ is known, then the time derivative of the spline coefficients can be computed in a manner analogous to computing the time derivative of the coefficients described in Equation 6.5:

$$\frac{\partial P_f(\mathbf{z})}{\partial t} = \frac{\partial \mathbf{N}(\mathbf{z})}{\partial t}\Sigma_{\mathbf{c}_f}\mathbf{N}^T(\mathbf{z}) + \mathbf{N}(\mathbf{z})\frac{\partial \Sigma_{\mathbf{c}_f}}{\partial t}\mathbf{N}^T(\mathbf{z}) + \mathbf{N}(\mathbf{z})\Sigma_{\mathbf{c}_f}\frac{\partial \mathbf{N}^T(\mathbf{z})}{\partial t} \quad (6.8)$$

Assuming that the spline bases themselves are stationary, then second term is the only one which is not trivially zero. Applying the pseudoinverse to the basis functions in Equation 6.8, the time derivative of the spline coefficients can be computed:

$$\frac{\partial \Sigma_{\mathbf{c}_f}}{\partial t} = (\mathbf{N}^T(\mathbf{z})\mathbf{N}(\mathbf{z}))^{-1}\mathbf{N}^T(\mathbf{z})\frac{\partial P_f(\mathbf{z})}{\partial t}\mathbf{N}(\mathbf{z})(\mathbf{N}^T(\mathbf{z})\mathbf{N}(\mathbf{z}))^{-1} \quad (6.9)$$

As in Equation 6.5, the derivative, $\frac{\partial P_f(\mathbf{z})}{\partial t}$ must be known at at least $n + k - 1$ points with some points in the support of all spline bases. Given a Kalman Filter integration step size Δt_{kf} , the process noise can be approximated:

$$Q \approx \Delta t_{kf}\frac{\partial \Sigma_{\mathbf{c}_f}}{\partial t} \quad (6.10)$$

6.1.3 Observation Models

The observation model for a linear Kalman Filter is defined [96]:

$$\hat{\mathbf{y}} = \mathbf{C}\hat{\mathbf{x}} \quad (6.11)$$

Which predicts the expected measurement \mathbf{y} for state \mathbf{x} . The modeled atmospheric state at each point is a linear combination of the basis functions:

$$f = \mathbf{N}(z)\mathbf{c}_f \quad (6.12)$$

So the basis function evaluated at the point of interest form the observation model. They represent the influence that each coefficient has on the model value at the observation point.

Sometimes multiple observations might be available simultaneously. This could happen when receiving a wind profiler measurement, a batch of observations from nearby aircraft, or a model analysis. This observation model can easily be extended to incorporate multiple simultaneous observations by writing an extended basis matrix as the observation model:

$$\mathbf{f} = \mathbf{N}(\mathbf{z})\mathbf{c}_f \quad (6.13)$$

Where \mathbf{N} is now an $m \times (n+k-1)$ matrix where m is the number of observations available.

6.1.4 Measurement Noise

Just as a sample from a sensor includes contributions from the mean value to be measured and a random disturbance due to sensor noise, the atmospheric state includes a mean and turbulent component [10]. Measurement noise thus arises from two sources – noise that is a function of error in the sensors and aircraft dynamics, and noise that is introduced because the point sampled is not representative of the environment as a whole. To clarify the distinction the first will be referred to as sensor noise and the second as sample noise.

Sensor noise is relatively straightforward to define. The sensors themselves can be characterized to determine their measurement variance. In some cases, a measurement may be synthesized from several sensors (e.g. the wind vector). In this case each sensor individually can be characterized and the overall error be determined by propagation of error.

Sensor noise in the wind vector has been studied by several authors and techniques to compute it are well established [98,99] For solar fraction, the solar array power electronics, current and voltage monitoring noise, and aircraft attitude all influence the energy production. Voltage and current can be measured very accurately, the assumption is made here that sensor error in the solar fraction is dominated by error in the aircraft's attitude. The sensitivity of cloud factor to attitude error can be determined:

$$\frac{\partial \alpha}{\partial \Theta} = \frac{\partial}{\partial \Theta} \frac{I_{observed} \cos \hat{i}}{I_{clear\ sky} \cos i} = \frac{I_{observed}}{I_{clear\ sky} \cos i} \frac{\partial \cos \hat{i}}{\partial \Theta} \quad (6.14)$$

Where i is the true angle between the aircraft $-z$ axis and the sun, and \hat{i} is the expected angle based on the sensed aircraft attitude. Noting that $\cos i$ is the dot product of the aircraft $-z$ axis resolved in inertial axes with a unit vector to the sun, the aircraft $-z$ axis can be transformed by the body-to-inertial coordinate rotation [72] and $\cos i$ can be written:

$$\cos i = \begin{bmatrix} s_x & s_y & s_z \end{bmatrix} \begin{bmatrix} \sin \phi \sin \psi + \cos \phi \sin \theta \cos \psi \\ -\sin \phi \cos \psi + \cos \phi \sin \theta \sin \psi \\ \cos \phi \cos \theta \end{bmatrix} \quad (6.15)$$

Where s_x , s_y , and s_z are the components of the unit vector to the sun. Abbreviating $\sin \cdot$ as $s \cdot$ and $\cos \cdot$ as $c \cdot$, the derivative of Equation 6.15 with respect to the aircraft attitude is:

$$\begin{bmatrix} \frac{\partial}{\partial \phi} & \frac{\partial}{\partial \theta} & \frac{\partial}{\partial \psi} \end{bmatrix} \cos i = \begin{bmatrix} s_x & s_y & s_z \end{bmatrix} \begin{bmatrix} c\phi s\psi - s\phi s\theta c\psi & c\phi c\theta c\psi & s\phi c\psi - c\phi s\theta s\psi \\ -c\phi c\psi - s\phi s\theta s\psi & c\phi c\theta s\psi & s\phi s\psi - c\phi s\theta c\phi \\ -s\psi c\theta & -c\phi s\theta & 0 \end{bmatrix} \quad (6.16)$$

The measurement variance can be approximated $\sigma_\alpha^2 \approx \frac{\partial \alpha}{\partial \Theta} \Sigma_\Theta$. Equations 6.14 and 6.16 give $\frac{\partial \alpha}{\partial \Theta}$. Assuming that attitude errors are uncorrelated and that $\cos \hat{i} \approx \cos i$, the measurement variance can be written:

$$\sigma_\alpha^2 = \frac{I_{observed}}{I_{clear\ sky} \cos \hat{i}} \begin{bmatrix} \frac{\partial}{\partial \phi} \cos \hat{i} & \frac{\partial}{\partial \theta} \cos \hat{i} & \frac{\partial}{\partial \psi} \cos \hat{i} \end{bmatrix} \begin{bmatrix} \sigma_\phi^2 \\ \sigma_\theta^2 \\ \sigma_\psi^2 \end{bmatrix} \quad (6.17)$$

6.1.5 Sample Noise

The other component of noise is the sample noise. This is variance introduced because a single sample may not be representative of the mean atmospheric state. For instance, the wind vector is influenced by convective motion, terrain interactions, and waves propagating through the atmosphere [10]. The effect of sample variance on solar fraction can be even starker – when flying under scattered clouds the solar insolation “blinks” between sunny and cloudy, never taking its mean value.

6.1.5.1 Wind Sampling Error

The wind sampling error can be analyzed by separating the wind into a mean and turbulent component [10]:

$$u = \bar{u} + u' \quad (6.18)$$

Where by definition the mean of the turbulent component is 0. The degree to which any realization of the wind differs from the mean wind will be described by the statistics of the turbulent component. This then, defines the sampling error and assuming a Gaussian distribution for u' , the variance of the turbulent wind motion gives the desired contribution to the measurement noise.

Within the boundary layer there are scaling laws that can be used to approximate the turbulent wind variance [10]. Turbulence budget equations could also be used to predict the turbulent wind variance [10]. Using scaling laws requires knowledge about other boundary layer parameters however, and solving turbulence budget equations requires running a complex weather model on the aircraft.

From a practical perspective it is simpler to provide the aircraft with a weather forecast which includes a prediction of the turbulent wind variance. One commonly forecast parameter than can be used to approximate the turbulent wind variance is the mean turbulent kinetic energy (TKE) per unit mass of air, defined [10]:

$$\frac{TKE}{m_{air}} = tke = \frac{1}{2} \left(\overline{(u')^2} + \overline{(v')^2} + \overline{(w')^2} \right) \quad (6.19)$$

Where $\overline{(u')^2}$, $\overline{(v')^2}$, and $\overline{(w')^2}$ are the variance of the turbulent east, north, and up wind components respectively. Note that while the TKE per unit mass is often written as e , here a lower case tke is used to distinguish it from the aircraft

energy per unit mass. The u and v components are assumed to have the same statistics [10]. Depending on where the mean and turbulent scale division is drawn, the variance of u' and v' can be significantly larger than w' [100, 101]. When tke is drawn from a weather model it represents the variation in motion that occurs at a scale below the resolved scale of the model. Large eddy simulations and turbulence theory indicates that turbulence at scales shorter than approximately one hundred meters is approximately isotropic [102, 103]. While the scale division for this work is somewhat longer, turbulence is assumed to be near isotropic so that the sampling error for wind components can be approximated:

$$R_{wind, sampling} \approx tke \frac{2}{3} \quad (6.20)$$

If the aircraft is to be operating with no large-scale planning or prior knowledge of the atmospheric environment then a larger value for $R_{wind, sampling}$ should be specified to include the effect of small mesoscale perturbations in the sampling error. This additional sampling error could be approximated by computing the variance of the wind forecast by a numerical weather prediction model over a representative mission, similar to the analysis done by Glasheen et al. [42] In this work, the wind sampling error will be determined solely by tke .

Since the objectives of this work are to make the aircraft robust to error in weather prediction and capable of operating using *in situ* data, the use of a weather model to provide estimates of tke seems slightly self-defeating. Error in the sampling error however, has less effect on the aircraft's flight plan than errors in the atmospheric state. Incorrect specification of the sampling error could lead the Kalman filter to converge too slowly (if the sample error is too large) or provide a state estimate which is noisy (if the sample error is too small) but the state estimate will be unbiased. In contrast, reliance on an *a priori* specified model will almost certainly introduce a systematic error into the aircraft's understanding of the environment, one which cannot be corrected in flight.

6.1.5.2 Solar Sampling Error

Assuming that the clouds are scattered randomly so that a given sample point has a cloud above it with probability f_c , then cloud coverage is defined by a Bernoulli distribution with parameter f_c . The mean cloud coverage is exactly defined by the

cloud fraction, and the variance in cloud cover can be determined from the variance of the Bernoulli distribution [104].

$$\text{Var}(f) = f_c(1 - f_c) \quad (6.21)$$

If all clouds block the same fraction of incident solar energy, α , then sampling error for the solar fraction is easily defined as a simple scaling of the cloud fraction variance:

$$R_{solar, sampling} = \alpha f_c(1 - f_c) \quad (6.22)$$

6.1.5.3 Updraft Sampling Error

The updraft sampling error is the most straightforward to define. Significant updrafts do not occur on scales larger than approximately 1 kilometer except in very unusual circumstances. Turbulent kinetic energy is thus a good scaling factor for estimating the sampling error, so that:

$$R_{updraft, sampling} \approx tke \frac{2}{3} \quad (6.23)$$

In areas of mountain wave, along fronts, or in the vicinity of thunderstorms it is possible to have significant updraft velocities on horizontal scales of tens of kilometers, so that there is a mesoscale component of vertical velocity. These are unusual circumstances and frequently associated with conditions which present a hazard to small UAS flight, so energy optimal response to vertical velocity is not a major concern in these situations.

6.2 Computing Travel Cost

In order to determine the optimal altitude, the aircraft must be able to transform the atmospheric state into a cost. Since the aircraft range or endurance is constrained by its onboard energy store, an appropriate cost is the required power output from storage in order to maintain flight at a specified groundspeed and direction. Because the atmospheric state is known imperfectly, it is desirable to determine both the expected cost and its variance.

For scalar transformations, a simple scaling factor can be determined to compute coefficients of a cost spline from coefficients of the spline describing atmospheric properties. For the updraft velocity the scale factor can be defined:

$$\begin{aligned}\mathbf{j}_w &= T_{j/w} \mathbf{c}_w = -\frac{1}{\eta_{propeller}} \mathbf{c}_w \\ \implies T_{j/w} &= -\frac{1}{\eta_{propeller}}\end{aligned}\tag{6.24}$$

Where \mathbf{c}_w are the coordinates of the updraft profile spline and $T_{j/w}$ is the scalar transformation from updraft to specific energy cost. Since vertical air motion can directly offset aerodynamic power, the transformation is the inverse of the propulsion efficiency. The cost is negative to indicate that an updraft reduces energy consumption.

The solar insolation can be mapped into a cost through a few scaling factors:

$$\begin{aligned}\mathbf{j}_{solar} &= T_{j/solar} \mathbf{c}_{solar} = -\mathbf{c}_{solar} S_{pv} \eta_{pv} I_{clear\ sky} \cos i \\ \implies T_{j/solar} &= -S_{pv} \eta_{pv} I_{clear\ sky} \cos i\end{aligned}\tag{6.25}$$

Where \mathbf{c}_{solar} are the coordinates of the solar fraction spline and $\mathbf{T}_{j/solar}$ is again a transformation matrix. The cost is negative indicating that solar energy input is beneficial.

The effect of wind is the most complicated to include. First, the required airspeed magnitude must be computed from the wind and desired travel direction and speed. The aerodynamic power required must then be computed from airspeed. The airspeed required can be expressed:

$$v(z) = \sqrt{(\bar{v}_n^2 + \bar{v}_e^2) + \mathbf{c}_n^T \mathbf{N}^T(z) \mathbf{N}(z) \mathbf{c}_n + \mathbf{c}_e^T \mathbf{N}^T(z) \mathbf{N}(z) \mathbf{c}_e - 2\mathbf{N}(z)(\mathbf{c}_n \bar{v}_n + \mathbf{c}_e \bar{v}_e)}\tag{6.26}$$

Where \bar{v}_e and \bar{v}_n are the average ground speed required to meet an outer loop goal resolved into east and north components. This already requires a nonlinear transformation. Transforming airspeed into power output introduces yet another:

$$p_{output}(z) = \frac{w_s(v(z))\sqrt{\sigma}}{\eta_{propeller}}\tag{6.27}$$

In order to easily combine the cost due to wind with costs from other sources, a

set of spline coordinates is desired which describes the cost due to the north and east wind profile:

$$p_{output}(z) = N(z)\mathbf{j}_{wind} = \frac{w_s(v(z, \mathbf{c}_n \text{ wind}, \mathbf{c}_e \text{ wind}))\sqrt{\sigma}}{\eta_{propeller}} \quad (6.28)$$

While no general closed-form solution exists, an approximate transformation from wind to cost can be determined. First, Equation 6.28 and Equation 6.26 are combined, this will be generically written as g . The spline basis is evaluated at some altitudes $z_l \in \{z_0, z_1, \dots, z_L\}$ where $L > (n + k - 1)$ so that:

$$\mathbf{N}(\mathbf{z})\mathbf{j}_{wind} = g(\mathbf{z}, \mathbf{c}_n \text{ wind}, \mathbf{c}_e \text{ wind}) \quad (6.29)$$

Which can be solved in the least-square sense to compute wind cost coefficients, \mathbf{j}_{wind} :

$$\mathbf{j}_{wind} = (\mathbf{N}^T(\mathbf{z})\mathbf{N}(\mathbf{z}))^{-1} \mathbf{N}^T(\mathbf{z})g(\mathbf{z}, \mathbf{c}_n \text{ wind}, \mathbf{c}_e \text{ wind}) \quad (6.30)$$

Computation of the covariance of the wind cost coefficients is a little more challenging. In principle, the Jacobian of Equation 6.28 can be found and used to compute a linearized transformation of the covariance. The derivatives are laborious to compute however. If the aerodynamic model, $w_s(v)$, is an empirical model then there may not be analytic derivatives at all. For this reason it is easier to transform the covariance using the unscented transform [105].

Assuming that all costs are able to be expressed as splines using the same knot locations, then the total cost can be determined by simply adding the coordinate vectors together:

$$\begin{aligned} \mathbf{j} &= \mathbf{j}_w + \mathbf{j}_{solar} + \mathbf{j}_{wind} \\ &= T_{j/w}\mathbf{c}_w + T_{j/solar}\mathbf{c}_{solar} + (\mathbf{N}^T(\mathbf{z})\mathbf{N}(\mathbf{z}))^{-1} \mathbf{N}^T(\mathbf{z})g(\mathbf{z}, \mathbf{c}_n \text{ wind}, \mathbf{c}_e \text{ wind}) \end{aligned} \quad (6.31)$$

Where $T_{j/}$ is the linear transformation matrix between the cost and profile coordinates. For the solar and updraft profiles, the transformation matrices can be used to compute their contribution to the covariance of the cost model.

$$\begin{aligned}\mathbf{P}_{j,updraft} &= T_{j/w} \mathbf{P}_w T_{j/w} \\ \mathbf{P}_{j,solar} &= T_{j/solar} \mathbf{P}_{solar} T_{j/solar}\end{aligned}\tag{6.32}$$

Where \mathbf{P}_w is the covariance matrix of the updraft velocity model and \mathbf{P}_{solar} is the covariance matrix of the solar fraction model.

The components of the cost covariance can then be summed to determined a total covariance for the output power model.

$$\mathbf{P}_j = \mathbf{P}_{j,updraft} + \mathbf{P}_{j,updraft} + \mathbf{P}_{j,wind}\tag{6.33}$$

6.3 Flight Test

To test the environmental modeling system it was implemented on the Vulture, a small UAS described in Section 3.4.2. Because it was simplest to obtain wind data to validate the model and because wind dominated variations in the aircraft's energy budget, the test focused on the wind profile. Numerical weather model analyses and radiosondes launched during the test provide validation data.

The test was conducted on 6 December 2018 in central Pennsylvania. The synoptic conditions were in transition, a high pressure system was located to the south-southwest and a weak cold front was approaching. Passage of the cold front was approximately 12 hours after the completion of the flight test. Winds were from the southwest at approximately 7.5 m s^{-1} as depicted in Figure 6.5.

6.3.1 Test Description

The wind profile was sampled by the aircraft once per hour beginning approximately one hour after sunrise and continuing until about one half hour before sunset. Sampling missions were conducted by flying in a circle with a radius of 150 meters. The mission began at an altitude of 439 meters above sea level, about 30 meters above ground level. The aircraft climbed at 1.5 m s^{-1} to an altitude of 674 meters MSL, about 270 meters above ground, then descended at approximately 0.75 m s^{-1} (the aircraft's descent rate in a glide) until reaching the start altitude. Figure 6.6 shows the flight area and nominal aircraft orbit, Figure 6.7 illustrates the aircraft altitude during the course of the test.

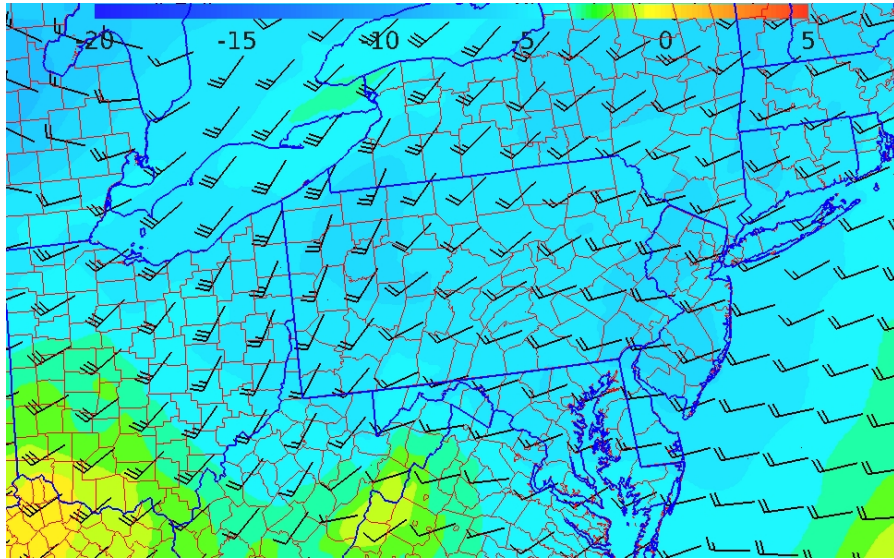


Figure 6.5: Wind and temperature at 925 mbar (approximately 750 m MSL) at 17:00 UTC, approximately the midpoint of the test. The approaching front can be seen as a abrupt wind shift along the eastern border of Michigan.

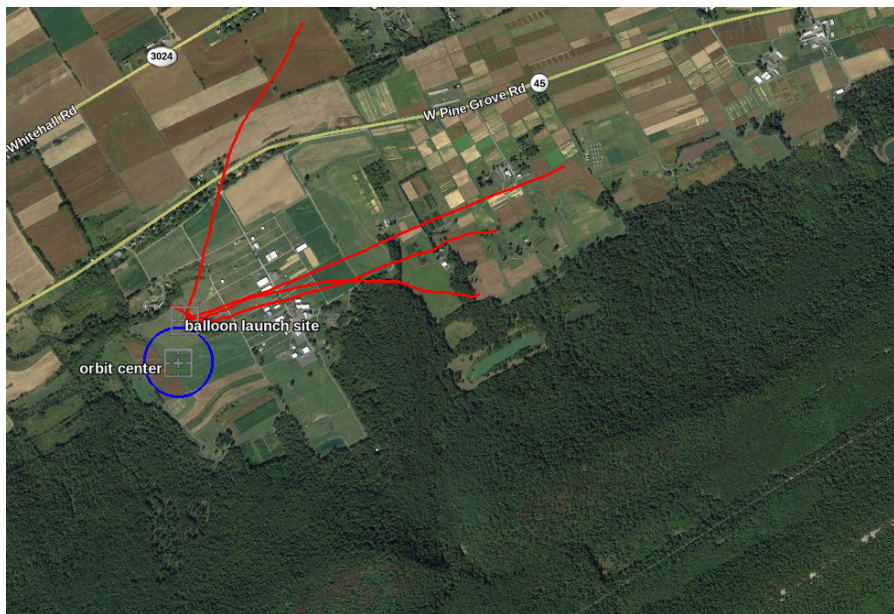


Figure 6.6: Aerial view of the test area showing the balloon trajectories and aircraft orbit location.

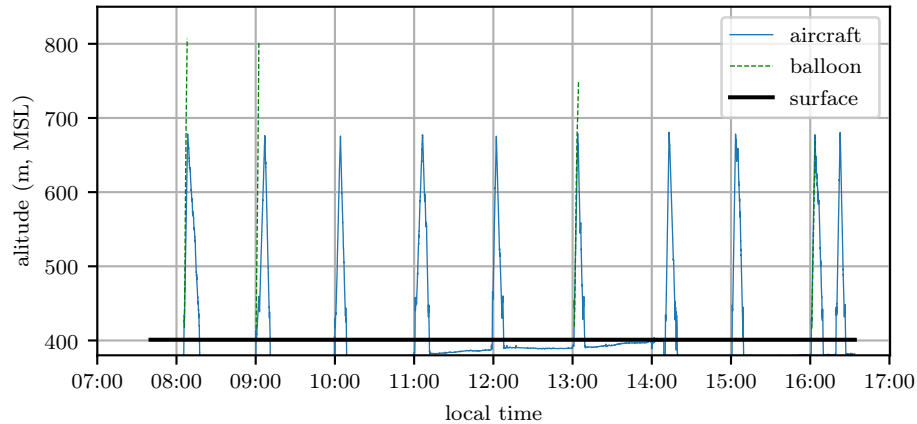


Figure 6.7: Time history of aircraft and balloon altitude. The aircraft appears to be below ground between flights because its state estimator is incorporating airspeed measurements which are not informative when on the ground. Balloon launches occur at 08:00, 09:00, 13:00, and 16:00 local time.

Several times throughout the day a Sparv Embedded S1 Windsonde was launched on a balloon from a site approximately 200 meters north of the orbit point. A GPS sensor on the radiosonde provided drift information which was used to determine wind speed, data was telemetered to the ground at 1 Hz. The radiosonde ascent was terminated by cutting the radiosonde free from the balloon after reaching 680 meters, permitting the radiosonde to be retrieved and reused. Balloon profiles were taken concurrently with the aircraft profiles at 08:00, 09:00, 13:00, and 16:00 local time.

The wind profile modeling system was enabled throughout the entire test so that the model mean and covariance was propagated in between profiling flights. The time derivative of the wind profiles was obtained by numerically differentiating the 09:00 UTC (04:00 local) HRRR forecast. When the aircraft’s airspeed was less than 10 m s^{-1} measurement updates were disabled to prevent nonsensical wind measurements from being incorporated while the aircraft was on the ground.

6.3.2 Process and Measurement Noise

At each measurement step a “wind measurement” is synthesized by solving the wind triangle given inertial speed and airspeed [99]. The wind sensor noise is computed at each step from the wind measurement dynamics and the measurement noise of

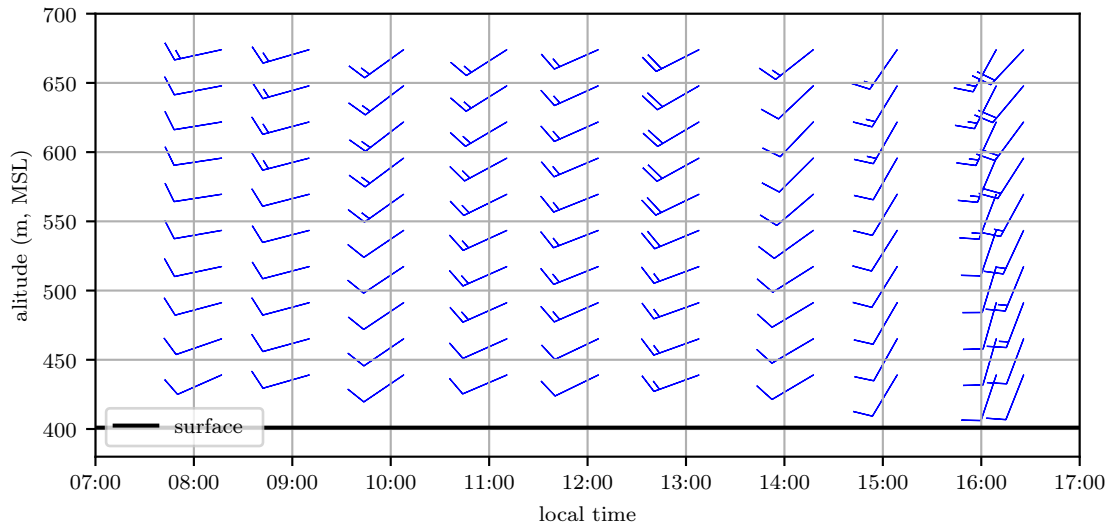


Figure 6.8: Time-altitude depiction of the profile of aircraft estimated horizontal wind depicting its evolution throughout the day.

the sensors used in computing the “wind measurement” [99].

Averaged over 900 HRRR runs, the 1 hour forecast error variance at the model grid point nearest the flight location is $0.95 \text{ m}^2 \text{ s}^{-2}$. The wind process noise is set so that the spline model state variance increases by this amount after one hour of time updates.

6.3.3 Results

Ten profiling flights were conducted by the aircraft, covering a time period of 8.5 hours. The estimated wind profiles can be compared to those gathered by weather balloons and the analysis values from the HRRR. While the wind profiling system was running on the aircraft throughout the entire day, an error in the system was discovered after the test. The results shown here were generated by running the raw aircraft sensor data through a corrected profile model in real-time as if it was being flown on the aircraft again. Figure 6.8 illustrates the evolution of the estimated wind profile throughout the day.

The wind profile initially shows increasing wind, likely a result of the deepening boundary layer drawing in momentum from the free troposphere above. Around 14:00 local time the wind magnitude decreases before the wind turns more southerly

and increases in speed as the cold front approaches [59].

6.3.3.1 Comparison with Radiosonde Observations

Coincident with the beginning of the aircraft profiles at 08:00, 09:00, 13:00 and 16:00 local time a balloon carrying a radiosonde was launched. Comparisons between the radiosonde and aircraft measured winds can be used to determine that the aircraft is a reliable instrument for sampling the wind field [106,107]. The balloons were launched about 200 meters from the orbit center point and drifted to the northeast, sometimes a kilometer or more before completing their profile. As the balloons ascended the radiosondes were observed swinging on their tethers, this motion sometimes interrupted GPS lock so the recorded data was quality controlled before analysis. Data points where the GPS lock or wind velocity was flagged as invalid were removed.

To simplify comparison to the aircraft measured profiles a basis spline with the same knot locations and order was fit to the radiosonde measurements. Detailed sensor specifications were not available for the radiosonde and the motion of the radiosonde introduces an additional error (i.e. the sensor package swinging on its tether beneath the balloon), making definition of the measurement variance difficult. The sample variance was estimated from variance of the error between radiosonde wind samples and the mean wind profile estimated for each launch.

Because the balloon advects with the the mean wind speed, it violates Taylor's simplification for analyzing turbulent wind fields [10]. For the balloon, turbulent eddies do not appear as measurement noise, but as a bias on the entire profile. Reflecting this, the balloon wind variance is increased by the $\frac{2}{3}tke$.

Figures 6.9-6.12 compare the aircraft filtered and radiosonde measured profiles at four times in the day. In each figure the mean profile and 1σ bounds are depicted for both the aircraft and radiosonde. Error bounds on the aircraft's profile are determined by the filtering algorithm. Note that these bounds do not reflect the variance of the wind observations, rather they reflect the variance in the mean profile. The observations are not expected fall within the 1σ bounds 37% of the time, rather the mean profile will lie within the error bounds 37% of the time. The bounds are illustrated as an evaluation of the likelihood that the two techniques reflect observations of the same process, and implicitly that the process and measurement noise for the Kalman Filter modeled profile is correct.

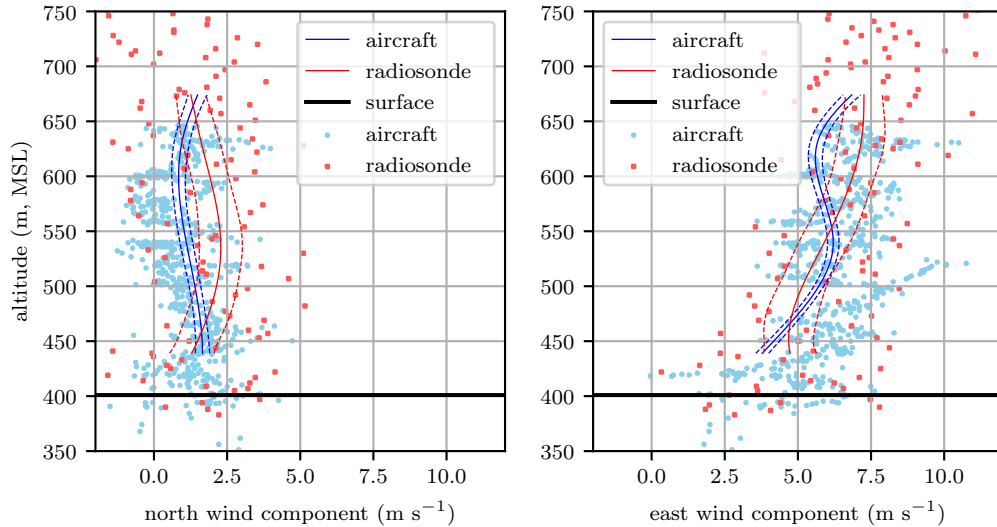


Figure 6.9: Aircraft and radiosonde profiles from 08:00 local time.

Figure 6.9 shows that the mean profiles measured by the radiosonde and aircraft agree well, generally within their mutual 1σ error bounds. The raw radiosonde data are conspicuously sparse. As the balloon rises at approximately 3 m s^{-1} , the radiosondes provide data at 1 Hz so they only take about 100 samples before rising above the test area. Conditionally sampling for valid GPS lock reduces this data set by about 15%. The aircraft samples in contrast are taken at approximately 10 Hz and include the descending leg of the sampling mission

Figure 6.10 compares radiosonde and aircraft measured profiles at 09:00 local time. Good agreement between the two is seen at altitudes above 450 meters (80 meters above ground).

Figure 6.11 shows good agreement between the radiosonde and aircraft profiles throughout most of the profile.

Figure 6.12 shows an unusual arched pattern in the radiosonde data, particularly in the north wind component. This late in the day, approximately 1 hour before sunset, the buoyantly generated *tke* is diminishing (as seen in the closer error profiles for the radiosonde) [10]. This perturbation is likely the result of the balloon advecting along with a particularly large eddy. Similar magnitude perturbations can be seen in the raw aircraft observations in Figures 6.11 and 6.12. The aircraft can fly out of the eddy however, and the eddy is advected away from the flight area

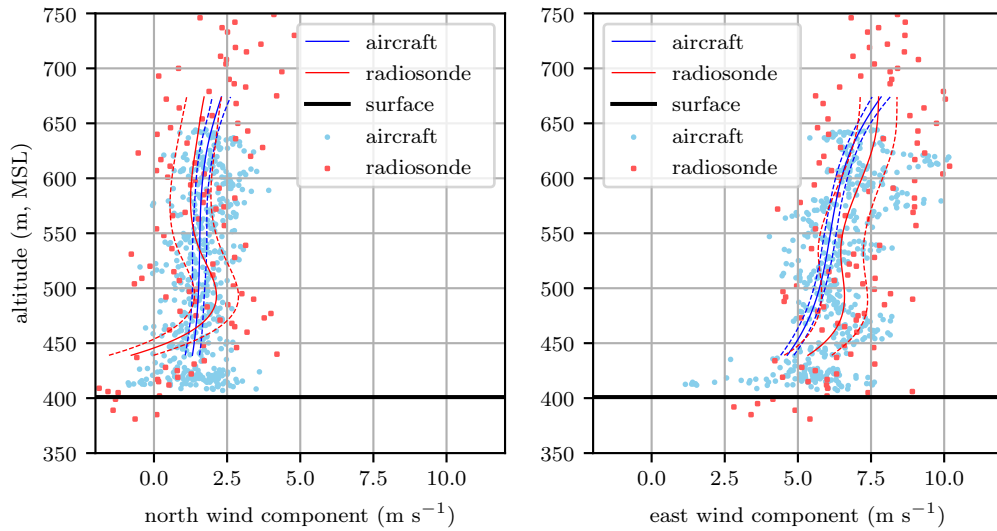


Figure 6.10: Aircraft and radiosonde profiles from 09:00 local time.

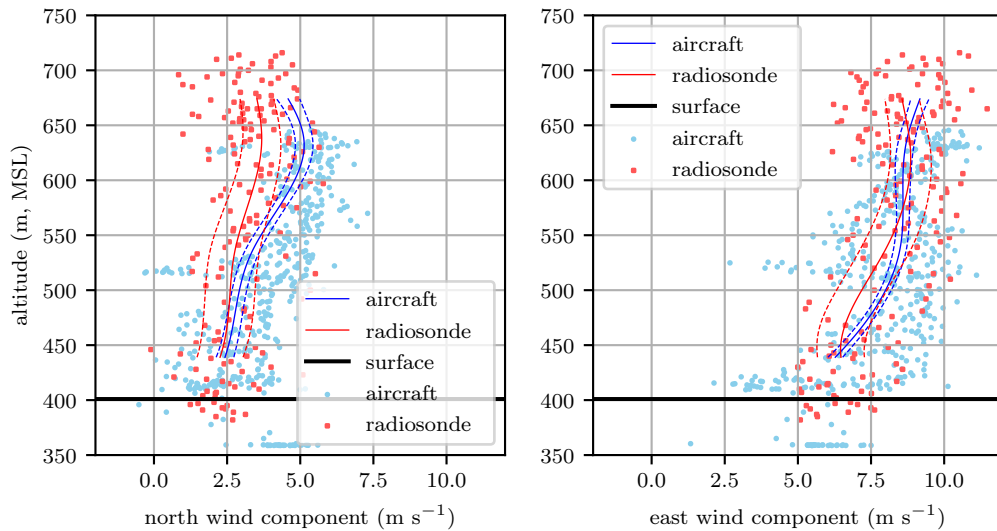


Figure 6.11: Aircraft and radiosonde profiles from 13:00 local time.

by the mean wind while the balloon drifts with these perturbations.

Nominally, this should be reflected by the magnitude of tke , but there is a source of turbulence that is not fully captured by the HRRR. A mountain ridge approximately 250 meters tall is located about 1 kilometer south and west of the test site, the ridge can be seen in Figure 6.6 running from southwest to northeast.

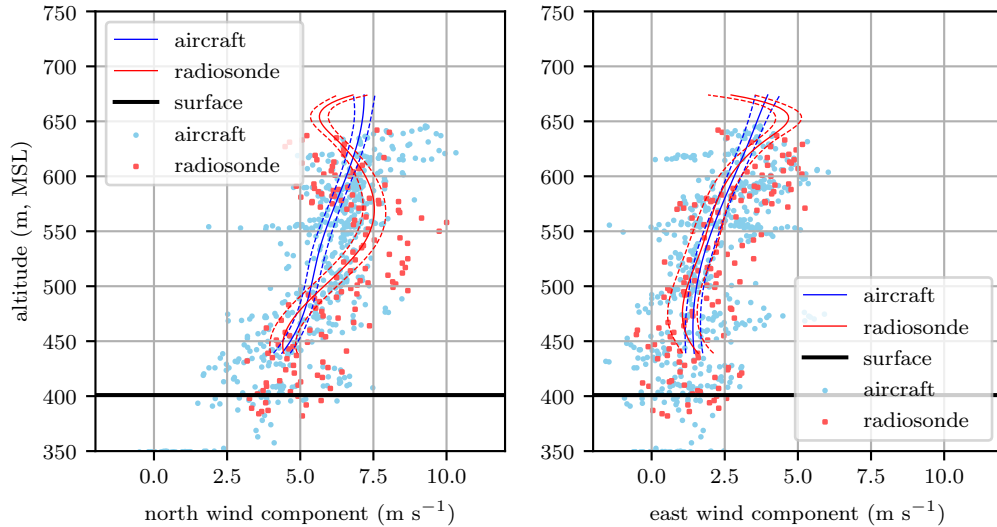


Figure 6.12: Aircraft and radiosonde profiles from 16:00 local time.

As winds shifted around to the south, there would be a significant cross-mountain component resulting in shear-generated turbulent eddies shed off of the mountain. The scale of this mountain system is of the same order as the grid resolution of the HRRR forecast model, so the effects of the mountains on the mean wind profile and tke is not fully resolved.

6.3.3.2 Comparison with Numerical Weather Model

The aircraft profiles were begun approximately on each hour to permit easy comparison with hourly weather model analyses, with the exception of the final profile which was constrained by the sunset time as regulation prohibits UAS flights after sunset. Figures 6.13-6.16 compare the evolution of the aircraft and HRRR wind profiles at the hours nearest radiosonde observations. The 1σ bounds are depicted on both the aircraft and HRRR profiles.

It is worth noting here that the comparisons are made against the HRRR analyses obtained post-flight. The HRRR profiles then are not forecasts, but the best estimate of the atmospheric state that can be made by the model. Using analysis data in flight would require considerable processing power on the ground be dedicated to providing very frequent analyses, and a constant high bandwidth link to the aircraft to update its data. This comparison then, represents the best-case for

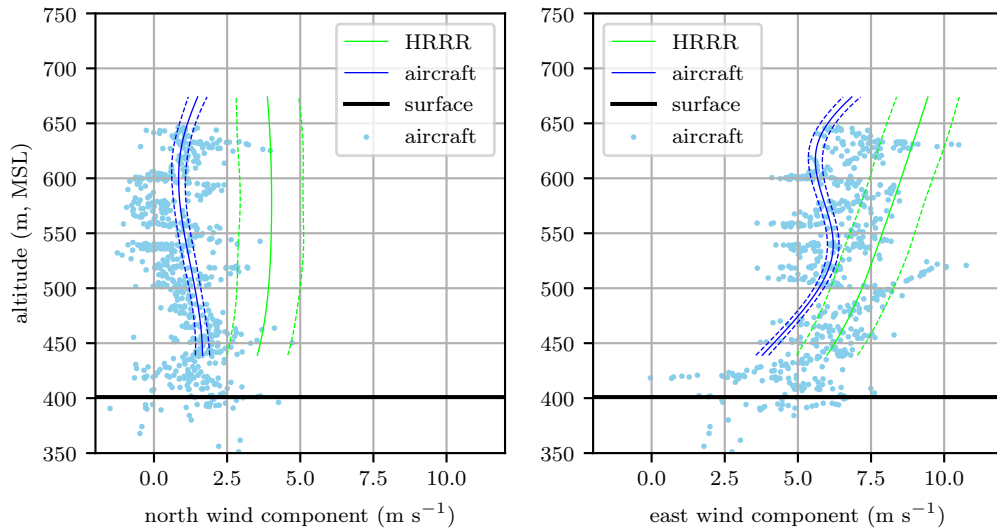


Figure 6.13: Aircraft measured and HRRR predicted wind profiles at 08:00 local time.

using offboard numerical weather prediction, less frequent updates from a forecast would perform worse.

The HRRR model error cannot be readily assessed from either a single model output or a series of model runs. It is necessary to know the model’s analysis skill, the average error between the expected conditions and those observed. Benjamin et al. and Pichugina et al. indicate that the HRRR wind analysis skill is approximately 2.5 m s^{-1} [87, 88].

Figure 6.13 compares the aircraft measured profile after the 08:00 flight with the HRRR analysis at that time. The profiles show similar shapes but the HRRR profiles are $2 - 3 \text{ m s}^{-1}$ greater in both components. The undulation in the aircraft modeled east wind component observed by the aircraft between 500 and 600 meters is likely the result of an eddy generated by either buoyantly rising air parcels or by the influence of surrounding terrain.

The effect of small eddies appear as random noise in the aircraft observed winds and are accounted for by increasing the measurement noise by the $\frac{2}{3}tke$. In order for this noise to be random and uncorrelated however, the aircraft must be traversing the wind field fast enough that the measurements are not correlated. The largest turbulent eddies in the boundary layer have a characteristic scale of roughly 1 kilometer [108]. An aircraft which is circling in the same location is traversing

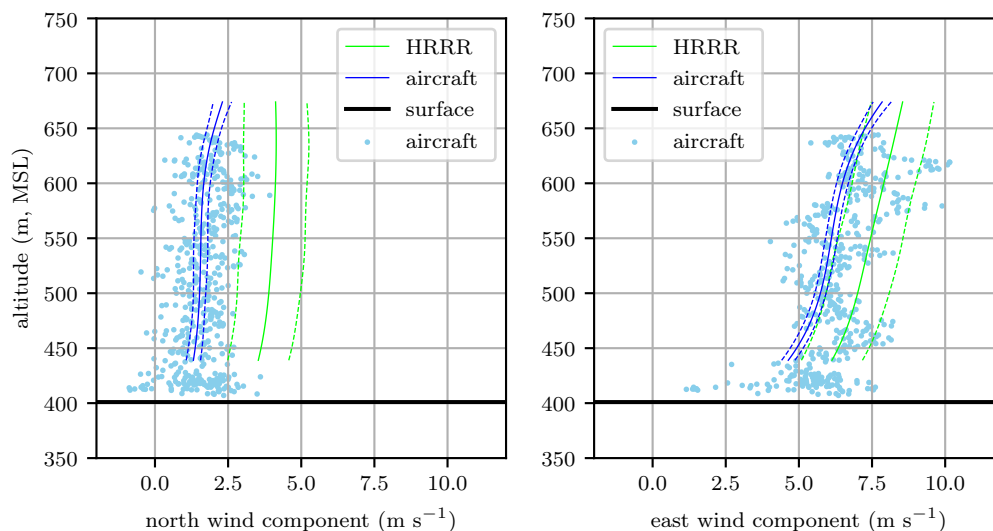


Figure 6.14: Aircraft measured and HRRR predicted wind profiles at 09:00 local time.

the wind field on average at the wind speed. Given the wind magnitude during this test, measurements could be correlated for up to two minutes, so some of the eddies can appear as biases in the estimated wind field rather than noise, as seen in Figure 6.13. Aircraft traveling to a destination will traverse the wind field much faster, so sample to sample correlation is decreased and these perturbations should be eliminated. Alternatively, Bryson and Henrikson’s approach to estimation with correlated measurement noise could be applied, preventing the bias but increasing the measurement variance.

Figure 6.14 clearly demonstrates the need to incorporate *in situ* information for flight planning. The HRRR and aircraft measured profiles agree well on shape, but the HRRR over predicts both wind components by approximately its analysis skill. At an altitude of 500 meters, HRRR anticipated wind magnitude is about 2 m s^{-1} greater than the measured profile, more than 10% of the aircraft’s nominal cruise speed.

Figure 6.15 again shows the limitations of relying solely on numerical weather prediction models for understanding the aircraft’s environment. The east wind component shows the HRRR to be in error by $2\text{-}3 \text{ m s}^{-1}$, but this time *under predicting* the wind magnitude. This demonstrates that even if some validation data is available to develop a correction to the output of a numerical weather

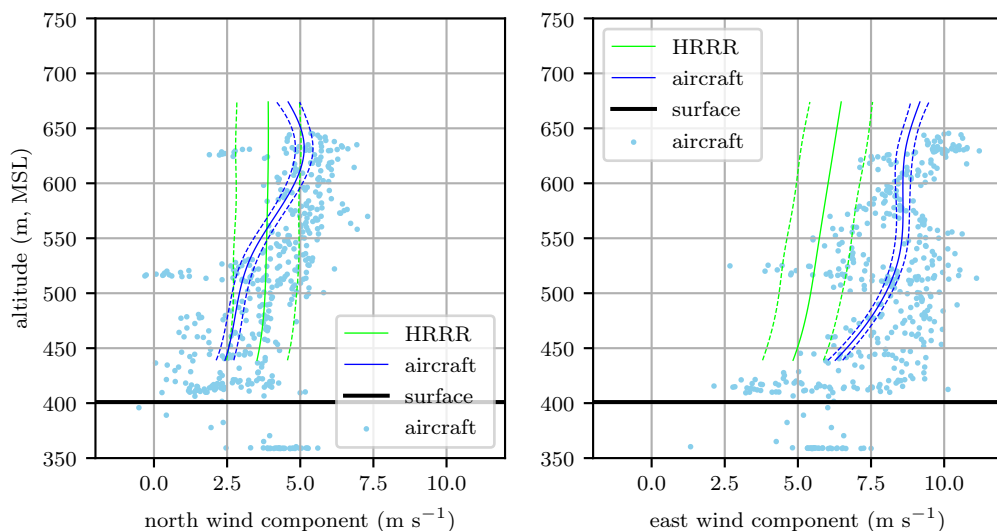


Figure 6.15: Aircraft measured and HRRR predicted wind profiles at 13:00 local time.

prediction system, it must be fairly available fairly frequently and at high resolution. In practice, it is simpler to estimate the atmospheric state onboard the aircraft.

Figure 6.16 shows the wind profile at 16:00 local, the second-to-last aircraft observed profile and last profile sampled on a hour. The wind is more southerly than anticipated by the HRRR, indicating that the prefrontal southerly winds are developing sooner than expected.

6.3.4 Travel Cost

While knowledge of the atmospheric structure may be useful in itself, the objective here is for the aircraft to have knowledge of the cost to travel to a desired location. The transformations developed in Section 6.2 can be applied to the profiles expected by the HRRR, measured by the balloon, and constructed *in situ* by the aircraft to determine the cost to accomplish a mission.

Figure 6.17 shows the cost, expressed as specific power, and its 1σ bounds for the vulture to travel in any direction at a groundspeed of 15 m s^{-1} at 13:00 local time. Two altitudes are displayed, 500 and 650 meters MSL. The figure illustrates how using only *a priori* information can lead to poor decisions. If the aircraft is traveling south-southeast the HRRR profiles expect the cost to be similar at both

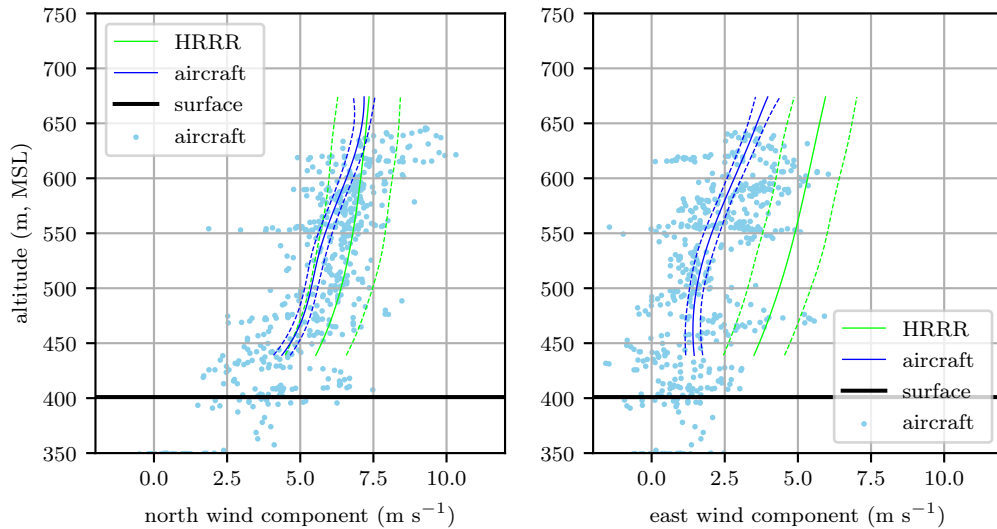


Figure 6.16: Aircraft measured and HRRR predicted wind profiles at 16:00 local time.

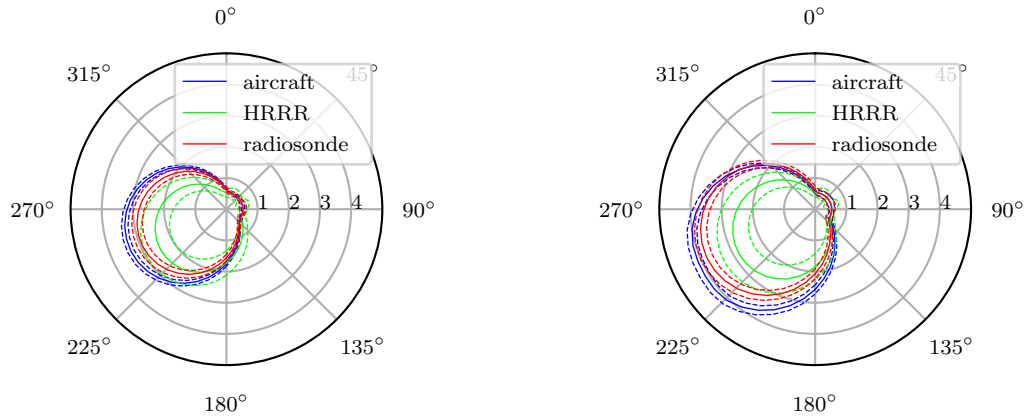
altitudes, so it may be desirable to fly aircraft higher in order to improve sensor coverage. The profile determined by the aircraft shows a different picture – the cost of traveling at 650 meters is approximately 1 m s^{-1} greater, or a 30% increase in energy consumption.

6.4 Summary

Basis splines provide a nonparametric way to model the atmospheric environment in a computationally efficient way. Since they are linear models, they can easily be implemented in a Kalman Filter, allowing simple and efficient updates to the model. This also permits observations and entire profiles to be combined if information is available from multiple sources.

To accurately determine the covariance of the mean atmospheric structure, filter noise must include more than just the sensor characteristics. This additional error captures the sample variation from the mean state due to random fluctuations in the atmospheric state. The sample variance can be estimated from scaling laws or from the output of numerical weather prediction models.

Modeling the environment using basis splines permits the atmospheric state to be easily transformed into a cost for use in flight planning. The use of a Kalman



(a) Cost for the vulture to travel at an altitude of 500 meters above sea level. (b) Cost for the vulture to travel at an altitude of 650 meters above sea level.

Figure 6.17: Cost for the vulture to travel in any direction at an average groundspeed of 15 m s^{-1} . Cost is expressed in specific power and evaluated at 13:00 local time.

Filter to model the environment allows the environmental state covariance and thus cost covariance to be determined. The Kalman Filter also permits fusing weather forecasts with *in situ* observations from the aircraft, a distributed flock of aircraft, or remote sensing systems. For linear transformations between atmospheric properties and cost, the cost profile and covariance is easily determined. Nonlinear transformations pose some additional difficulty but the mean and covariance of the cost can be approximated using best-fit and nonlinear covariance transformation techniques.

The wind profile filter was implemented on a small UAS and ten wind profile sampling missions conducted over the course of a day to track the evolution of the wind profile. The estimated wind profile is compared to numerical weather model analyses and to observations made with balloon-borne radiosondes. The aircraft-estimated and radiosonde observed profiles generally agree up to their respective model covariances. The analysis profiles show greater deviation, frequently exceeding even the analyses' greater profile variance.

Propagating the wind model obtained by the aircraft through a cost function allows the aircraft to determine the mean cost to travel in a desired direction and the confidence in that cost. This improves the aircraft's situational awareness and can enable a human operator or automated scheduler to weigh the cost of an action.

In one example from the flight test, the onboard modeling system identifies a 30% difference in cost over only 150 meters of altitude change, a change in cost which is not anticipated *a priori* by the numerical weather prediction model.

Fusing *a priori* information available from numerical weather prediction models with observations made *in situ* by an aircraft provides a method to improve the quality of atmospheric state information available to the aircraft without requiring significant ground computation resources or constant communications links to the aircraft.

Chapter 7 | Altitude Optimization

Section 5 demonstrated that power output can be scheduled separately from the velocity command without affecting the optimal velocity or power schedule. The only constraint provided was that the power output from the aircraft's onboard storage must supply whatever portion of the energy budget is not harvested from the environment. Since the velocity varies in response to the stochastic component of the environment, it makes sense to use the power output to respond to the mean atmospheric state.

Section 6 developed a means to model the mean atmospheric state and its impact on the aircraft's energy budget. To complete an operational system, a method is needed to employ this model in a way that minimizes energy consumption. Since a profile of travel cost can be computed from the profile of the atmospheric state, the altitude with minimum expected energy can be found directly from this profile. Computing the derivative of a basis spline is straightforward [95] so the extrema of the cost profile can be easily determined.

This greedy approach is risky however; since the environmental model is uncertain, the altitude with the lowest expected value may not truly be best. If the only source of information about the atmospheric state comes from the aircraft's own *in situ* observations then this problem only worsens with time as the model uncertainty grows everywhere but where the aircraft is flying. All of this is compounded further since the environment is not stationary. The optimal altitude can change with time and even if a prediction of the evolution of the environmental state is available, uncertainty in the model evolution degrades confidence that the greedily chosen altitude is best.

Figure 7.1 schematically shows the problem: the aircraft must make a series of decisions about altitudes to visit in order to minimize its energy expenditure. In

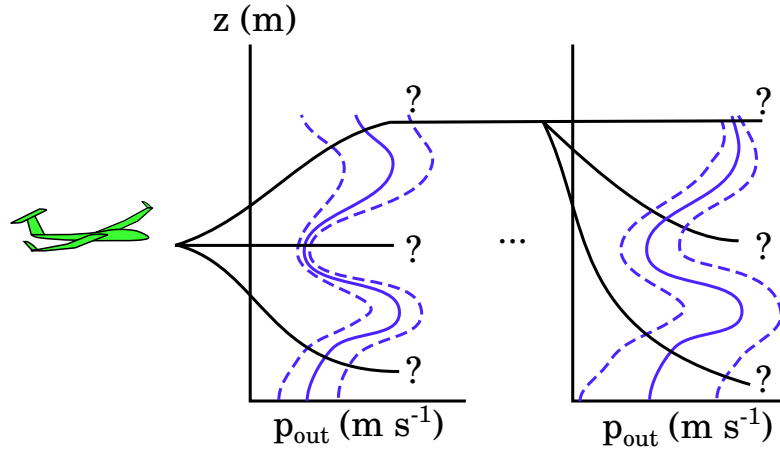


Figure 7.1: In order to choose the altitude with the smallest travel cost, the aircraft must decide when to visit possibly suboptimal altitudes in order to gain information about its environment.

order to know the best altitude to fly at, the aircraft must periodically visit possible suboptimal altitudes in order to gather information about the environment.

Section 2.3 discusses several approaches to balancing exploration and exploitation. The most directly applicable problem format is the multi-armed bandit. The problem addressed in this thesis is a particularly challenging form of a bandit problem. The search space is a continuum, the reward distribution is nonstationary, and the number of “pulls” is relatively small, giving little time for exploration. These problems are often examined singly in the bandit literature but not together, this section develops a pricing approach that uses a probabilistic model of the environment to identify regions that should be explored based on their likelihood of having low travel costs.

To clarify discussion throughout this section a few definitions need to be made. The energetic cost (specific power output from storage) for the aircraft to achieve a desired inertial velocity (specified by an operator or outer-loop planner) is referred to as the “travel cost.” The energy required to change altitude is the “transition energy” while the net energy required to gather information then return to the initial altitude is referred to as the “investigation energy.” Finally, the energetic cost of changing altitudes to gather information, then continuing travel (with no restriction on the altitude for subsequent travel) is termed the “exploration cost.”

The use of “energy” rather than cost for some terms is to make clear that they have units of energy where the “costs” have units of energy rate. Specific power

is the objective function here because in a nonstationary environment without knowledge of the future evolution of the atmospheric state, the aircraft cannot compute an integral cost (such as total expended energy). It must rely instead on consistent minimization of the instantaneous derivative of the stored energy.

7.1 Travel Cost

Section 6.3.4 describes how to transform a model of the atmospheric state into a profile of the cost to travel at a specified inertial velocity. A naive approach to altitude selection would be to choose the altitude which has the minimum expected travel cost.

This strategy carries risk, especially when the cost profile is uncertain. The aircraft might expend energy, changing altitude only to find that traveling at the new altitude is more costly than where it was initially. This is especially a risk if the aircraft makes a significant altitude change to reach a region with low certainty. Upon arriving at a new altitude and finding it not as favorable as expected the aircraft faces a choice – expend additional energy to investigate a new altitude or continue with the higher travel cost.

Using a model which provides estimates of the confidence in the profile helps resolve this problem. A low-cost high-confidence region is certainly worth pursuing while a low-cost, low-confidence region may not be. The converse – a high-cost, low-confidence region may be worth exploring to see if conditions have changed reducing its cost. Heuristics weights have frequently been used to assist in making this tradeoff [39, 109]. These weights significantly affect the performance of the guidance system, so selecting them is a significant design choice. In practice there is often considerable “tuning” of the weights which must be done in order to achieve good performance, this process is difficult to scale to large numbers of systems and does not work well if the aircraft is operating in a new environment.

Assuming that the time required to transition to a new region is small so that the only relevant travel costs are at the initial and final altitudes, the maximum change in energy required to visit a region is the difference between the current and candidate altitude. If a period over which this energy change is averaged can be defined then the transition energy (specific energy) and travel cost (specific energy rate) can be combined to define the exploration cost:

$$j_{exploration} = j_{travel} + \frac{e_{transition}}{T_{payback}} \quad (7.1)$$

If the cost profile is represented by the spline model developed in Section 6 then the profile of exploration cost including transition energy and travel cost can then be computed:

$$\mathbf{c}_{j,exploration} = \mathbf{c}_j + \frac{\mathbf{c}_{\Delta h}}{\eta_{propeller} T_{payback}} \quad (7.2)$$

Where \mathbf{j} is the spline coordinates of the travel cost profile determined in equation 6.31, $T_{payback}$ is the payback period, and $\mathbf{c}_{\Delta h}$ is a vector of spline coefficients representing the difference between the current and candidate altitudes. The expression $\frac{\Delta h}{\eta_{propeller} T_{payback}}$ represents the cost of transition, or the degree to which a candidate altitude must be superior to the current altitude in order to be worth changing.

Note that the transition energy could be made more detailed if a better estimate is available. The model structure in Equation 7.1 admits any form for the transition energy provided it can be represented in the same model form as the travel cost. If the spline model is adopted, then uncertainty in the transition energy could be included in the exploration cost profile as well:

$$\mathbf{P}_{exploration} = \mathbf{P}_{travel} + \mathbf{P}_{transition} \quad (7.3)$$

In this formulation the payback period, $T_{payback}$ determines the amount of time which is allotted to recoup the cost of changing altitude by flying in a more favorable region. A natural value for $T_{payback}$ would be a time scale based on either mission duration or how quickly information degrades as this limits how long a favorable region can be exploited. Shorter values for $T_{payback}$ tend to discourage exploration – a candidate altitude must be very favorable in order to pay back the transition cost in time, large values promote changes to exploit even small differences. In the extreme case as $T_{payback} \rightarrow \infty$ the transition cost is ignored. Note also that as $T_{payback} \rightarrow 0$ that altitudes below the aircraft are preferred as gliding down to these altitudes enables a small power output. This effect will be explored more later.

In the absence of a mission duration, $T_{payback}$ could be selected from the shape of the atmospheric energy spectrum. Energy input to the atmosphere occurs largely

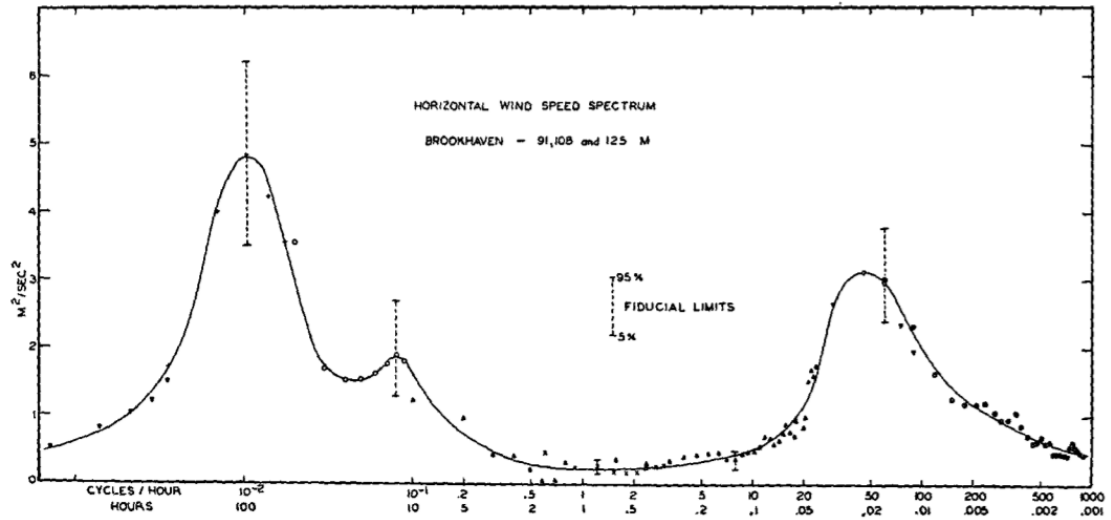


Figure 7.2: The spectrum of atmospheric energy has long-term (diurnal and weekly) and short-term (minutes) peaks. At intermediate scales there is relatively little energy, so observations of departures from forecast conditions are valid for several hours. Reproduced from Van der Hoven (1957) “Power Spectrum of Horizontal Wind Speed in the Frequency Range from 0.0007 to 900 Cycles per Hour” [108].

on the small scales (convective turbulence) and large scales (synoptic weather systems) [108, 110], depicted in Figure 7.2. At intermediate scales, around 1 hour, there is comparatively little variation in atmospheric conditions. Note that the relatively small atmospheric variability on this timescale does not mean that it is well forecast. In fact, forecasts shorter than three hours are *less skillful* than forecasts between 3 and 30 hours due to position and timing errors [11]. This makes the low-frequency end of the spectral gap a natural payback period in the absence of other information.

Indeed, the existence of this spectral gap is at the heart of the *in situ* planner – error between the forecast and realized conditions should be correlated over this scale, which is of a similar order to the mission duration of small UAS. Over larger scales *in situ* observations are less informative and *a priori* planner using forecasts can provide quality guidance. At smaller scales a more reactive approach (such as that described in Section 5) is required because perturbations decorrelate very rapidly. Within this gap conditions are consistent enough that *in situ* observations have validity for a long enough time frame to permit the aircraft to respond but error in the forecast conditions can make *a priori* flight plans suboptimal.

7.2 Mission Constraints

Mission constraints and operational objectives may put limits on the desired altitude of the aircraft. Sometimes these restrictions may not be “hard,” that is the mission performance measure which motivates a constraint smoothly degrades as the aircraft departs from some nominal altitude. For example, imaging resolution smoothly decreases as altitude increases so a hard altitude limit might not be an appropriate constraint provided a reduction in resolution can be tolerated in exchange for greater range or endurance.

This system can provide an estimate of the cost to comply with a mission constraint. The difference between the expected travel cost at the desired altitude and the cost at the constraint limit provides information about the effect of the constraint. For “soft” constraints, if a cost tolerance can be defined to represent the additional specific power which can be tolerated in order to improve mission performance, then it can be included naturally by addition to Equation 7.2. In some cases this may be simple to define – a mapping task that is not resolution limited can survey more area by flying higher and the speed required to survey the same area per unit time can be defined:

$$v_2 = \frac{\delta_1 v_1}{\delta_2} \quad (7.4)$$

Where δ_1 is the camera field of view projected onto the ground at the nominal altitude (the scan width in meters), v_1 is the nominal speed, δ_2 is the camera field of view at a candidate altitude, and v_2 is the speed required to survey the same area per unit time at the candidate altitude. The speed change can be related to a cost via the method described in Section 6.2 to build a profile of the energetic cost of achieving a specified utility. This cost could then be included in Equation 7.1.

Even if a hard constraint is specified the travel cost profile is valuable as it can define to an operator or supervisory system the energetic cost of compliance with the mission constraint. This can be used to help determine if the mission constraint is really warranted or if the aircraft has enough energy to complete the mission.

An alternate approach can be taken if the aircraft’s primary mission is to reach a desired location but it has a secondary mission to perform along the way and an energy budget for performing this mission. The travel cost profile can be used

to determine the acceptable departure from the optimal altitude which can be tolerated while satisfying this budget.

7.3 Selecting an Altitude to Explore

7.3.1 Expected Cost of Exploration

The estimate of exploration costs is based on a transformation of the distribution of the environmental properties. The proposed model structure produces a Gaussian distribution of the environmental state and thus exploration cost distribution. This means that even an altitude expected to be favorable has a tail admitting unfavorable conditions and vice-versa.

If the aircraft explores an altitude and finds it unfavorable then it can return to its previous altitude. The aircraft will have high confidence in the conditions at the initial altitude and the spectral structure of the atmosphere means that information about the initial altitude will remain relevant provided that the exploration is relatively fast. A large transition might cover 1000 meters of altitude, and vertical rates of 1.0 m s^{-1} are common for small UAS so only half an hour would be required to explore and return to the initial altitude, considerably faster than the large-scale period of the atmosphere.

Assuming that the transition to a candidate altitude and back to the initial altitude happen rapidly then there is no net cost to investigating a candidate altitude (the energy expended climbing is recovered when gliding). The maximum cost incurred by investigating an altitude and then either continuing at that altitude or returning to the initial altitude is thus the initial travel cost plus an investigation cost.

$$j_{limit}(z) = j_{exploration}(z_{initial}) + \frac{e_{investigation}(z, z_{initial})}{T_{payback}} = j(z_{initial}) \quad (7.5)$$

In this work, the investigation cost will be assumed to be zero, that is the aircraft recovers all the energy spent climbing in a glide (or expends energy saved in a glide down to an exploration altitude climbing back to its start point). If an investigation energy can be defined then it can easily be included in the cost limit.

Since there is a limit to the cost incurred by selecting a candidate altitude Equation 7.2 is not enough to evaluate the expected exploration cost by itself. For each altitude under consideration the full probability distribution $p(j(z))$ is required. The portion of the distribution with cost greater than j_{limit} can be reassigned to the cost limit, so the expected exploration cost can be computed:

$$\begin{aligned} \mathbb{E}(j_{exploration}(z)) = & \int_{-\infty}^{j_{limit}} j_{exploration}(z)p(j_{exploration}(z))dj(z) \\ & + j_{limit} \int_{j_{limit}}^{\infty} p(j_{exploration}(z))dj(z) \end{aligned} \quad (7.6)$$

Since the cost of exploring a region is capped by the travel cost at the initial altitude, the distribution of exploration cost is heavily skewed. If information about an altitude has sufficiently degraded then it is possible for the expected exploration cost to be less than the travel cost at the initial altitude, even if the mean travel cost at the candidate altitude is greater than the mean travel cost at the initial altitude.

This is illustrated in figure 7.3 for an initial travel cost of 0.75 m s^{-1} , cost at the candidate altitude described by $\mathcal{N}(1.25 \text{ m s}^{-1}, 1.0 \text{ m}^2 \text{ s}^{-2})$, altitude difference ($z - z_{initial}$) of -750 meters, and payback time of one hour. The cost limit is depicted as a Dirac delta function with length equal to the cumulative probability of exceeding the limit.

While the resulting pdf is clearly non Gaussian, a semi-analytic solution for the expected value is possible. For costs less than the j_{limit} , the distribution is a truncated Gaussian which can be evaluated analytically (up to the error function). The probability of realizing the limit cost is equal to the area under the truncated Gaussian to the right of the maximum cost. With this knowledge, a piecewise integration to obtain the expected value is possible.

This provides an explicit way to evaluate altitudes that is almost free from hyperparameters. The only value which must be chosen in designing the system is the time period over which the transition cost is discounted. Principled ways to choose $T_{payback}$ are discussed in Section 7.1. This also provides an implicit value for information: the difference between the expected value of the unrestricted and the limited distribution of $j_{exploration}$.

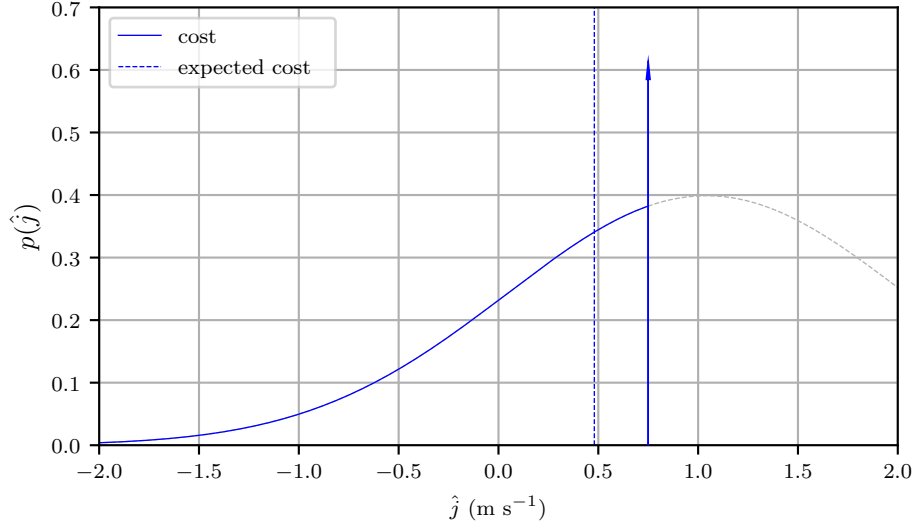


Figure 7.3: Because the aircraft can return to the initial altitude, the distribution of the cost to explore a new altitude is heavily skewed and the expected cost of exploration can be below the travel cost at the initial altitude.

$$\begin{aligned}
 \dot{J}_{information} = & \\
 & \dot{J}_{limit} \int_{\dot{J}_{limit}}^{\infty} p(\dot{J}_{exploration}(z)) d\dot{J}(z) \\
 & - \int_{\dot{J}_{limit}}^{\infty} \dot{J}_{exploration}(z) p(\dot{J}_{exploration}(z)) d\dot{J}(z)
 \end{aligned} \tag{7.7}$$

Note that the algorithm described here requires the aircraft have a representation of the environment which describes the distribution of travel cost at each altitude, but no other requirements are placed on the environmental model. In this work a Kalman filter is used to build a model of the environmental state so the cost distribution is a Gaussian, but this is not required.

This approach is conceptually similar to the lever pricing approach employed by Vermorel and Mohri in the POKER algorithm [51]. There are two significant distinctions between POKER and this algorithm. First, the algorithm described here can explicitly compute the value of the information gained rather than using a heuristic value. Second, coupling the altitude selection algorithm with a model of the underlying environment permits the algorithm to operate on continuous domains (using the altitude selection algorithm described in Section 7.3.2) that

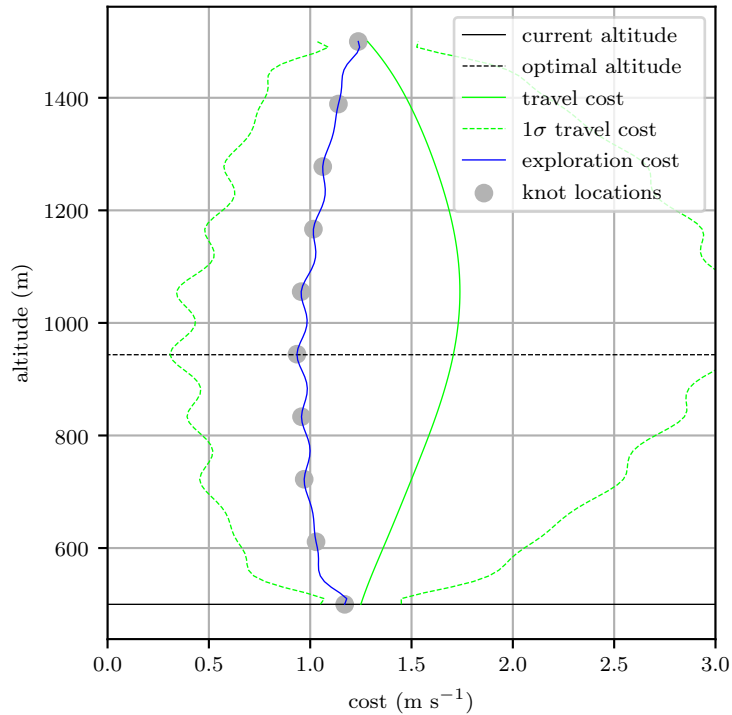


Figure 7.4: The exploration cost profile can be non-convex even if the underlying travel cost profile is.

are nonstationary (by virtue of the including time updates to propagate the belief distribution of the environmental model).

7.3.2 Finding the Lowest Cost Altitude

The algorithm described in Section 7.3.1 gives a semi-analytical form for the exploration cost profile. If the underlying travel cost profile and its variance is a smooth, continuous function then the exploration cost profile will also be smooth and continuous. The exploration cost will not necessarily be convex however, Figure 7.4 illustrates this effect.

Non-convexity in the travel cost profile variance can create non-convexity in the exploration cost profile, even if the travel cost profile mean itself is convex. In this case the the non-convex nature of the travel cost profile variance is driven by the structure of the spline model. The value of the function at each knot is dominated by the spline associated with that knot, so the function uncertainty is greater near

knots where the function value is influenced by fewer coefficients.

This issue is not unique to the spline model structure used here however. Non-convexity in the travel cost variance can arise in a number of ways: contemporaneous observation of several altitudes, nonuniform sampling of the profile, or process noise varying with height can all create this situation. There is also no guarantee that the underlying travel profile is itself convex.

Use of the spline model provides a means to address this issue. A basis spline of order 3 can be represented as a third-order polynomial that is piecewise continuous at the knots up to the second derivative. This means that there is at most one local minima and one local maxima of the function between two knots, so function minima between two knots can be found by a gradient descent begun at each knot point.

While the mean profile of the travel cost can have at most one local minima between each knot, when the expected value of the limited exploration cost distribution from Section 7.3.1 is computed, it is possible to for two additional local minima to be introduced by the profile variance. This makes it impossible to guarantee convergence of a gradient-based optimization to the global minimum exploration cost. While convergence cannot be guaranteed for any individual computation of the minimum exploration cost, this effect is reduced as the the travel cost uncertainty shrinks. This means that if the aircraft is drawn to a region in the support of a spline, the travel cost distribution will become more certain and the additional local minima will eventually be eliminated, allowing the true minimum to be determined.

A reasonable approach to determining the optimal altitude is then to numerically optimize Equation 7.6 using each knot point in the travel cost spline as an initialization value and choosing the altitude corresponding to the optimization result with the lowest cost. If the travel cost profile is very uncertain then this approach may converge to a local minimum, but exploration of this point will reduce the travel cost uncertainty and eliminate the local minima. The effect of local minima can thus be thought of in the same way as error in the travel cost profile – an error which may cause suboptimal guidance commands but which will be eliminated as the aircraft explores.

Because the optimization is over a single variable and the exploration cost is computationally inexpensive to evaluate, even a brute force solution is computationally tractable. Solving for the exploration cost at 5 meter altitude increments

(characteristic of the altitude holding performance of a small UAS) over a 1000 meter altitude band requires less than one second to compute. To isolate the performance of the exploration cost from the technique used to find the optimal altitude, the brute force solution is used in the results presented here.

7.4 Monte Carlo Simulations

To test the altitude selection algorithm, it is implemented in a numerical simulation of the SB-XC aircraft described in Section 3.2. The aircraft is simulated with 38.6% of the wing covered in solar cells which permits the aircraft fly under pure solar power but only near noon with no obstructions to solar energy. This wing coverage fraction represents the area of the inboard wing panel forward of the flap as this portion of the wing would be simplest to fit with a solar array.

Six-hundred fifty two simulations covering a period from 2018-11-04 to 2019-12-15, Figure 7.5 shows the start hour for each simulation. Not all hours in the time period are represented due to errors in the script which downloaded and processed the data files as they were made available. Section 4 demonstrated that the aircraft energy budget is most sensitive to wind, so simulations were run for both day and night conditions to provide more simulation iterations.

7.4.1 Simulation Tests

The aircraft is commanded to fly a 200 kilometer mission beginning near Eastern West Virginia Regional Airport (39.3977°N, 77.9978°W) and ending near William T Piper Memorial Airport (41.1466°N, 77.4166°W). The mission length is chosen for a nominal flight time of approximately 3.5 hours. This is characteristic of the endurance of many small aircraft [111]. The four hour forecast is also approximately when the wind forecast root mean square error reaches a steady-state value [112]. Atmospheric features with scales larger than four hours should be resolved fairly well then and can be handled by *a priori* planners which can provide outer-loop guidance targets, but *in situ* planning is needed to account for position and timing errors in forecasting smaller features.

Two types of planners were employed for comparison. The first baseline planner generated a nominal altitude trajectory before flight which was then tracked open-

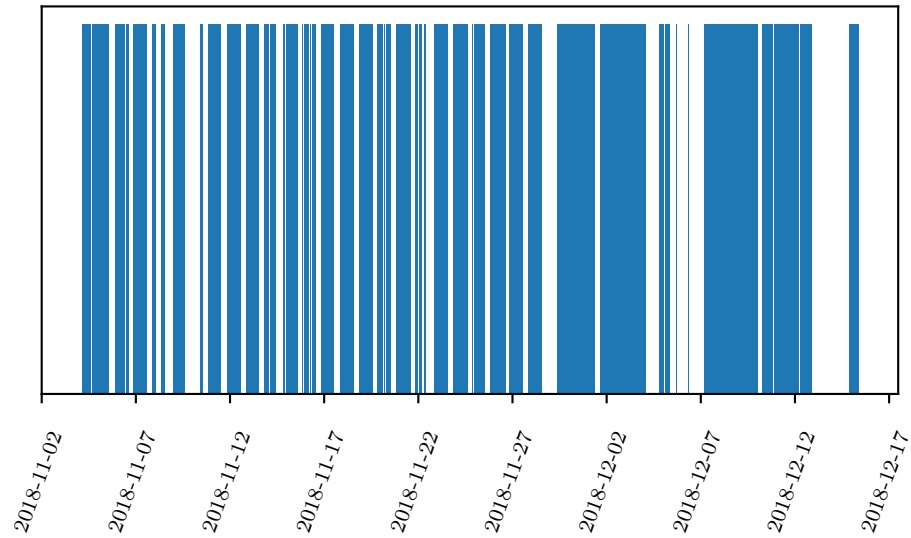


Figure 7.5: Six-hundred fifty two runs were conducted between early November and mid December 2019. The download script used to collect model data occasionally failed so not every hour in the range was simulated.

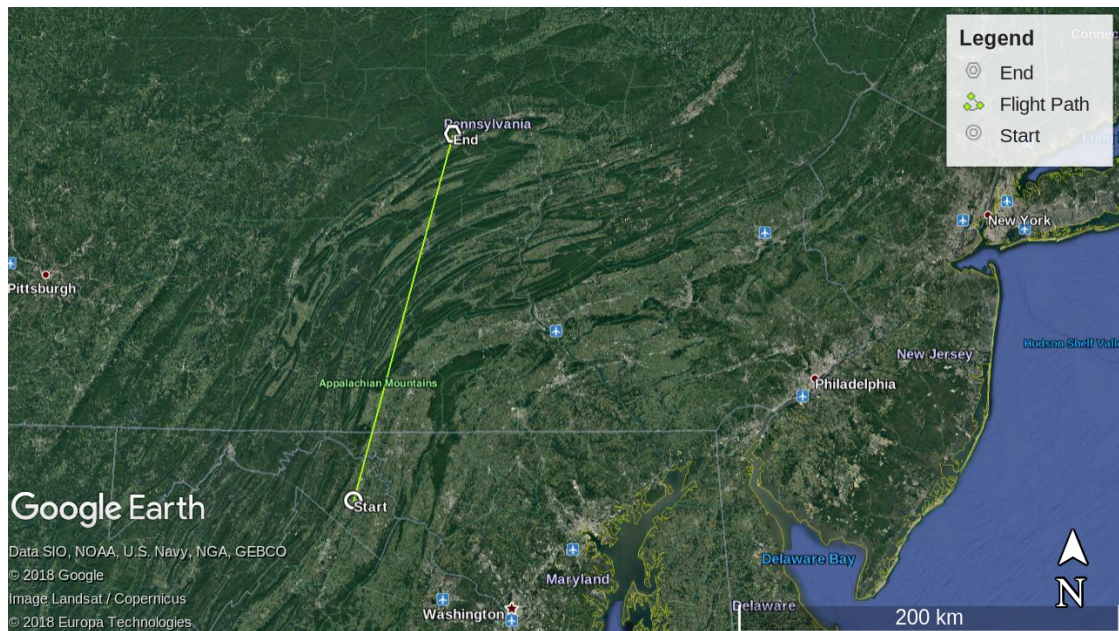


Figure 7.6: The aircraft is commanded to fly a 200 kilometer straight-line flight from West Virginia to central Pennsylvania. The permissible altitude band keeps the aircraft at least 100 meters above terrain throughout the flight.

loop. The nominal flight path was generated using the SciPy `minimize` routine [91] with the total energy expended from onboard storage as the objective function. The solver was used to find the optimal altitude at ten evenly spaced collocation points. At each collocation point the environmental conditions were interpolated from the gridded output of a numerical weather model and the required power output from storage to achieve the desired climb rate and speed was then computed. The total energetic cost to complete the mission was then computed using a fourth order Runge-Kutta integration. This approach will be referred to as the *a priori* planner in the simulation results.

The altitude selection algorithm described in Section 7.3 was also implemented in the simulation. The environmental model described in Section 6 is used to learn a model of the environment for use by this algorithm. In the simulation results this approach is called the *in situ* planner.

To characterize the value of information and the effect of model error on the performance of each planner, the availability and age of the information provided is varied. One *in situ* planner was provided with no *a priori* knowledge of the environment at all. Its wind model was initialized to zero, solar profile to a cloud factor of 0.5, and the model covariances to the climatological variance. For this planner time updates merely propagate the model covariance, increasing it by the mean drift rate of the environmental state.

Other *in situ* planners are provided with a HRRR forecast or analysis grid which is used to initialize the profiles and provide the total derivative of the environmental state during the mission. The initial covariance for these planners is initialized to the HRRR skill in the wind and cloud factor, $6.25 \text{ m}^2 \text{ s}^{-2}$ and 0.096 (squared irradiance fraction) respectively [88, 113]. The wind component and cloud factor process noise is set to the mean growth rate in forecast error computed in Section 6.1.2 ($0.95 \text{ m}^2 \text{ s}^{-2} \text{ h}^{-1}$ and 0.0914 h^{-1}). The *a priori* planners are all provided with a HRRR grid for use in computing the nominal trajectory.

For each class of planner the HRRR grid provided is drawn from the analysis, 1, 2, or 3 hour forecast. This introduces error into the aircraft's *a priori* environmental knowledge that reflects regions, features, and properties where the forecast changes most. This should represent the most uncertain components of the environmental state. Reference to Figure 6.4 shows that the mean squared difference in the HRRR wind vector between the three hour forecast and analysis is only about $3 \text{ m}^2 \text{ s}^{-2}$,

about half of the analysis error, so the simulations will understate the error in the forecast (forecasts made three hours apart are more consistent with each other than they are with the true atmospheric state). All simulation cases use the HRRR analysis as the realization of the environmental state, so the aircraft provided with the analysis have perfect information as from an “oracle,” and represent a bounding case on performance.

The nominal flight time (tracked by each aircraft using the method described in Section 5) is determined from the flight time required for the *a priori* planned flight path with perfect information to reach the goal point with a constant airspeed of 16 m s^{-1} , this is slightly faster than the aircraft’s best range speed, which is typical for cruise speeds of light aircraft and small UAS. A constant nominal airspeed is specified instead of a groundspeed because the standard deviation of wind speed is greater than 8 m s^{-1} (computed from the HRRR grids used to compute the process noise in Section 6.1.2). This is more than half of the aircraft’s speed for best range, so specifying a constant inertial speed at a speed near the best glide speed is not possible (for example with a tailwind equal to the flight speed) or unreasonable (when facing a strong tailwind). Permitting the inertial speed to vary in response to environmental conditions is also consistent with typical operating practice for aircraft.

7.4.2 Mean Performance

The performance of each planner is analyzed through its regret relative to the perfectly informed *a priori* planner. The final regret after 652 simulations was averaged to compute the mean final regret. Regret for the *in situ* and lagged optimal planners is summarized in Table 7.1. Regardless of the age of information provided, the *in situ* planner actually outperforms the *a priori* optimal control-collocation planner. When the *in situ* planner is provided with *a priori* information to initialize its profiles and provide time updates, its mean energy consumption is 3-4% less than the perfectly informed *a priori* planner. With no prior information the *in situ* planner has a mean energy consumption 2% less than the *a priori* planner.

Figure 7.7 illustrates the mean regret as a function of the aircraft position (because of differences in the time to complete the mission, the mean computed for fixed locations is more informative than the mean at fixed times). The jumps

Table 7.1: Mean final regret averaged over 652 simulations.

strategy	regret (m)	regret (%)
<i>in situ</i> , no forecast	-233	-2.0
<i>in situ</i> , perfect information t	-466	-4.0
<i>in situ</i> , 1 hour forecast	-432	-3.7
<i>in situ</i> , 2 hour forecast	-383	-3.3
<i>in situ</i> , 3 hour forecast	-378	-3.2
<i>a priori</i> , 1 hour forecast	216	1.8
<i>a priori</i> , 2 hour forecast	319	2.7
<i>a priori</i> , 3 hour forecast	316	2.7

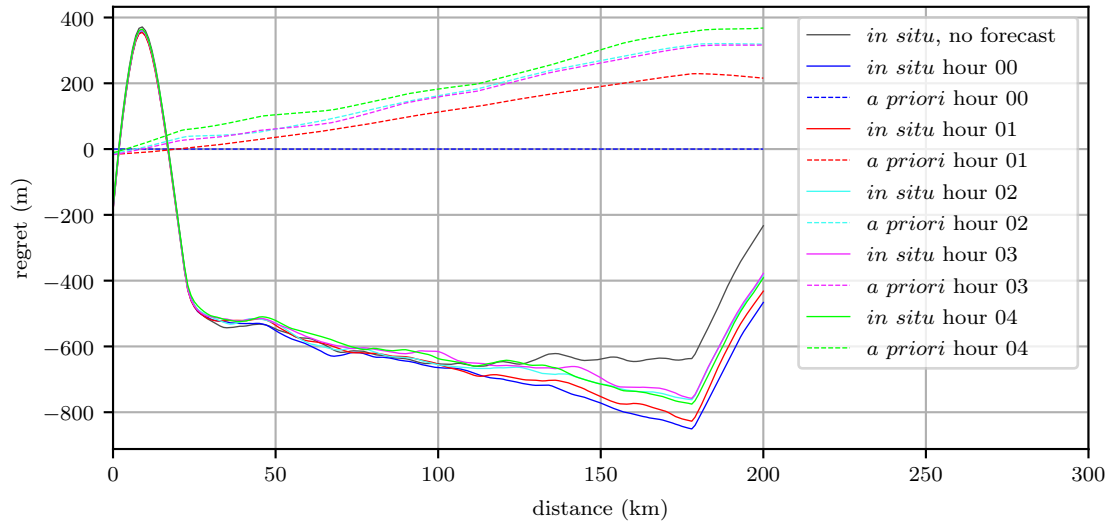
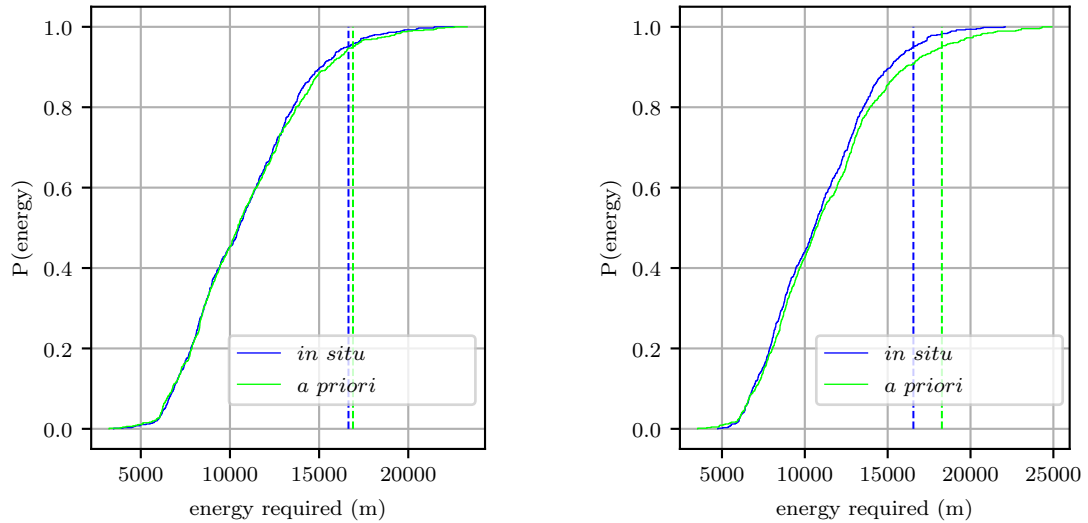


Figure 7.7: Mean regret averaged over 652 simulation runs.

in regret at the beginning and end of the mission stand out. The initial jump in regret occurs because in many simulations the *a priori* planner immediately climbs at the maximum permitted rate to explore or reach a desired altitude. The climb rate of the *a priori* is constrained by the resolution of the collocation points used for planning. The final jump in regret occurs because the *a priori* planner reduces altitude near the end of the mission, gliding to reduce its energy consumption. These two effects are explored further in Section 7.4.4.



(a) Energy required to complete the mission if the environmental state is known perfectly.

(b) Energy required to complete the mission when the planners are provided with a four hour forecast.

Figure 7.8: Empirical cumulative distribution of the energy required to complete the mission. Vertical dashed lines indicate the 95th percentile of energy consumption.

7.4.3 Energy Budget for Likely Mission Completion

Section 7.4.2 illustrates the mean performance of the various strategies relative to a perfectly informed optimal control approach. The mean energy required to accomplish a mission is not a good metric of performance however, it is likely that in many cases more than the mean energy will be required. A better measure is the energy required to complete a mission with a specified likelihood. Figure 7.8 illustrates the empirical cumulative distribution of the energy required to complete the mission.

Figure 7.8a shows the distribution of final specific energy expended (consumed from storage minus remaining altitude) when the planners are provided with perfect information. The vertical dashed lines indicate the 95th percentile energy expenditure. The distributions are very similar, though the *in situ* planner achieves slightly better performance using the 95th percentile energy consumption as a criterion. This is likely due to the higher effective planning resolution, which is discussed further in Section 7.4.4.

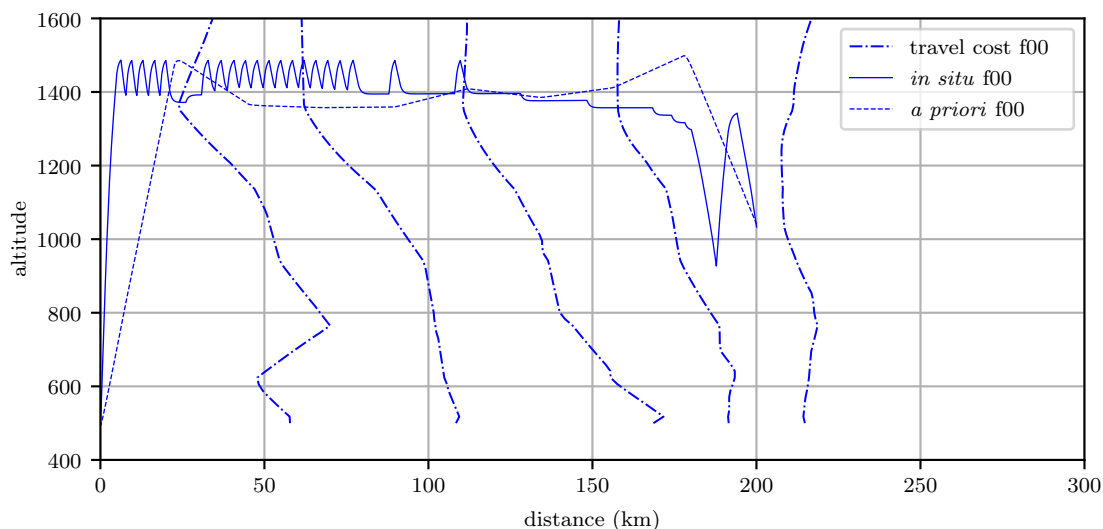
Figure 7.8b shows the same comparison of distributions when the planners are provided with a four hour forecast. Recall from Section 7.4.1 that the lagged forecasts are actually introducing less error than the analysis skill of current weather models, so the effect of forecast error is understated by this simulation. The difference in the 95th percentile energy is greater with the longer-range forecast, approximately 1500 m or 9% of the 95th percentile energy for the *in situ* planer. This indicates that the *in situ* environmental modeling and planning is mitigating some of the cost incurred by error in the weather forecast.

7.4.4 Comparison of Trajectories

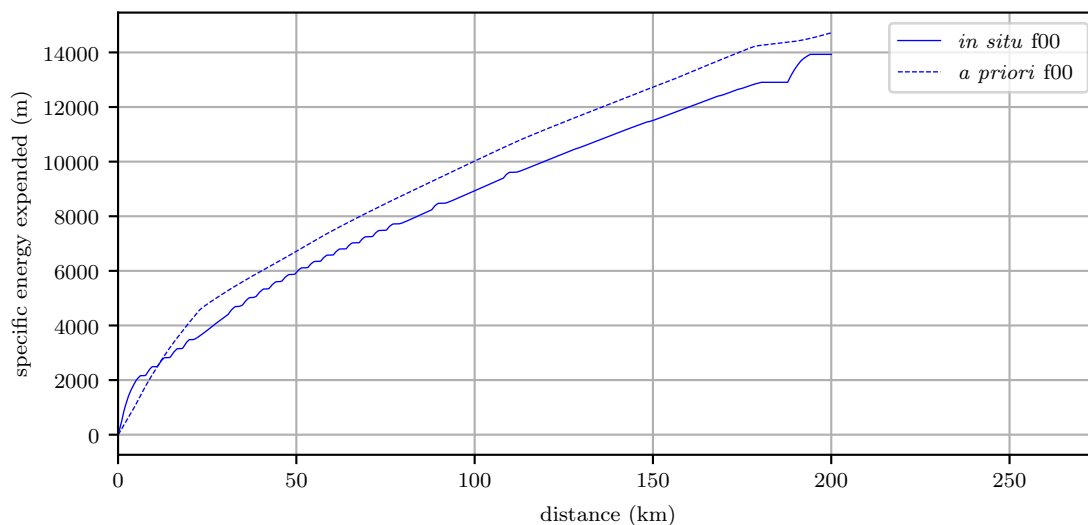
Figure 7.9 compares the flight path and energy state for the two planners with perfect information during the run beginning 2018-11-15 at 22:00 UTC. The figure also depicts the true travel cost profile (scaled by a factor of 10 for visibility) every 50 kilometers. During this run the *in situ* planner used 800 m less energy, a reduction of approximately 6% relative to the *a priori* planner. Examining the trajectories in detail highlights some differences between the two planning approaches.

Early in the flight the *in situ* planner can be seen to command an immediate change in altitude. Because the resolution of the *a priori* planner is limited by the number of collocation points it cannot reach the optimal altitude until the second collocation point at the earliest (the first collocation point defines the mission start location). In contrast, the *in situ* planner has a resolution equal to the rate at which the guidance algorithm is run so it commands an immediate change to the altitude it identifies as favorable for exploration. Greater resolution could be achieved in the *a priori* planner by adding collocation points or including the collocation point locations in the optimization. These approaches would require expanding the optimization state vector which significantly increases the computation time. An experiment with doubling the number of collocation points increased the convergence time by an order of magnitude, from approximately 600 seconds to approximately 7000 seconds, making it unsuitable for use onboard an aircraft.

Late in the flight both planners command a descent, using their gravitational potential energy to avoid using stored energy in a maneuver analogous to the “final glide” employed by sailplanes [35]. The *a priori* planner shows itself more



(a) Flight path for the perfectly informed planners. The *in situ* planner can be seen exploring a nearly-constant wind band in order to fine-tune its altitude.



(b) Expended stored energy trajectory. Not having a resolution limit, the *in situ* planner can rapidly climb to the most favorable region and achieve lower cost travel very rapidly.

Figure 7.9: State trajectories and travel cost profiles for perfectly informed *in situ* and *a priori* planners for the mission beginning at 2018-11-15 22:00 UTC. Both planners reached the optimal altitude, but the *in situ* planner is able to do so sooner. Near the end of the flight, the growing model covariance and shrinking payback period induce the *in situ* planner to explore lower. It finds the winds are still strong and retreats back to a higher altitude before beginning a “final glide.” This maneuver lowers its energy consumption, but the *a priori* planner achieves a lower-cost “final glide.”

adept at planning the final glide. This makes sense, after all the *a priori* planner is explicitly attempting to find the altitude trajectory which minimizes the total energy consumption.

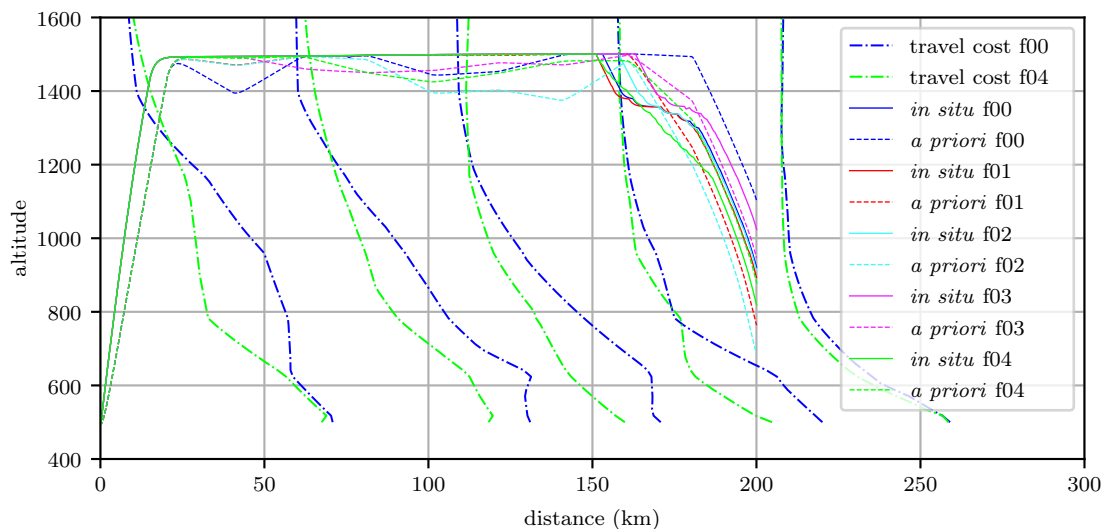
In contrast, the *in situ* planner merely determines that the chance that favorable conditions exist at a lower altitude is high enough that the significant (albeit temporary) reduction in power output justifies the risk of exploring. In this case, the covariance has grown enough that the *in situ* planner commands an “early” final glide, one which it initially reverses upon observing that the winds are still strong. Eventually, the mission end is near enough that the reduction in power consumption is worth starting another glide even in the face of strong winds. While the *a priori* planner produces better final glide plans, the fact that the final glide behavior emerges naturally from the exploration / exploitation balance is striking.

7.4.5 Effect of Information Age

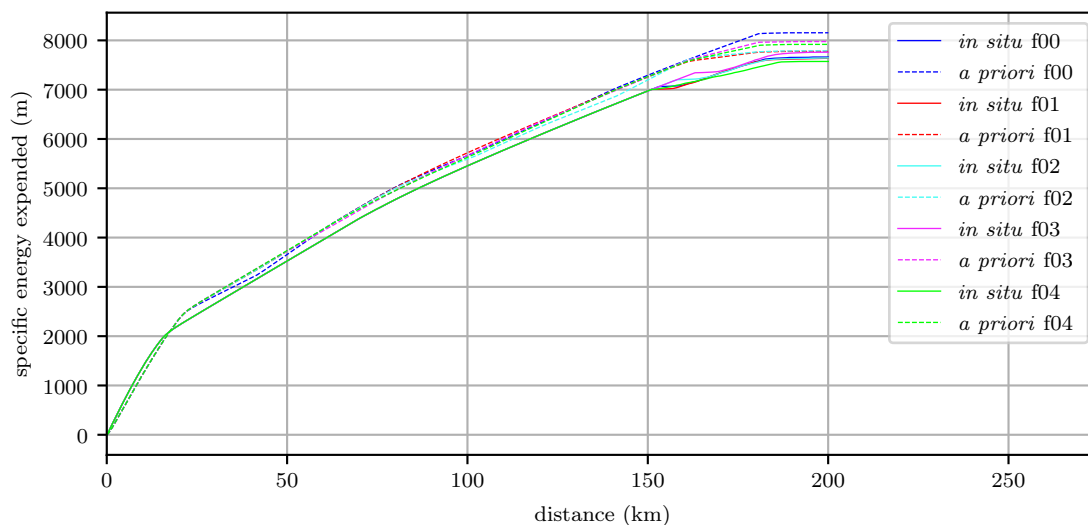
The atmosphere often exhibits relatively consistent conditions for a period of hours to days until a sudden transition occurs to a new state [59]. The exact timing and location of these transitions is often difficult to forecast in advance, so during these transitions longer-range forecasts are likely to introduce additional error into the expected atmospheric state and thus flight plan. During the quiescent periods performance of both the *in situ* and *a priori* planners should be nearly independent of the forecast length. During the simulation depicted in Figure 7.10, initialized 2018-11-05 at 02:00 UTC, a strong tailwind was present that increased with altitude. This drove all of the controllers to command an altitude near the maximum permitted, small errors in the forecast atmospheric state did not change the optimal flight path significantly.

When the weather is changing, longer-range forecasts have difficulty exactly placing the location or timing of changes. This is depicted in Figure 7.11 which shows state trajectories for the simulation run initialized on 2018-11-14 at 20:00 UTC.

The flight path was under a building high pressure system that was preceded by strong northwest winds. Early forecasts expected the high pressure to build in rapidly, bringing weaker winds with it and shifting the optimal altitude from low to high. The high pressure did not build in as rapidly as the initial forecasts

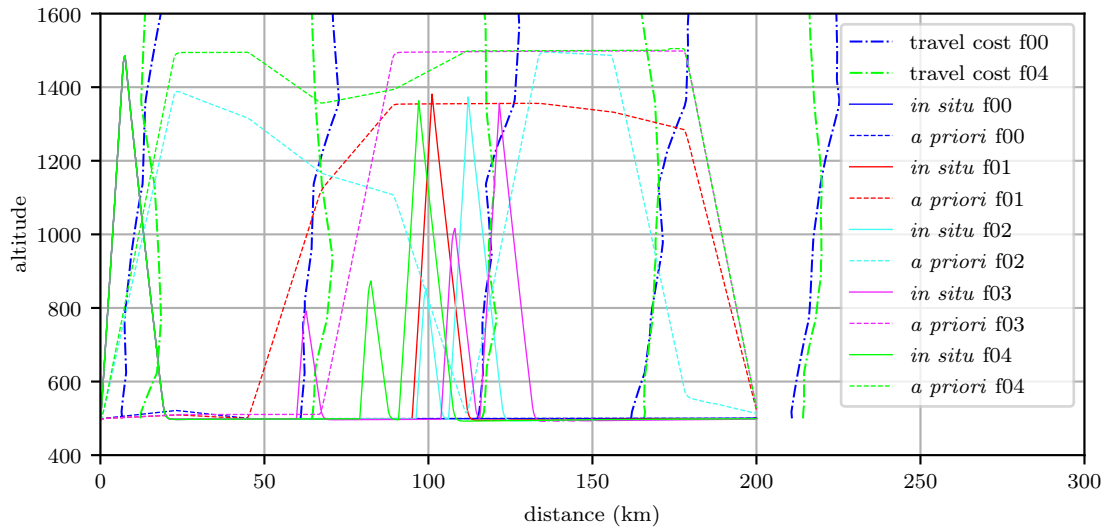


(a) Regardless of the forecast age, all travel cost profiles favor a high altitude so the planners all command a flight path near the maximum permitted altitude.

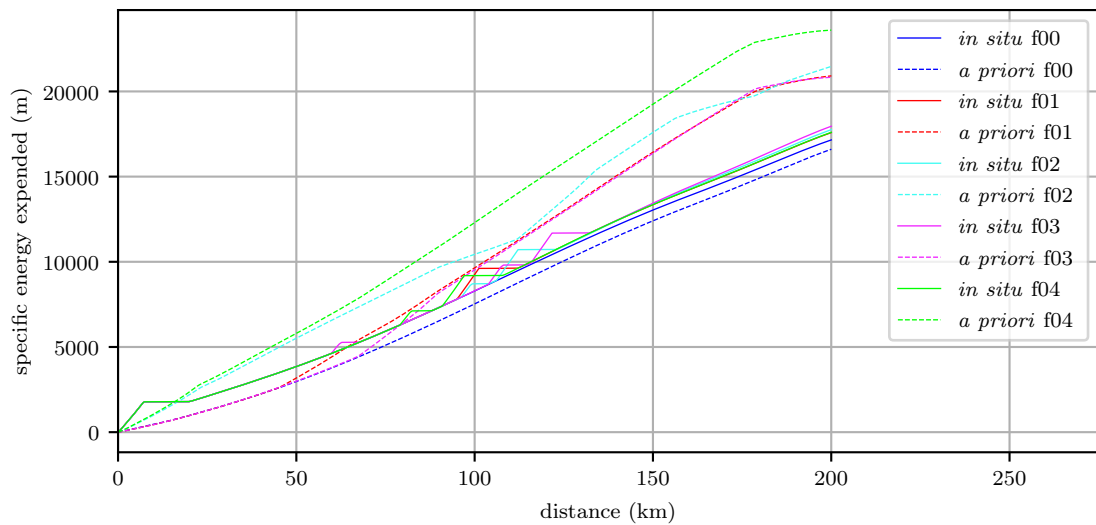


(b) The *in situ* planner achieves slightly lower energy expenditure because it immediately climbs to the maximum altitude, but otherwise both planners cluster around similar energy costs.

Figure 7.10: State trajectories from the run beginning 2018-11-05 at 02:00 UTC. A consistent tailwind was present the entire flight, which increased with height. Error in the forecast atmospheric state does not significantly impact the commanded flight path.



(a) The trajectories computed using longer range forecasts expect the optimal altitude to shift from the minimum to maximum altitude. The *a priori* planners using this data are unable to determine that the shift does not occur. The *in situ* planners explore and find that the travel cost is greater than expected so they return to a low altitude.



(b) Acting on the incorrect information, the *a priori* planners using longer-range forecasts have considerably higher total mission energy requirements. The *in situ* planners using this incorrect information are able to correct it and pay a smaller price.

Figure 7.11: State trajectories from the run beginning 2018-11-14 at 20:00 UTC. When the atmosphere is evolving rapidly the forecast error can be quite large and following an altitude profile computed using old information can be very costly.

anticipated which can be inferred by the altitude traces – shorter-term forecasts push the climb from low to high altitudes later in the flight. In the end, the weaker winds did not occur until after the flight so the planner with perfect information remains at the minimum altitude throughout the flight. The *in situ* planner shows a similar pattern – the *in situ* planners provided with longer-range forecasts find it likely that there is a favorable region at high altitude and begin climbing between 75 and 100 kilometers into the mission. Observations quickly show the anticipated weaker headwinds not to exist and the *in situ* planners then command a descent to the minimum altitude.

Examining the energy expended, it is clear that the *in situ* planners which have this “bad information” pay a price, their total energetic cost is increased by about 500 m, but this is a considerable advantage over the *a priori* planners whose cost is increased by more than 4000 m.

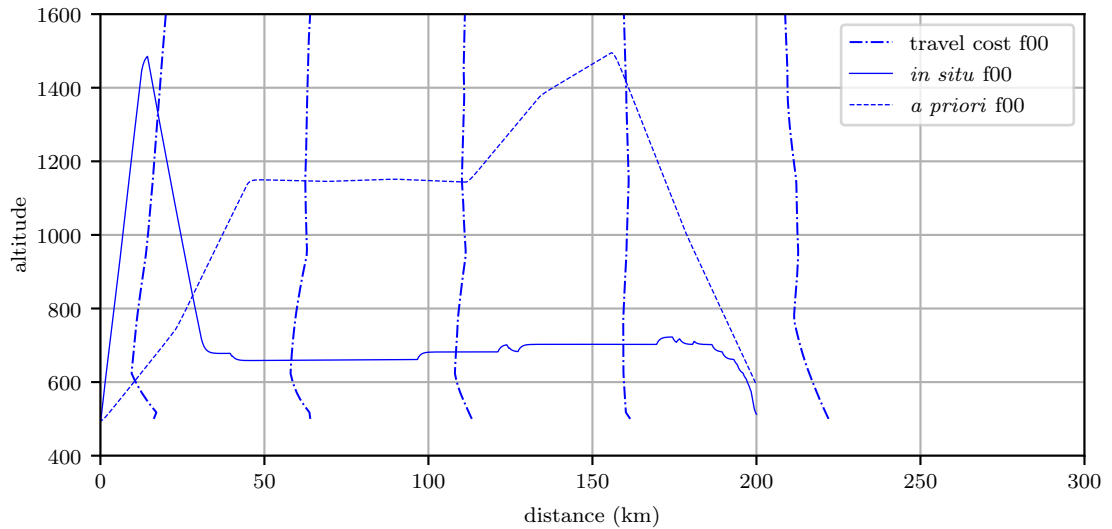
7.4.6 Robustness to Local Minima

The collocation based planner uses a gradient descent algorithm to find the trajectory which minimizes energy. The initial guess for the trajectory is one which climbs to the maximum altitude then descends to the minimum at the end of the flight, exposing the optimization algorithm to the atmospheric conditions at all altitudes. Most of the time this approach converges to the best trajectory, but occasionally there are local minima in the travel cost which the gradient descent cannot climb out of. One such situation is shown in Figure 7.12.

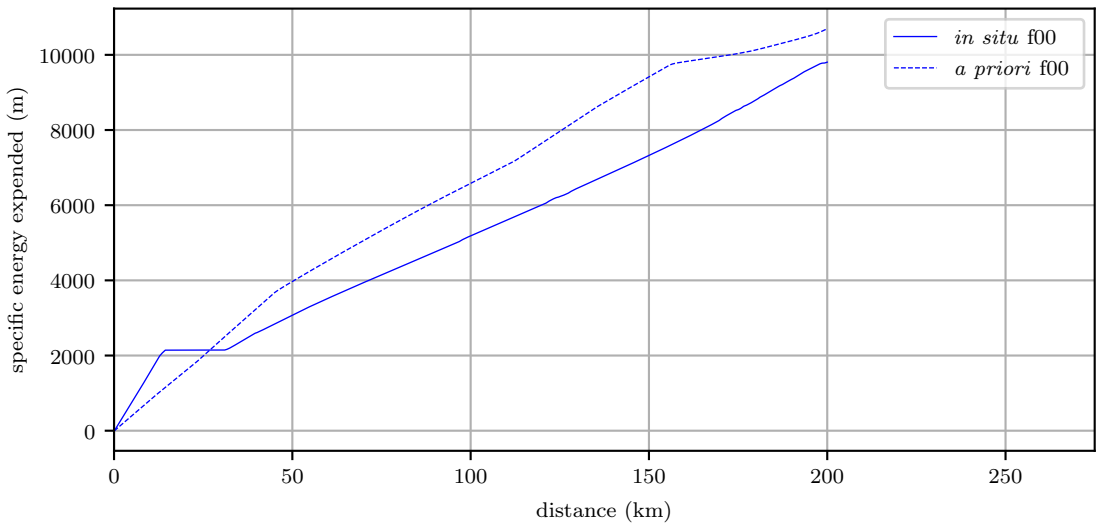
This could be ameliorated to some extent by multiple restarts of the *a priori* planner with various initial conditions, but at the cost of additional planning time. Each solution of the *a priori* planner takes between 10 and 20 minutes, so multiple restarts could be a very costly way to compute the optimal trajectory. In contrast each altitude selection by the *in situ* planner takes only a fraction of a second to compute, permitting it to run continuously onboard a small UAS.

7.4.7 Value of *a priori* Information

Table 7.1 gives a rough indication of the value of having prior information – the mean regret relative to the fully informed case tends to grow as the age of information increases. In the extreme case, the *in situ* planner which is provided with no *a*



(a) The *a priori* planner does not converge to the global minimum energy trajectory because it requires the optimization to traverse a region where cost increases with altitude. In contrast the *in situ* planner considers the probability of the global minima occurring at a given altitude and explores regions that are likely to have minimum cost.



(b) Identification of the global minima permits the *in situ* planner to achieve a modest decrease in energy relative to the *a priori* planner.

Figure 7.12: State trajectories from the run beginning 2018-11-12 at 04:00 UTC. Because the *in situ* planner considers the entire profile when selecting an altitude and considers the exploration cost probabilistically it is less susceptible to being trapped in local minima than the *a priori* planner which uses a gradient descent to find the minimum cost trajectory.

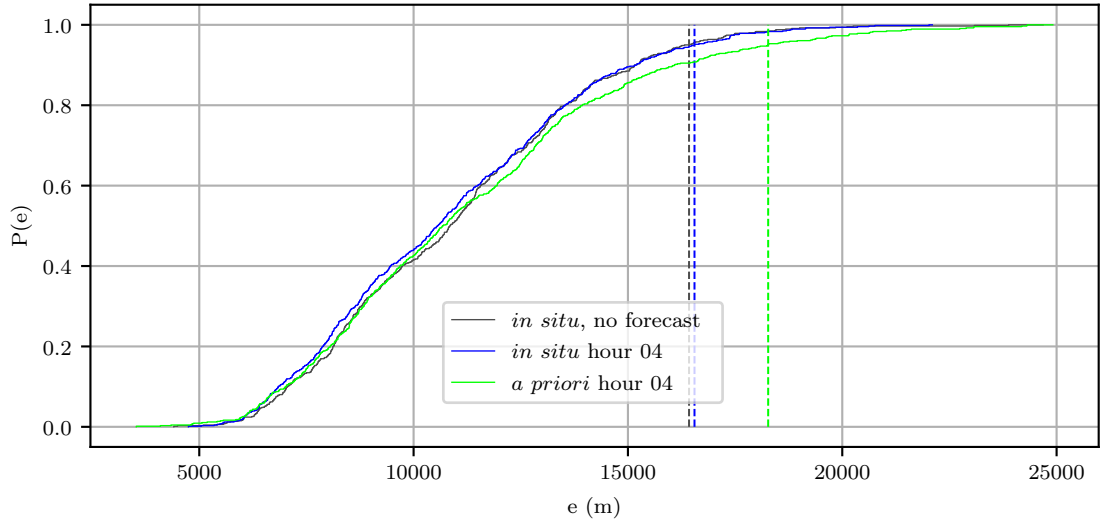


Figure 7.13: Empirical cumulative distribution of final energy state for the *in situ* and *a priori* planners with a four hour forecast and for the *in situ* planner with no prior information.

priori information has a regret approximately 2 percentage points greater than the informed case. As discussed in Section 7.4.3 mean regret is an imprecise way to evaluate the effect that *a priori* information can have.

Error in the aircraft’s knowledge of the environment does not in itself incur additional energy expenditure. If the environmental model is in error but the error is structured such that the optimal altitude is unchanged (e.g. off by a scale factor throughout the profile), then either planner will still drive the aircraft to the optimal altitude. Environmental error can only drive the aircraft to suboptimal decisions when the error magnitude or structure is such that it identifies an incorrect altitude as the optimal.

With this in mind, examination of Figure 7.13 illustrates the empirical cumulative distribution for the *a priori* and *in situ* planners with four hour old information as well as for the *in situ* planner which was provided with no prior information.

The similarity of the distributions and 95th percentile energy required for the *in situ* planner with and without energy indicate two things. First, that uncertainty in the forecast makes time updates to the observed profile of limited utility in making decisions. Second, that the environmental model constructed from *in situ* observations is capable of representing the environment over the moderate term

with enough fidelity to enable the aircraft to manage its energy and risk state. Once the forecast becomes unreliable there will occasionally be circumstances that significantly degrade the performance of any planner relying on *a priori* information. This is probably the reason why the 95th percentile performance between the *in situ* planner with and with *a priori* information is much smaller than the mean performance difference. When a forecast is good, environmental conditions tend to be consistent and the “persistence forecast” of the uninformed atmospheric model is not a bad approach. When environmental conditions experience a significant change (e.g. frontal passage) over the course of a flight, the error in the exact timing and location of the change can have enough error that time updates from the forecast will misinform the aircraft. In this case the greater process noise associated with the *in situ* planner without *a priori* information enables this planner to admit this large change and respond as well as the planner receiving time updates.

7.5 Summary

Determining the flight profile to minimize energy consumption can be considered as a continuous, non-stationary multi-armed bandit problem. While this is a particularly challenging form of multi-armed bandit, it captures the explore/exploit tradeoff better than sensor placement or information maximization approaches which require heuristic functions to provide value to the gain of information.

An algorithm is proposed which uses the option to retreat to the initial altitude to limit the exploration cost and provide an explicit energetic value for gaining information. This approach integrates well with the atmospheric structure modeling system described in Section 6 and is able to select an altitude near enough the global minimum that the decision can converge to the global minimum as information is gathered. This algorithm has the interesting ability to suggest remaining at the current altitude in order to gain additional information because the aircraft’s current environmental model could admit a more favorable profile than the current mean value.

The altitude optimization algorithm is able to incorporate mission constraints by penalties in the cost profile. For some constraints it may be possible to construct a penalty which actually represents the additional energy required to complete a mission at a given altitude, in other cases a utility function will be required. The

constraint problem can also be inverted – given a desired altitude and a specific power budget, the aircraft can identify an altitude nearest the desired which falls within the budget.

The altitude selection algorithm is tested in Monte Carlo simulations against a collocation based planner which tries to minimize the total mission cost using a gradient descent minimization algorithm. On average the *in situ* planner is able to achieve performance superior to the collocation based planner. The *in situ* planner also exhibits greater robustness to the existence of local optima. The planner considers the entire profile and the distribution of travel cost rather than the expected value. This enables it to identify multiple altitudes which are likely to be the optimum and prioritize these altitudes for exploration to determine which is truly optimal.

With perfect information and no restriction on the computational resources available, the collocation planner can achieve higher resolution and handle local optima via multiple initializations. It should converge on the optimal trajectory, bounding the performance of any planner, so the fact that the *in situ* planner outperforms the perfectly informed collocation planner here is a result of the restricted computational time allowed. Improved optimization algorithms and computers would erode the advantage displayed by the *in situ* planner in the perfectly informed case.

In practice, the aircraft will never have perfect knowledge of the environment, the combination of a planner and environmental modeling system that both run *in situ* allows for correction of error in the environmental state propagation. This makes the planner much more robust to situations where the environment changes in a way which is not resolved well by forecast information provided *a priori*. The *in situ* planner has this advantage regardless of the computational resources available to plan a trajectory *a priori*.

Finally, the algorithm is capable of finding energy efficient trajectories even when started up with nothing more than knowledge of the climatological variance in the environment and provided with no forward propagation of the atmospheric state. On average the *in situ* planner provided with no *a priori* information outperforms the *a priori* collocation based planners. In some cases it is actually an advantage not to have prior information – when there is significant forecast error then the time updates can try to lead the *in situ* planner astray.

Overall the multi-armed bandit approach to *in situ* trajectory optimization appears to be a promising way to manage uncertainty and energy conservation for small UAS. It permits the energetic value of information to be determined and exploration decisions to be made on the likelihood of finding more favorable regions. In simulations the *in situ* approach demonstrates lower mean cost and greater confidence in the energy required to complete a mission when compared with an *a priori* optimization.

Chapter 8 | Conclusion

While considerable progress has been made in the capability and sophistication of robotic aircraft, most current UAS fall into one of two categories – large aircraft best described as “conventional aircraft with no one in it” and small aircraft and multirotors resembling or adapted from “toy aircraft.” In order to provide the benefits of an aerial platform with reduced acquisition, maintenance, and operation costs an intermediate space is needed for small UAS which have the range, endurance, and autonomy to conduct lengthy missions without constant monitoring and intervention. Until now the development of this class of aircraft has largely been constrained by regulation, but as this thesis was written UAS were given air carrier designation for the first time, opening the possibility of extended commercial flights [114].

The impressive stabilization and control of small UAS often gives the impression of greater capability and autonomy than currently exists. As the number of high performance sailplane pilots that land in fields would attest, poor decision making can overcome the inherent performance of any aircraft. The capability of small UAS to handle adverse weather conditions resembles general aviation aircraft more than transport aircraft. In the case of unexpected winds especially, small UAS are more sensitive even than light airplanes and helicopters. This does not make it impossible to operate small UAS safely and effectively – after all small aircraft regularly fly in challenging conditions – but requires an awareness of the environment and sophisticated decision-making that is usually provided by an expert pilot.

Proponents of drone deliveries, agricultural monitoring, and urban air mobility envision a future where relatively small aerial robots are ubiquitous. This thesis attempts to move the state of the art in environmental awareness for small UAS forward to help enable this vision and perhaps keep the count of YouTube videos

featuring “drone runs out of battery” in the title from growing beyond the current count: 85,000. In particular, this thesis addresses the needs and capabilities of small solar augmented UAS, but many of the innovations developed are applicable to UAS in general and the insights can inform autonomous decision-making more generally.

8.1 Summary of Contributions

8.1.1 Separation of Scales of Response to Atmospheric Uncertainty

The separation of scales of atmospheric variation and uncertainty can be exploited to layer guidance techniques. Traditional optimization-based long-range planning can respond to atmospheric variation at scales exceeding the atmospheric energy spectral gap, providing outer-loop guidance to lower-level systems. Within the spectral gap, *in situ* observation and planners can be used to find flight paths to minimize the effect of error in the expected atmospheric state. High frequency variations in the environment appear as random disturbances to the aircraft and controllers can be designed to react to the immediate atmospheric state to efficiently respond to these disturbances.

8.1.2 Speed Control to Manage Stochasticity

Separability of the speed and power control is shown. Speed commands can be used to respond to stochastic variations in the environment in a way that makes the environment more favorable to the aircraft. A speed control is derived which permits harvesting energy while meeting an arrival time condition. This control is evaluated in simulation and shown to reduce energy expenditure and uncertainty in the final energy state. In flight tests it is able to meet arrival time specifications within 1% even under the influence of considerable unmodeled dynamics.

8.1.3 Environmental and Travel Cost Modeling

An approach to modeling the environment in flight is developed which uses a Kalman filter to estimate the coordinates on a basis of *a priori* specified functions

which best describe the mean atmospheric state. This approach permits many observations to be fused with no performance penalty as the number of observations grows, and for observations from other aircraft and sensors to be assimilated into the model. The Kalman filter framework also permits updating the environmental state with derivative information if available, and provides an estimate of not only the atmospheric state, but confidence in the state estimate.

A transformation is defined which permits converting the environmental state into a travel cost, permitting the aircraft to assess the cost of travel in any direction at a desired speed from information gathered in flight. The filter is tested onboard a small UAS and compared to numerical weather model analyses and to observations collected by balloon-borne radiosondes. The results demonstrate that aircraft observations are able to describe the environmental state, and show significant differences between observed and model predicted conditions. This demonstrates the need for *in situ* observations and planning to enable efficient autonomous flight by small UAS.

8.1.4 *in situ* Flight Planning

A multi-armed bandit approach to flight planning is developed to balance exploration of the environment with minimizing travel costs. By exploiting the ability to retreat to a previous state, the cost of exploration can be limited and regions can be identified where exploration is likely to pay off. This framework also allows the value of information to be defined.

The *in situ* planner is evaluated in Monte Carlo simulations covering 652 initial times in November and December 2018. In comparison with a collocation-based optimal control planner, the *in situ* planner can provide higher resolution guidance at low computational cost. It also demonstrates the ability to reduce the impact of forecast uncertainty on the cost required to complete a mission and robustness to local minima in the cost profile.

8.2 Recommendations for Future Research

8.2.1 Managing Stochasticity in Other Domains

The speed control algorithm developed to manage stochasticity in the environment is able to make the effective environment more favorable by preferentially spending more time in favorable regions. This approach can be applied to other domains and objective functions. For example, an autonomous car on a highway may identify certain regions with higher probability of hazards (either globally or relative to other vehicles) and vary its speed to minimize the cumulative risk of an accident.

8.2.2 Identification of and Response to Weather Hazards

This thesis focuses largely on improving UAS capability. Assuring sufficient energy is available to complete a mission enhances safety, but safe flight in response to environmental conditions embodies a much larger field of research. The modeling and exploration techniques developed here could be applied to the identification of some hazards, such as in-flight icing. The response to weather hazards needs to be different than the approach adopted for energy efficiency in this thesis however. Iteratively re-exploring previously visited regions to maintain a model of the environment is not appropriate when every encounter with a hazardous condition carries the risk of damage to the vehicle or loss of control.

8.2.3 Multi-Armed Bandit Planning

The multi-armed bandit approach to planning under uncertainty shows considerable promise. The problem examined in this thesis is well suited to solution by this approach, but it may be applicable to other aircraft planning problems and for robotics in general. For aircraft guidance the same approach could be used to identify lateral offsets from a nominal flight path which reduce energy consumption (for example because strong winds create bands of clouds aligned with the flight path).

In principle, the multi-armed bandit planner is a good candidate for distributed systems. Information shared between multiple agents should permit actions with low cost to be rapidly identified and the team would be able to maintain a shared

understanding of the environment at little individual cost. Since the planner is computationally inexpensive to run, it should scale well across many systems with limited processing resources.

8.2.4 Exploration Cost

While the structure of the optimization problem allows any exploration cost that can be represented as an energy rate the exploration cost employed in this work is relatively simple, representing just the altitude change required to gather information. This is constructed under the assumptions that the aircraft power system is equally efficient at all power outputs and that the time required to explore is small relative to the mission length.

Even under these assumptions the system performs well, but it would be worth exploring the effect of higher fidelity costs. When changing altitudes the aircraft power system must be run at a higher output, the efficiency of most power systems varies with output so this effect could be included. Additionally, unless the time required to explore is truly infinitesimal there is an “opportunity cost” to gathering information. During exploration the aircraft is likely to traverse areas where its travel cost is higher than at the initial altitude. The additional energy expended when traversing this region could be included in the transition energy and thus exploration cost.

Finally, the algorithm as described here makes exploration decisions based on the information to be gathered at the location it decides to visit. During exploration the aircraft gains information about all of the intermediate locations. This information is not currently accounted for when selecting an altitude to explore, pricing the information gained while in transition would be worthwhile as well.

8.2.5 Forward Looking Sensors

All of the sensing technologies examined in this thesis can only detect the environmental state at the vehicle position. As LIDAR, computer vision, and processing power improves it may be possible to gather information about the environment ahead of the vehicle. Incorporating this information into the aircraft’s guidance should permit more proactive decision-making, further reducing travel costs, and allowing the aircraft to avoid unfavorable and hazardous regions.

Works Cited

- [1] AURORA FLIGHT SCIENCES (2019), “Odysseus – High Altitude, Ultra-long Endurance, Pseudo-Satellite – HAPS – Aurora Flight Sciences,” .
URL <https://www.aurora.aero/odysseus-high-altitude-pseudo-satellite-haps>
- [2] NOTH, A. (2008) *History of Solar Flight, Tech. rep.*, ETH Zurich.
- [3] BOUCHER, R. J. (1984) “History of solar flight,” in *20th Joint Propulsion Conference*.
- [4] NOLL, T. E., J. M. BROWN, M. E. PEREZ-DAVIS, S. D. ISHMAEL, G. C. TIFFANY, and M. GAIER (2004) *Investigation of the Helios Prototype Aircraft Mishap; Volume I: Mishap Report, Tech. rep.*, National Aeronautics and Space Administration.
- [5] NATIONAL TRANSPORTATION SAFETY BOARD (2016) *NTSB Final Report DCA16CA197, Tech. rep.*, National Transportation Safety Board.
- [6] PHILLIPS, J., K. BYRON, S. PAUL, and J. FREED (2019), “Airbus says Zephyr test flight for UK Ministry of Defence was ‘interrupted’,” .
URL <https://www.reuters.com/article/us-airbus-zephyr/airbus-says-zephyr-test-flight-for-uk-ministry-of-defence-was-interrupted-idUSKCN1RN0QD>
- [7] AEROVIRONMENT (2019), “Puma AE Small UAS (UAV) - Aerovirement, Inc,” .
URL <https://www.avinc.com/uas/view/puma>
- [8] COCCONI, A. (2004) *AC Propulsion’s Solar Electric Powered Solong UAV, Tech. rep.*, AC Propulsion.
- [9] OETTERSHAGEN, P., A. MELZER, T. MANTEL, K. RUDIN, R. LOTZ, D. SIEBENMANN, S. LEUTENEGGER, K. ALEXIS, and R. SIEGWART (2015) “A Solar-Powered Hand-Launchable UAV for Low-Altitude Multi-Day Continuous Flight,” in *2015 IEEE International Conference on Robotics and Automation*, Seattle, WA, pp. 3986–3993.

- [10] STULL, R. B. (1988) *An Introduction to Boundary Layer Meteorology*, 1 ed., Springer Netherlands.
- [11] MASS, C. F., D. OVENS, K. WESTRICK, and B. A. COLLE (2001) “Does Increasing Horizontal Resolution Produce More Skillful Forecasts?” *Bulletin of the American Meteorological Society*, **83**(3), pp. 407–430.
- [12] BERRY, D. and B. FRISTEDT (1985) *Bandit Problems: Sequential Allocation of Experiments (Monographs on Statistics and Applied Probability)*, Springer-Science+Business Media.
- [13] DOH, N. L., C. KIM, and W. K. CHUNG (2007) “A practical path planner for the robotic vacuum cleaner in rectilinear environments,” *IEEE Transactions on Consumer Electronics*, **53**(2), pp. 519–527.
- [14] CHEUNG, J., A. HALLY, J. HEIJSTEK, A. MARSMAN, and J.-L. BRENGUIER (2015) “Recommendations on trajectory selection in flight planning based on weather uncertainty,” in *5th SESAR Innovation Days*.
- [15] GONZÁLEZ, D., J. PÉREZ, V. MILANÉS, and F. NASHASHIBI (2016) “A Review of Motion Planning Techniques for Automated Vehicles,” *IEEE Transactions on Intelligent Transportation Systems*, **17**(4), pp. 1135–1145.
- [16] GOERZEN, C., Z. KONG, and B. METTLER (2010) “A Survey of Motion Planning Algorithms from the Perspective of Autonomous UAV Guidance,” *Journal of Intelligent and Robotic Systems*, **57**(65), pp. 65–100.
- [17] ZERMELO, E. (1931) “Navigationsproblem bei ruhender oder veränderlicher Windverteilung.” *Differentiation*, pp. 114–124.
- [18] JARDIN, M. R. and A. E. BRYSON (2001) “Neighboring Optimal Aircraft Guidance in Winds,” *Journal of Guidance, Control, and Dynamics*, **24**(4), pp. 710–715.
- [19] OTTE, M., W. SILVA, and E. FREW (2016) “Any-Time Path-Planning : Time-Varying Wind Field + Moving Obstacles,” in *International Conference on Robotics and Automation*.
- [20] CHAKRABARTY, A. and J. W. LANGELAAN (2013) “UAV flight path planning in time varying complex wind-fields,” in *American Control Conference*, pp. 2568–2574.
- [21] DAI, R. (2013) “Path Planning of Solar-Powered Unmanned Aerial Vehicles at Low Altitude,” *Midwest Symposium on Circuits and Systems*, pp. 693–696.

- [22] WIRTH, L., P. OETTERSHAGEN, and R. SIEGWART (2015) “Meteorological Path Planning Using Dynamic Programming for a Solar-Powered UAV,” in *2015 IEEE Aerospace Conference*, Big Sky, MT.
- [23] AL-SABBAN, W. H., L. F. GONZALEZ, and R. N. SMITH (2013) “Wind-energy based path planning for Unmanned Aerial Vehicles using Markov Decision Processes,” in *International Conference on Robotics and Automation*, IEEE, pp. 784–789.
- [24] STEINER, M., R. BATEMAN, D. MEGENHARDT, Y. LIU, M. XU, M. POCERNICH, and J. KROZEL (2010) “Translation of Ensemble Weather Forecasts into Probabilistic Air Traffic Capacity Impact,” *Air Traffic Control Quarterly*, **18**(3), pp. 229–254.
- [25] XIU, D. and J. S. HESTHAVEN (2005) “High-Order Collocation Methods for Differential Equations with Random Inputs,” *SIAM Journal of Scientific Computing*, **27**(3), pp. 1118–1139.
- [26] GONZALES-ARRIBAS, D., M. SOLER, and SANURJO-RIVO MANUEL (2018) “Robust Aircraft Trajectory Planning Under Wind Uncertainty Using Optimal Control,” *Journal of Guidance, Control, and Dynamics*, **41**(3), pp. 673–688.
- [27] FLANZER, T. C., G. C. BOWER, and I. M. KROO (2012) “Robust Trajectory Optimization for Dynamic Soaring,” *AIAA Guidance, Navigation, and Control Conference*.
- [28] XIU, D. (2009) “Fast Numerical Methods for Stochastic Computations: A Review,” *Communications in Computational Physics*, **5**(2), pp. 242–272.
- [29] KLESH, A. T. and P. T. KABAMBA (2007) “Energy-Optimal Path Planning for Solar-Powered Aircraft in Level Flight,” in *AIAA Guidance, Navigation and Control Conference and Exhibit*.
- [30] DAI, R., U. LEE, S. HOSSEINI, and M. MESBAHI (2012) “Optimal path planning for solar-powered UAVs based on unit quaternions,” in *IEEE Conference on Decision and Control*, pp. 3104–3109.
- [31] HOSSEINI, S. and M. MESBAHI (2016) “Energy-Aware Aerial Surveillance for a Long-Endurance Solar-Powered Unmanned Aerial Vehicles,” *Journal of Guidance, Control, and Dynamics*, **39**(9), pp. 1980–1993.
- [32] EDWARDS, D. J., A. D. KAHN, M. KELLY, S. HEINZEN, D. A. SCHEIMAN, P. P. JENKINS, R. WALTERS, and R. HOHEISEL (2016) “Maximizing Net Power in Circular Turns for Solar and Autonomous Soaring Aircraft,” *Journal of Aircraft*, **53**(5), pp. 1237–1247.

- [33] MARTIN, R. A., N. S. GATES, A. NING, and J. D. HEDENGREN (2018) “Dynamic Optimization of High-Altitude Solar Aircraft Trajectories Under Station-Keeping Constraints,” *Journal of Guidance, Control, and Dynamics*, pp. 1–15.
- [34] RAGOT, F. (2004) “Best Speed Story 1938-1950,” *Technical Soaring*, **28**(1).
- [35] REICHMANN, H. (1981) *Cross-Country Soaring*, Soaring Society of America.
- [36] BARNABY, R. S. (1930) *Gliders and Gliding*, Ronald Press Company.
- [37] ARHO, R. (1973) “Optimal Dolphin Soaring as a Variation Problem,” *Technical Soaring*, **3**(1), pp. 20–26.
- [38] DE JONG, J. L. (1978) “Optimal Range Velocity Polar,” *Technical Soaring*, **6**(4), pp. 25–45.
- [39] LAWRENCE, N. R. J. and S. SUKKARIEH (2011) “Autonomous Exploration of a Wind Field with a Gliding Aircraft,” *Journal of Guidance, Control, and Dynamics*, **34**(3), pp. 719–733.
- [40] DEPENBUSCH, N. T., J. J. BIRD, and J. W. LANGELAAN (2016) “The AutoSOAR autonomous soaring aircraft, part 1: Autonomy algorithms,” *Journal of Field Robotics*, **35**(6), pp. 868–889.
- [41] BIRD, J. J., J. W. LANGELAAN, and J. SPLETZER (2014) “Closing the Loop in Dynamic Soaring,” *AIAA Guidance, Navigation, and Control Conference*, (January), pp. 1–19.
- [42] GLASHEEN, K., J. PINTO, M. STEINER, and E. W. FREW (2019) “Experimental Assessment of Local Weather Forecasts for Small Unmanned Aircraft Flight,” in *AIAA Scitech Forum*.
- [43] JONASSEN, M. O., H. ÓLAFSSON, H. ÁGÚSTSSON, Ó. RÖGNVALDSSON, and J. REUDER (2012) “Improving High Resolution Numerical Weather Simulations by Assimilating Data from an Unmanned Aerial System,” *Monthly Weather Review*, **140**, pp. 3734–3756.
- [44] FLAGG, D. D., J. D. DOYLE, T. R. HOLT, D. P. TYNDALL, C. M. AMERAULT, D. GEISZLER, T. HAACK, J. R. MOSKAITIS, J. NACHAMKIN, and D. P. ELEUTERIO (2017) “On the Impact of Unmanned Aerial System Observations on Numerical Weather Prediction in the Coastal Zone,” *Monthly Weather Review*, **146**(2), pp. 599–622.

- [45] OETTERSHAGEN, P., F. ACHERMANN, M. BENJAMIN, D. SCHNEIDER, and R. SIEGWART (2017) “Towards Fully Environment-Aware UAVs: Real-Time Path Planning with Online 3D Wind Field Prediction in Complex Terrain,” *arXiv Preprint*, arXiv:1712.03608v1.
- [46] FREW, E. W., B. ARGROW, A. HOUSTON, C. WEISS, and J. ELSTON (2017) “An Energy-Aware Airborne Dynamic Data-Driven Application System for Persistent Sampling and Surveillance,” *Procedia Computer Science*, **18**, pp. 2008–2017.
- [47] LENSCHOW, D. H. and B. B. STANKOV (1986) “Length Scales in the Convective Boundary Layer,” *Journal of the Atmospheric Sciences*, **43**(12), pp. 1198–1209.
- [48] KRAUSE, A., A. SINGH, and C. GUESTRIN (2008) “Near-Optimal Sensor Placements in Gaussian Processes: Theory, Efficient Algorithms and Empirical Studies,” *Journal of Machine Learning Research*, **9**, pp. 235–284.
- [49] DEVRIES, L., S. J. MAJUMDAR, and D. A. PALEY (2012) “Observability-based Optimization of Coordinated Sampling Trajectories for Recursive Estimation of a Strong, Spatially Varying Flowfield,” *Journal of Intelligent and Robotic Systems*, **70**(1-4), pp. 527–544.
- [50] KULESHOV, V. and D. PRECUP (2000) “Algorithms for the multi-armed bandit problem,” *Journal of Machine Learning Research*, **1**(48), arXiv:1402.6028v1.
- [51] VERMOREL, J. and M. MOHRI (2005) “Empirical Evaluation of Multi-Armed Bandit Algorithms,” in *European conference on machine learning*, pp. 437–448.
- [52] LAI, T. L. and H. ROBBINS (1985) “Asymptotically efficient adaptive allocation rules,” *Advances in Applied Mathematics*, **6**(1), pp. 4–22.
- [53] AUER, P., R. ORTNER, and C. SZEPESVÁRI (2007) “Improved rates for the stochastic continuum-armed bandit problem,” *Learning Theory*, **4539**, pp. 454–468.
- [54] KLEINBERG, R. (2004) “Nearly tight bounds for the continuum-armed bandit problem,” in *7th International Conference on Neural Information Processing Systems*, pp. 697–704.
- [55] BERG, S. (2010) *Solving dynamic bandit problems and decentralized games using the Kalman Bayesian learning automaton*, Ph.D. thesis, University of Agder.

- [56] GARIVIER, A. and E. MOULINES (2008) “On Upper-Confidence Bound Policies for Non-Stationary Bandit Problems,” *arXiv Preprint*, arXiv:0805.3415.
- [57] GRANMO, O. C. and S. BERG (2010) “Solving non-stationary bandit problems by random sampling from sibling Kalman filters,” in *International Conference on Industrial, Engineering and Other Applications of Applied Intelligent Systems*, pp. 199–208.
- [58] RAJ, V. and S. KALYANI (2017) “Taming Non-stationary Bandits: A Bayesian Approach,” *arXiv Preprint*, arXiv:1707.09727.
- [59] WALLACE, J. M. and P. V. HOBBS (2006) *Atmospheric science: an introductory survey*, Academic press.
- [60] UNIVERSITY CENTER FOR ATMOSPHERIC RESEARCH (2012), “Cloud Types | UCAR Center for Science Education,” .
- [61] GODSKE, C. L., T. BERGERON, J. BJERNKNES, and R. C. BUNDGAARD (1957) *Dynamic Meteorology and Weather Forecasting*, American Meteorological Society and Carnegie Institution.
- [62] ALLEN, M. and V. LIN (2007) “Guidance and Control of an Autonomous Soaring Vehicle with Flight Test Results,” in *45th AIAA Aerospace Sciences Meeting and Exhibit*.
- [63] ANDERSSON, K., I. KAMINER, and K. D. JONES (2010) “Autonomous Soaring; Flight Test Results of a Thermal Centering Controller,” *AIAA Guidance, Navigation, and Control Conference*.
- [64] EDWARDS, D. J. and L. M. SILVERBERG (2010) “Autonomous Soaring: The Montague Cross-Country Challenge,” *Journal of Aircraft*, **47**(5), pp. 1763–1769.
- [65] HAZEN, Z. R. T. (2012) *Design and Implementation of a Low Cost Thermal Soaring System for Uninhabited Aircraft*, Master’s thesis, Wichita State University.
- [66] DEPENBUSCH, N. T., J. J. BIRD, and J. W. LANGELAAN (2017) “The AutoSOAR autonomous soaring aircraft part 2: Hardware implementation and flight results,” *Journal of Field Robotics*, (May), pp. 1–24.
- [67] GUILLIARD, I., R. ROGAHN, J. PIAVIS, and A. KOLOBOV (2018) “Autonomous Thermalling as a Partially Observable Markov Decision Process (Extended Version),” in *Robotics: Science and Systems 2018*, arXiv:1805.09875.

- [68] SACHS, G., J. LENZ, and F. HOLZAPFEL (2009) “Unlimited endurance performance of solar UAVs with minimal or zero electric energy storage,” in *AIAA Guidance, Navigation, and Control Conference*, Chicago, IL.
- [69] SAARLAS, M. (2007) *Aircraft Performance*, John Wiley & Sons, Inc., Hoboken, NJ.
- [70] BIRD, J. J. and J. W. LANGELAAN (2017) “Design Space Exploration for Hybrid Solar / Soaring Aircraft,” in *17th AIAA Aviation Technology, Integration, and Operations Conference*.
- [71] METZGER, D. E. and J. K. HEDRICK (1975) “Optimal flight paths for soaring flight,” *Journal of Aircraft*, **12**(11), pp. 867–871.
- [72] STEVENS, B. L. and F. L. LEWIS (2003) *Aircraft Control and Simulation*, 2nd ed., Wiley, Hoboken, New Jersey.
- [73] SCHEIMAN, D., R. HOHEISEL, D. J. EDWARDS, A. PAULSEN, J. LORENTZEN, P. JENKINS, S. CARUTHERS, S. CARTER, and R. WALTERS (2016) “A Path Toward Enhanced Endurance of a UAV Using IMM Solar Cells,” in *2016 IEEE 43rd Photovoltaic Specialists Conference (PVSC)*, pp. 1095–1100.
- [74] F. HOLMGREN, W., C. W. HANSEN, and M. A. MIKOFSKI (2018) “Pvlib Python: a Python Package for Modeling Solar Energy Systems,” *Journal of Open Source Software*, **3**(29), p. 884.
- [75] ALLEN, M. J. (2006) “Updraft Model for Development of Autonomous Soaring Uninhabited Air Vehicles,” in *44th AIAA Aerospace Sciences Meeting and Exhibit*, Reno, NV.
- [76] EDWARDS, D. J. (2008) “Implementation Details and Flight Test Results of an Autonomous Soaring Controller,” in *AIAA Guidance, Navigation, and Control Conference*, American Institute of Aeronautics and Astronautics.
- [77] SMITH, T. L., S. G. BENJAMIN, J. M. BROWN, S. WEYGANDT, T. SMIRNOVA, and B. SCHWARTZ (2008) “Convection forecasts from the hourly updated, 3-km High Resolution Rapid Refresh (HRRR) model,” in *24th Conference on Severe Local Storms*.
- [78] MEIER, L., D. HONEGGER, and M. POLLEFEYS (2015) “PX4: A node-based multithreaded open source robotics framework for deeply embedded platforms,” *IEEE International Conference on Robotics and Automation*, pp. 6235–6240.

- [79] QUIGLEY, M., B. GERKEY, K. CONLEY, J. FAUST, T. FOOTE, J. LEIBS, E. BERGER, R. WHEELER, and A. NG (2009) “ROS: an open-source Robot Operating System,” in *Open-Source Software workshop of the International Conference on Robotics and Automation (ICRA)*.
- [80] CHRISTOPHER, R. (2012) *Extending the endurance of small unmanned aerial vehicles using advanced flexible solar cells*, Master’s thesis, Naval Postgraduate School.
- [81] SILENT FALCON (2019), “Silent Falcon,” .
URL <http://www.silentfalconuas.com/silent-falcon>
- [82] ARAÚJO, G. L. and A. MARTÍ (1994) “Absolute limiting efficiencies for photovoltaic energy conversion,” *Solar Energy Materials and Solar Cells*, **33**(2), pp. 213–240.
- [83] SOMERS, D. M. and M. D. MAUGHMER (1992) “The SM701 Airfoil an Airfoil for World Class Sailplanes,” *Technical Soaring*, **16**(3).
- [84] XIONGFENG, Z., G. ZHENG, F. RONGFEI, H. ZHONGXI, and G. XIANZHONG (2014) “How High Can Solar-Powered Airplanes Fly,” *Journal of Aircraft*, **51**(5), pp. 1653–1659.
- [85] GUO, Z., X.-K. CHEN, Z.-X. HOU, and J. GUO (2011) “Development of a Solar Electric Powered UAV for Long Endurance Flight,” in *11th AIAA Aviation Technology, Integration, and Operations (ATIO) Conference*.
- [86] LEE, B., P. PARK, K. KIM, and S. KWON (2014) “The flight test and power simulations of an UAV powered by solar cells, a fuel cell and batteries,” *Journal of Mechanical Science and Technology*, **28**(1), pp. 399–405.
- [87] BENJAMIN, S. G., B. E. SCHWARTZ, E. J. SZOKE, and S. E. KOCH (2004) “The value of wind profiler data in U.S. weather forecasting,” *Bulletin of the American Meteorological Society*, **85**(12), pp. 1871–1886.
- [88] PICHUGINA, Y. L., R. M. BANTA, J. B. OLSON, J. R. CARLEY, M. C. MARQUIS, W. A. BREWER, J. M. WILCZAK, I. DJALALOVA, L. BIANCO, E. P. JAMES, S. G. BENJAMIN, and J. CLINE (2017) “Assessment of NWP Forecast Models in Simulating Offshore Winds through the Lower Boundary Layer by Measurements from a Ship-Based Scanning Doppler Lidar,” *Monthly Weather Review*, **145**(10), pp. 4277–4301.
- [89] KLESH, A. T. and P. T. KABAMBA (2009) “Solar-Powered Aircraft: Energy-Optimal Path Planning and Perpetual Endurance,” *Journal of Guidance, Control, and Dynamics*, **32**(4), pp. 1320–1329.

- [90] CHEN, C.-T. (2013) *Linear System Theory and Design*, fourth ed., Oxford University Press, New York, NY.
- [91] JONES, E., T. OLIPHANT, P. PETERSON, and OTHERS (2019), “SciPy: Open Source Scientific Tools for Python,” .
URL <https://www.scipy.org>
- [92] RASMUSSEN, C. E. and C. K. I. WILLIAMS (2006) “Regression,” in *Gaussian Processes for Machine Learning*, MIT Press.
- [93] LAWRENCE, N. R. J. and S. SUKKARIEH (2011) “Path planning for autonomous soaring flight in dynamic wind fields,” *IEEE International Conference on Robotics and Automation*, pp. 2499–2505.
- [94] SHEAHAN, S., E. FREW, and A. B. MILLS (2017) “Kernel Function Evaluation For Gaussian Process Wind Regression,” in *AIAA Scitech Forum*.
- [95] DIERCX, P. (1993) *Curve and Surface Fitting with Splines*, Oxford University Press.
- [96] SIMON, D. (2006) *Optimal State Estimation: Kalman, H Infinity, and Nonlinear Approaches*, Wiley.
- [97] BIRD, J. J. (2013) *Wind Estimation and Closed-Loop Control of a Soaring Vehicle*, Master’s thesis, The Pennsylvania State University.
- [98] NICHOLS, T., B. ARGROW, and D. KINGSTON (2017) “Error Sensitivity Analysis of Small UAS Wind-Sensing Systems,” in *AIAA Scitech Forum*.
- [99] LANGELAAN, J. W., N. ALLEY, and J. NEIDHOEFER (2011) “Wind Field Estimation for Small Unmanned Aerial Vehicles,” *Journal of Guidance, Control, and Dynamics*, **34**(4), pp. 1016–1030.
- [100] NUCCIARONE, J. J. and G. S. YOUNG (1991), “Aircraft Measurements of Turbulence Spectra in the Marine Stratocumulus-topped Boundary Layer,” .
- [101] BUSCH, N. E. and H. A. PANOFSKY (1968) “Recent spectra of atmospheric turbulence,” *Quarterly Journal of the Royal Meteorological Society*, **94**(400), pp. 132–148.
- [102] MOENG, C.-H. (1986) “Large-Eddy Simulation of a Stratus-Topped Boundary Layer. Part I: Structure and Budgets,” *Journal of the Atmospheric Sciences*, **43**(23), pp. 2886–2900.
- [103] MACCREADY, P. B. (1962) “The inertial subrange of atmospheric turbulence,” *Journal of Geophysical Research*, **67**(3), pp. 1051–1059.

- [104] PAPOULIS, A. and S. U. PILLAI (2002) *Probability, Random Variables, and Stochastic Processes*, fourth ed., McGraw-Hill.
- [105] JULIER, S. J. (2003) “The scaled unscented transformation,” in *Proceedings of the American Control Conference*, pp. 4555–4559.
- [106] SODDELL, J. R., K. MCGUFFIE, and G. J. HOLLAND (2004) “Intercomparison of atmospheric soundings from the aerosonde and radiosonde,” *Journal of Applied Meteorology*, **43**, pp. 1260–1269.
- [107] KOCH, S. E., M. FENGLER, P. B. CHILSON, K. L. ELMORE, B. ARGROW, D. L. ANDRA, and T. LINDLEY (2018) “On the use of unmanned aircraft for sampling mesoscale phenomena in the preconvective boundary layer,” *Journal of Atmospheric and Oceanic Technology*, **35**(11), pp. 2265–2288.
- [108] VAN DER HOVEN, I. (1957) “Power Spectrum of Horizontal Wind Speed in the Frequency Range from 0.0007 to 900 Cycles per Hour,” *Journal of Meteorology*, **14**.
- [109] SINGH, A., A. KRAUSE, and W. J. KAISER (2009) “Nonmyopic adaptive informative path planning for multiple robots,” *IJCAI International Joint Conference on Artificial Intelligence*, pp. 1843–1850.
- [110] FIEDLER, F. and H. A. PANOFSKY (1970) “Atmospheric Scales and Spectral Gaps,” *Bulletin of the American Meteorological Society*, **51**(12), pp. 1114–1120.
- [111] CESSNA AIRCRAFT COMPANY (1998) *Skyhawk SP Information Manual*, *Tech. rep.*
- [112] WILCZAK, J. (2014) *WFIP NOAA Final Report*, *Tech. rep.*, National Oceanic and Atmospheric Administration.
- [113] PEREZ, R., A. KANKIEWICZ, J. SCHLEMMER, K. HEMKER, and S. KIVALOV (2014) “A new operational solar resource forecast model service for PV fleet simulation,” *2014 IEEE 40th Photovoltaic Specialist Conference, PVSC 2014*, pp. 69–74.
- [114] ZAVERI, M. (2019), “Wing, Owned by Google’s Parent Company, Gets First Approval for Drone Deliveries in U.S.” .
URL <https://www.nytimes.com/2019/04/23/technology/drone-deliveries-google-wing.html>

Vita

John Bird

Education

Ph.D. Aerospace Engineering, Pennsylvania State University, 2019
Atmospherically Aware Aircraft Guidance Using in situ Observations
Advisor: Jack W Langelaan

M.S. Aerospace Engineering, Pennsylvania State University, 2013
Wind Estimation and Closed-Loop Control of a Soaring Vehicle
Advisor: Jack W Langelaan

B.S. Aerospace Engineering, Wichita State University, 2011

Publications

Bird, J. J., Richardson, S. J., & Langelaan, J. W. (2019). Estimating the Vertical Structure of Weather-Induced Mission Costs for Small UAS. *Sensors*, 19(12), 2770.

Bird, J. J., & Langelaan, J. W. (2019). Optimal Speed Scheduling for Hybrid Solar Aircraft with Arrival Time Condition. In AIAA Scitech 2019 Forum.

Deppenbusch, N. T., Bird, J. J., & Langelaan, J. W. (2018). The AutoSOAR autonomous soaring aircraft, part 1: Autonomy algorithms. *Journal of Field Robotics*, 35(6), 868-889.

Deppenbusch, N. T., Bird, J. J., & Langelaan, J. W. (2018). The AutoSOAR autonomous soaring aircraft part 2: Hardware implementation and flight results. *Journal of Field Robotics*, 35(4), 435-458.

Stroman, R. O., Edwards, D. J., Jenkins, P., Carter, S., Newton, D., Kelly, M., Heinzen, S., Young, T., Dobrokhodov, V., Langelaan, J., Bird, J. & Reinecke, P. A. (2018). The Hybrid Tiger: A Long Endurance Solar/Fuel Cell/Soaring Unmanned Aerial Vehicle. In Power Sources Conference

Bird, J. J., & Langelaan, J. (2017). Design Space Exploration for Hybrid Solar/Soaring Aircraft. In 17th AIAA Aviation Technology, Integration, and Operations Conference.